Contents

Chapter 1

Introduction

The modern day technological advancement is almost entirely dependent on the semiconductor devices. The application of semiconductors in the device fabrication commonly requires that defects be introduced in the semiconductor lattice, intentionally by radiating with energetic particles or unintentionally during processing stages. Defects can be introduced in the lattice during semiconductor processing techniques such as semiconductor growth, ion implantation, plasma etching, annealing, metallization, (sputter and electron beam deposition) or by particle irradiation. These defects modify the properties of the substrate and therefore influence the performance of devices fabricated thereon. Defects may have detrimental effects on the performance of devices such as solar cells, wherein they act as efficient recombination centers and degrade minority carrier lifetimes [1]. However, there are other instances when defects are created intentionally to produce impurity - related defect levels in the semiconductor band gap, i.e. to absorb low energy photons known as impurity photovoltaic effect and as efficient recombination centers in fast-switching silicon power devices [2]. A true understanding of a defect in a semiconductor usually requires achieving four steps (a) defect observation and characterization, (b) defect identification, (c) defect control, and (d) influence of defects on device performance. The knowledge of how defects influence the device performance is the basis for development of improved semiconductor devices. For this basic motivation, defect characterization is still a very much active field for all technological important semiconductors until all aspects of defects are well understood. Although a lot of work has been done on defects introduced in silicon (Si) materials in the last two decades, most of the defects have not been identified. Silicon integrated circuits presently dominate the semiconductor industry and recently it has been used to develop, high efficiency and low cost solar cells as the search for

alternative energy sources continues. To achieve high efficiency (i.e. faster switching speeds, low power consumption, etc) devices, great emphasis is now placed on decreasing the lateral and vertical dimensions of the individual transistors (miniaturization). With the reduction in size the devices become sensitive to minute defect concentration therefore it is essential to identify and control defects in the substrate, thereby reducing or eliminating those that are detrimental to the device and retaining those that are beneficial to the device operation.

It is interesting to note that the first transistor invented in 1947 by J. Bardeen and W.H Brattain used elemental germanium (Ge) as the semi-conducting material, but since then silicon soon replaced germanium as substrate material because of its inherent advantages, such as thermal stability, abundance and availability of a stable oxide, (SiO_2). Recently there has been a sudden growing interest in Ge as a possible candidate for high performance complimentary metal-oxide-semiconductor (CMOS) devices and faster switching transistors because of the higher electron and hole mobilities of Ge at low electric fields when compared to Si [3].

Conventional Deep Level Transient Spectroscopy (DLTS) [4] is a powerful junction capacitance tool that is used to study defects introduced in semiconductors. DLTS is particularly attractive because it can be used to characterize defects using various kinds of space-charge-based devices, ranging from simple Schottky barrier diodes (SBDs) and p-n junctions, MOS structures (which are all standard building blocks of solid state circuitry) to device structures with higher degrees of complexities [5]. The recent development of high-resolution Laplace – DLTS [6,7] has significantly increased its spectroscopic ability, by giving over an order of magnitude improved energy resolution in studies of thermal emission of carriers from deep states, thereby facilitating the separation of the closely spaced energy levels that show up as a single broad feature in conventional DLTS. The L-DLTS has a remarkable sensitivity (it can probe very low concentrations of defects $>10^{10}$ cm^{-3}), can be used to probe very narrow regions of semiconductors (e.g. regions of shallow implants) and even be used to study selectively the active regions of devices (Differential DLTS [8,9]).

Deep levels in crystalline Si and Ge have been systematically characterized by DLTS and LDLTS after exposing the materials to energetic particles (MeV electrons or keV

Ar ions) and metal deposition (resistive deposition, electron beam deposition or sputter deposition). Particle irradiation and metal deposition are crucial and necessary stages during device processing steps, such as ion implantation for doping, metallization for low resistive for low resistive ohmic contacts as well as rectifying contacts, and plasma etching. Therefore it is of paramount importance to study the properties of these defects and their effects on device application.

An overview of the semiconductor theory with the emphasis on Si and Ge is given in chapter 2 since these materials are the substrates used in this study. Defects, their creation and annealing mechanisms, resulting from bombardment with energetic particles in semiconductors, are described in chapter 3. The underlying theory behind DLTS and Laplace-DLTS is presented in chapter 4 followed by the experimental techniques in chapter 5. The results of defects created during processing steps or by irradiation of silicon and germanium are presented in chapters 6, 7, 8, 9 and 10, while chapter 11 gives a summary of the work covered in this thesis.

References

[1] J. Schmidt and K. Bonde, *Phys. Rev.* B **69** (2004) 024107.

[2] D.C. Sawko and J. Bartko, *IEEE Nucl. Sci.* **30** (1983) 1756.

[3] R. Hull, J.C. Bean (Eds.), Germanium Silicon, Physics Materials, Semiconductor and Semi-metals, vol. 56, Academic, San Diego, 1999.

[4] D.V. Lang, *J. Appl. Phys*. **45** (1974) 3023.

[5] F.D. Auret and P.N.K. Deenapanray, *Crit. Rev. Sol. Stat Mater. Sci*. **29** (2004) 1.

[6] L. Dobaczewski, P. Kaczor, I.D. Hawkins and A.R. Peaker. *J. Appl. Phys*. **76** (1994) 194.

[7] L. Dobaczewski, A.R. Peaker and K.B. Nielsen, *J. Appl. Phys*. **96** (1994) 4689.

[8] H. Lefèvre and M. Schulz, *Appl Phys. A* **12** (1977) 45.

[9] Y. Zohta and M.O. Watanabe, *J. Appl. Phys*. **53** (1982) 1809.

Chapter 2

Semiconductor Theory

2.1 Introduction

In this chapter semiconductor theory is discussed. Section 2.2 presents the crystal structure and the energy band theory, particularly for silicon and germanium. The importance of energy band theories for a crystalline solid is due to the fact that many important physical and optical properties of a solid can be readily explained using its energy band structure. In principle, the energy band structure of a solid can be constructed by solving the Schrödinger equation for electrons in a crystalline solid that contains a large number of interacting electrons and atoms. Section 2.3 discusses the metal-semiconductor junctions. A metal–semiconductor contact will either form a Schottky or an ohmic contact. These contacts are very important since they make it possible to electrically probe the semiconductor underlying layer by various characterization tools, such as current-voltage, capacitance-voltage and deep level transient spectroscopy (DLTS) measurements, which have been employed in this work. Section 2.4 presents the current transport mechanism through the metal-semiconductor junctions.

2.2 The Crystal and Band Structure of Si and Ge

Elemental semiconductors such as silicon and germanium crystallize into the diamond structure. The diamond structure shown in Fig. 2-1 is actually formed by two interpenetrating face-centered cubic (fcc) lattices with the vertex atom of one fcc sublattice located at (0, 0, 0) and the vertex atom of another fcc sublattice located at (a/4, a/4, a/4), where a is the lattice constant. In the diamond lattice structure, the

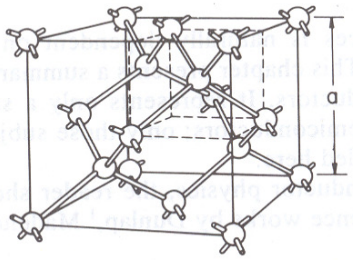

Fig. 2-1. Diamond structure redrawn from ref. 1.

primitive basis of two identical atoms located at (0, 0, 0) and (*a*/4, *a*/4, *a*/4) is associated with each lattice point of the fcc lattice. The band structure of a crystalline solid, that is, the energy-momentum (*E*-*k*) relationship is usually obtained by solving the Schrödinger equation of an approximate one-electron problem. The Bloch theorem, states that if a potential energy $V(\vec{r})$ is periodic with the periodicity of the lattice, then the solutions $\phi_k(\vec{r})$ of the Schrödinger equation [1-2]

$$\left[-\frac{\hbar^2}{2m}\nabla^2 + V(\vec{r})\right]\phi_k(\vec{r}) = E_k\phi_k(\vec{r}) \tag{2.1}$$

are of the form

$$\phi_k(\vec{r}) = e^{j\vec{k}.\vec{r}}U_n(\vec{k}.\vec{r}) \text{ (Bloch function)} \tag{2.2}$$

where, $U_n(\vec{k},\vec{r})$ is periodic in $\vec{r}$ with periodicity of the lattice and *n* is the band index. From the Bloch theorem one can show that the energy $E_{\vec{k}}$ is periodic in the reciprocal lattice. For a given band index, to label the energy uniquely, it is sufficient to use only *k*'s in a primitive cell of the reciprocal lattice.

The energy bands of solids have been studied theoretically using a variety of numerical methods. For semiconductors the three methods most frequently used are the orthogonalized plane-wave method [3-4], the pseudopotential method [5], and the **k.p** method [6]. Fig. 2-2 depicts the energy-band structures for Ge and Si [1,7]. For any semiconductor there is a forbidden energy region in which allowed states cannot exist, which is called the energy gap E_g. The energy gap is the most important

parameter in semiconductor physics. Electron states are permitted above and below this energy gap. The bands above the energy gap are called the conduction bands and below the energy gap, the valence bands. The two top valence bands (Fig. 2-2) can be approximately fitted by two parabolic bands with different curvature: the heavy-hole band (the wider band with a smaller $\partial^2 E/\partial k^2$) and light-hole band (the narrower band with larger $\partial^2 E/\partial k^2$). The lowest conduction minimum is along the $\langle 111 \rangle$ axes in Ge and along $\langle 100 \rangle$ axes in Si. The band structure of Si shows six equivalent conduction minima and three valence band maxima all at the center of Brillouin zone. The valence band tops are degenerate and the third one is split-off by 44 meV.

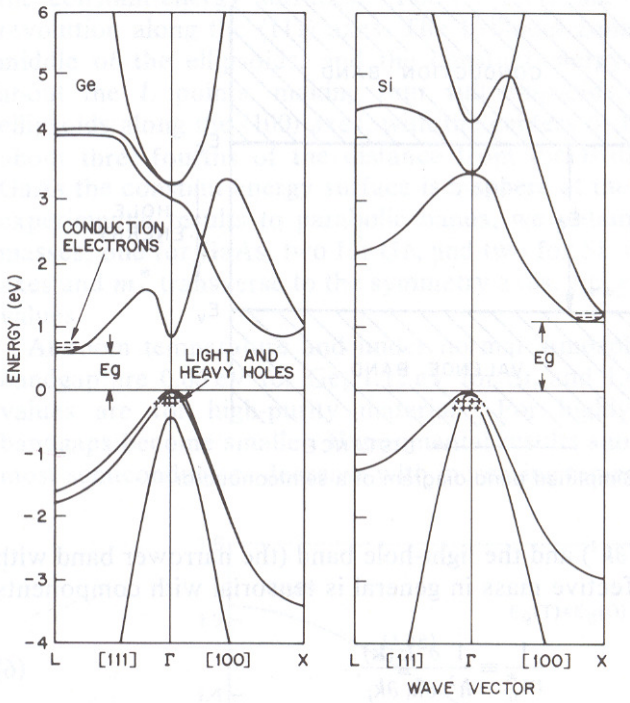

Fig. 2-2. Energy band structure of Ge and Si, where E_g is the energy band gap. Plus signs indicate the holes in the valence band and minus signs indicate electrons in the conduction band (after ref. 1).

At room temperature (300 K) and under normal atmosphere, the values of the band gap are 0.66 eV for Ge, and 1.12 eV for Si [1]. These values are for high-purity materials. For highly doped materials the band gaps become smaller. Experimental results show that the band gaps of Ge and Si decrease with increasing temperature and the relationship can be expressed approximately by a universal function given by equation (2.3),

$$E_g(T) = E_g(0) - \frac{\alpha T^2}{(T+\beta)} \tag{2.3}$$

where, $E_g(0)$ is the energy gap at T = 0 K , α and β are material constants given in Table 2.1.

Table 2.1. Coefficients for the temperature dependent energy band gap of Si and Ge.

Material	$E_g(0)$ (eV)	α (x 10^{-4} eV/K)	β (K)
Si	1.519	4.730	636
Ge	1.170	4.774	235

The temperature coefficient dE_g / dT is negative for Ge and Si [1]. Near room temperature, the band gap of Ge increases with pressure and that of Si decreases with pressure [8] as shown in equation (2.4),

$$\frac{dE_g}{dP} = \begin{cases} 5.0\times10^{-6} \text{ eV/(kg/cm}^2\text{)} & \text{for Ge} \\ -2.4\times10^{-6} \text{ eV/(kg/cm}^2\text{)} & \text{for Si} \end{cases} \tag{2.4}$$

The mobility of electrons and holes is an important semiconductor property, which depends on the band structure. For bulk-grown Si and Ge the hole and electron mobilities at room temperature are listed in Table 2.2.

Table. 2.2. Mobilities (at room temperature) in bulk Si and Ge

Material	μ_e (cm^2/Vs)	μ_h (cm^2/Vs)
Si	1500	450
Ge	3900	1900

The values show higher mobilities in Ge when compared to Si, by nearly a factor of 2 for electron mobility and a factor of 4 for hole mobility. Experiment [9] has shown that the band structure can be affected by the application of stress, breaking the

degeneracy of both the conduction and the valence band. This has an effect of increasing the electron and hole mobility in a given semiconductor.

2.3 Metal – Semiconductor Junctions

Metal-semiconductor contacts are an integral part of the semiconductor industry. It is well known that one of the most important aspects of realizing the potential of a semiconductor device is the preparation of high quality metal contacts to the material. There are two types of metal-semiconductor contacts, ohmic and Schottky (rectifying) contacts. The Schottky contacts can be used for a wide variety of device applications e.g. microwave receiver detectors, mixers [10] and used as gate electrodes of field-effect transistors (MESFETS), the drain and source in MOSFETS [1]. In addition to these several device applications, Schottky contacts may also be used to study bulk defects (introduced during material growth, during device processing or by energetic particles such electrons or protons) and interface properties of a metal-semiconductor system. In this study the Schottky contacts have been used to form the space charge region, which is used to probe the semiconductor forbidden gap and measure the electrical properties of the defect levels on and beneath the metal-semiconductor interface.

2.3.1 Schottky Barrier Junctions

In principle, for a Schottky barrier junction, there is nonlinear current flow through the device, allowing current to flow in one direction but not the other (rectifying effect). According to the Schottky-Mott model, [11-12] the barrier height of an ideal Schottky contact between a metal and an *n*-type semiconductor in the absence of surface states is equal to the difference between the metal work function ϕ_m and the electron affinity χ of the semiconductor, which can be written as

$$\phi_{Bn} = \phi_m - \chi \tag{2.5}$$

The work function of a metal ϕ_m is defined as the minimum amount of energy required to remove an electron completely from the metal into free space (the so called vacuum level). The work function of a metal is a fundamental property of the

particular metal (measured in eV). Similarly the work function of a semiconductor ϕ_{sc} is the difference in energy between the Fermi level and the vacuum level. The electron affinity χ is the difference between the vacuum level and bottom of the conduction band and is independent of the doping concentration of the semiconductor material. The work function of the semiconductor material ϕ_{sc} and the electron affinity χ are related by the following equation,

$$\phi_{sc} = \chi + \xi \tag{2.6}$$

where, ξ is the energy difference between the Fermi level and conduction band in the neutral region of the semiconductor and is given by

$$\xi = kT\ln(N_C / N_D) \tag{2.7}$$

where, k is the Boltzmann constant, T is the temperature, N_C is the effective density of states in the conduction band and N_D is the free carrier concentration. The schematic energy band diagrams in Fig. 2-3 show the process of barrier formation according to the Schottky-Mott theory. We assume a uniformly doped *n*-type semiconductor and that $\phi_m > \phi_{sc}$, Fig. 2-3a shows the case when the materials are isolated from each other. The average energy of electrons in the semiconductor is greater than the average energy of those in the metal. When the metal is brought into intimate (perfect) contact with the semiconductor (with no surface states), the difference in the average electron energy will transfer electrons from semiconductor to the metal. The electron transfer will take place until the Fermi levels coincide, and thermal equilibrium is established, Fig. 2-3b. Relative to the Fermi level in the metal, the Fermi level in the semiconductor is lowered by an amount equal to the difference between the two work functions, causing band bending. This difference between the work functions is called the built-in-voltage (V_{bi}) given by, $V_{bi} = (\phi_m - \phi_{sc})$. Simultaneously an electric field is created due to the negative charge on the surface of the metal that is balanced by an equal but positive charge in the semiconductor. Due to the relatively low dopant concentration, this positive charge is distributed

throughout a barrier region near the semiconductor surface, up to a thickness W_o in the semiconductor, which is the depletion width.

An electron at the Femi level in the metal will see a potential barrier towards the semiconductor of ϕ_{Bn} which is the difference between ϕ_m and χ. Whereas an electron deep in the semiconductor at $E = E_C$ sees a potential barrier towards the metal of $V_{bi} = (\phi_m - \phi_{sc})$.

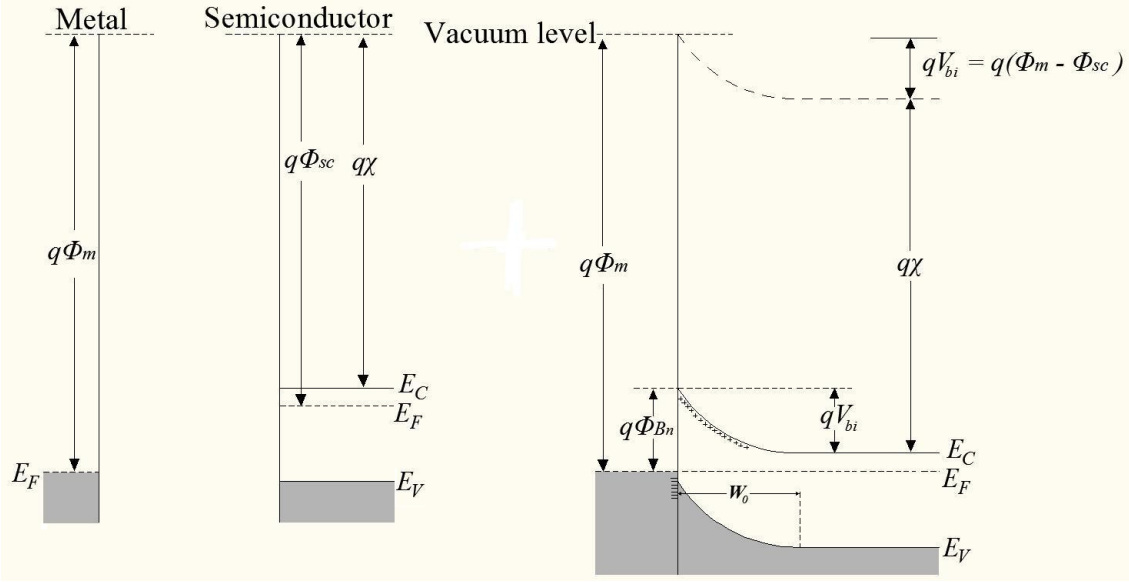

Fig. 2-3. Energy band diagrams of a metal/n-type semiconductor with $\phi_m > \phi_{sc}$ (a) materials isolated from each other and (b) at thermal equilibrium after contact is made, redrawn from ref. 13.

When a bias voltage is applied across the junction, non-equilibrium conditions are established. Under zero bias conditions, electrons at the Fermi level from both the metal and semiconductor see the same barrier height. Therefore there is no net flow of electrons over the barrier in either direction. Applying a negative potential V_a on the semiconductor side, causes the band bending to decrease. This reduces the barrier for electrons crossing from the semiconductor toward the metal from qV_{bi} to $q(V_{bi} - V_a)$, i.e. forward biasing condition. The electrons can now cross from the semiconductor to the metal more easily since they now see a reduced barrier. When a positive potential V_a is applied to the semiconductor, the barrier for electron from the metal increases by

qV_a. This also increases the depletion width. The number of electrons with enough energy to cross the barrier from the semiconductor to the metal is reduced due the increased barrier, i.e. reverse biasing condition. The barrier seen by electrons from the metal stays the same as the number of electrons crossing from the semiconductor to metal decreases.

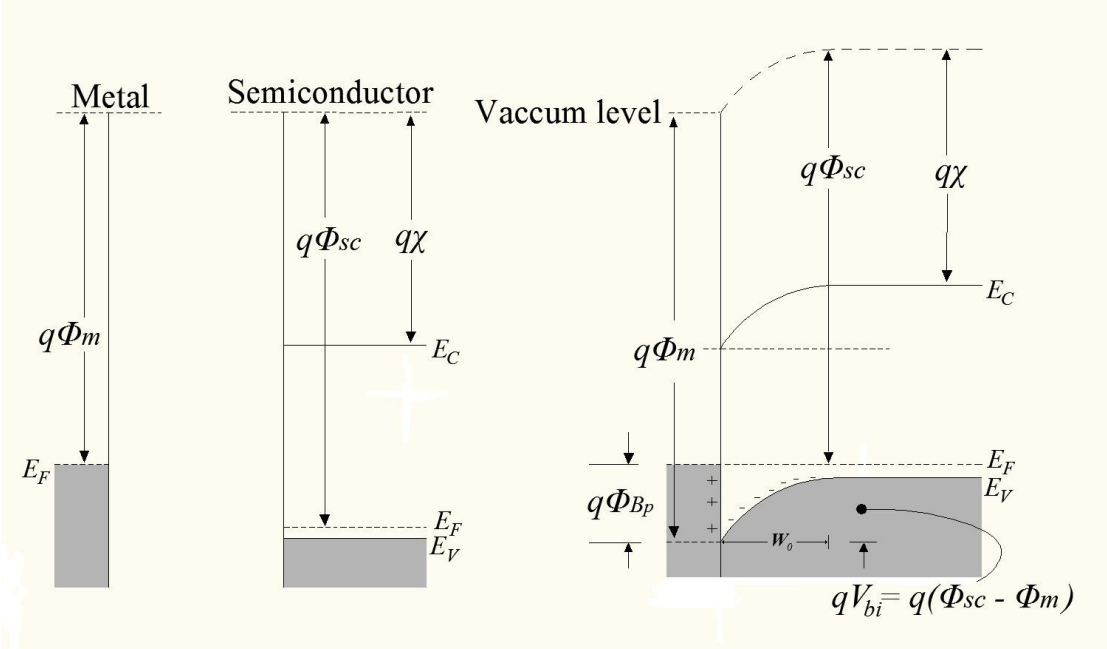

Fig. 2-4. Energy band diagrams of a metal/p-type semiconductor with $\phi_m < \phi_{sc}$ (a) materials isolated from each other and (b) at thermal equilibrium after contact is made, redrawn from ref. 13.

A barrier can also be formed between a metal and *p*-type semiconductor. Consider a *p*-type semiconductor having $\phi_m < \phi_{sc}$ with the two materials isolated from each other, Fig. 2-4(a). When the two substrates are brought into intimate contact, electrons will flow from the metal into the semiconductor until, E_F, is the same throughout, Fig. 2-4(b). Each electron flowing into the semiconductor removes a hole from the valence band, leaving behind an unneutralized charge of ionized acceptors in the semiconductor, forming a depletion region in the semiconductor. Since the current in *p*-type semiconductors is carried mainly by holes, the contact shown in Fig. 2-4(b) is therefore rectifying and in the absence of surface states the barrier height ϕ_{Bp} can be expressed by

$$\phi_{Bp} = \frac{E_g}{q} - (\phi_m - \chi) \tag{2.8}$$

where, E_g is the energy band gap and q is the electron charge. From equation (2.8) it follows that, according to the Schottky-Mott theory, for a given semiconductor and for any metal, the sum of the barrier heights on *n*-type and *p*-type substrates is equal to the band gap, or

$$q(\phi_{Bn} + \phi_{Bp}) = E_g \tag{2.9}$$

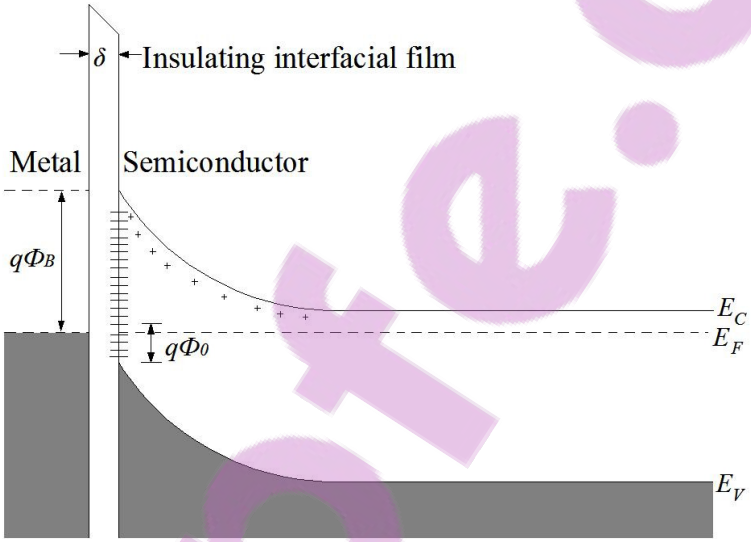

Fig. 2-5. Energy band diagram of a metal-semiconductor contact with surface states and an interfacial oxide layer of thickness δ.

It should be noted that in reality the measured barrier heights for most of the metal-semiconductor contacts do not always follow the simple predictions given by the equations (2.5) and (2.8) because in their derivation we did not consider the thin insulating layer of oxide on the semiconductor surface, interface states and the image force lowering effect. In fact, for most compound semiconductors, because of high surface state density and Fermi-level pinning at the interface states, the barrier height formed is found to be independent of the metals used [1], and this is also true for covalently bonded semiconductors like Ge and Si [13]. In a covalently bonded crystal, the surface atoms have no neighbors on the vacuum side, with which they can form covalent bond. Thus, each surface atom has one broken covalent bond known as the

dangling bond. Dangling bonds give rise to surface states that are continuously distributed in energy within the forbidden gap. These states pin the Fermi level at the surface and thus influence the barrier height. Prior to metal deposition, the semiconductor surface is chemically cleaned. This process invariably leaves a thin (5 to 20 Å thick) [13] insulating oxide layer on the semiconductor surface. In the presence of interface states and a thin interfacial layer (Fig.2-5) the barrier height is given by [14],

$$\phi_B = \gamma(\phi_m - \chi) + (1-\gamma)(E_g - \phi_o) \tag{2.10}$$

where,

$$\gamma = \frac{\varepsilon_i}{\varepsilon_i + q\delta D_s} \tag{2.11}$$

δ being the thickness of the interfacial layer, E_g the band gap, ϕ_o the so-called neutral level, ε_i the permittivity of this film and D_s the density of interface states per eV per unit area in the band gap. The surface states are characterized by the neutral level ϕ_o such that all the states below ϕ_o are filled, while those above are empty. Equilibrium is reached when electrons from the semiconductor adjacent to the surface occupy states above ϕ_o. Thus, the surface becomes negatively charged and a depletion region is created within the semiconductor near the surface. If a metal is now brought into contact with the semiconductor, exchange of the electrons takes place between the metal and the semiconductor surface states, while the depletion charge remains practically unchanged. Thus ϕ_B tends to the Schottky-Mott limit $(\phi_B = \phi_m - \chi)$ as $D_s \rightarrow 0$ and to the Bardeen limit $(\phi_B = E_g - \phi_o)$ as $D_s \rightarrow \infty$. Thus, if the density of surface states becomes high enough, the Fermi level is said to be pinned at $E_F \approx \phi_o$ so that,

$$\phi_B \approx E_g - \phi_o \tag{2.12}$$

which is the Bardeen limit.

2.3.2 Depletion Layer

It has been discussed in the previous section that when a metal is brought into intimate contact with a semiconductor, the conduction and valence bands of the semiconductor are brought into a definite energy relationship with the Fermi level in the metal. Once this relationship is known, it serves as the boundary condition on the solution of the Poison equation in the semiconductor. The boundary conditions are obtained from,

(i) barrier height and

(ii) taking electric field in the bulk of the semiconductor as zero.

At the interface, taking $x = 0$, the boundary condition can now be written as $V(0) = V_{bi}$ and $E(\infty) = 0$, where V is the contact potential, V_{bi} is built-in potential and E is the electric field. The Poisson's equation in the semiconductor can be written in one dimension as

$$\frac{d^2V}{dx^2} = -\frac{1}{\varepsilon_s}\rho(x) \tag{2.13}$$

where, $\rho(x)$ is the total charge density in the semiconductor at a depth x and ε_s is the permittivity of the semiconductor. Generally, $\rho(x)$ should include contributions form the valence band, conduction band, ionized donors and acceptors, and deep levels in the band gap. This will lead to a complicated equation which requires numerical methods to solve. To simplify the equation, the abrupt approximation is used. Considering the abrupt approximation, it is assumed that the semiconductor can be divided into two regions: (i) the depletion region, directly below the metal, which contains no free carriers, and (ii) the bulk semiconductor, which is electrically neutral, and in which no electric field exists. In the depletion region, $\rho(x) \approx qN_D$, and in the semiconductor bulk, $\rho(x) \approx 0$ and $dV/dx \approx 0$. If the width of the depletion region is W, the charge density in the semiconductor can be written as

$$\rho(x) = \begin{cases} qN_D & \text{if } x \le W \\ 0 & \text{if } x > W \end{cases} \tag{2.14}$$

where, N_D is the density of dopants and q the electronic charge. Integrating equation 2.13 twice and applying the boundary condition, the depletion width can be written as

$$W = \sqrt{\frac{2\varepsilon_s V_{bi}}{qN_D}} \tag{2.15}$$

When the contact is biased by an externally applied voltage V_a, the depletion width can be written as

$$W = \sqrt{\frac{2\varepsilon_s}{qN_D}\left(V_{bi} - V_a - \frac{kT}{q}\right)} \tag{2.16}$$

where, the term kT/q arises from the contribution of the majority carrier distribution tail. It is seen from equation (2.16) that the depletion layer width is directly proportional to the square root of the applied voltage, and inversely proportional to the square root of the dopant density of the semiconductor. The electric field in the semiconductor is given by

$$E(x) = -\frac{qN_D}{\varepsilon_e}(W - x) = \frac{qN_D}{\varepsilon_s}x - E_m \tag{2.17}$$

where, E_m is the maximum field strength which occurs at $x = 0$. Integrating the electric field yields the electrostatic potential,

$$V(x) = \frac{qN_D}{\varepsilon_e}(Wx - \frac{1}{2}x^2) - \phi_{Bn} \tag{2.18}$$

The space charge Q_{sc} per unit area of the semiconductor and the depletion-layer capacitance C per unit area are given by

$$Q_{sc} = qN_D W = \sqrt{2q\varepsilon_e N_D\left(V_{bi} - V_a - \frac{kT}{q}\right)} \tag{2.19}$$

$$C = \frac{\left|\partial Q_{sc}\right|}{\partial V_a} = \sqrt{\frac{q\varepsilon_s N_D}{2(V_{bi} - V_a - kT/q)}} = \frac{\varepsilon_s}{W} \tag{2.20}$$

equation (2.20) can be written in the form,

$$\frac{1}{C^2} = \frac{2(V_{bi} - V_a - kT/q)}{q\varepsilon_s N_D} \tag{2.21}$$

or

$$N_D = \frac{2}{q\varepsilon_s}\left[-\frac{1}{d(1/C^2)/dV}\right] \tag{2.22}$$

If N_D is constant throughout the depletion region, a plot of $1/C^2$ versus V should yield a straight line graph. If N_D is not a constant then the differential capacitance method can be used to determine the doping profile from equation (2.22). Using the voltage axis intercept, the barrier height can be determined from the equation,

$$\varphi_{Bn} = V_i + \xi + \frac{kT}{q} - \Delta\phi \tag{2.23}$$

where V_i, is the voltage axis intercept (equivalent to V_{bi}), $\Delta\phi$ is the image force barrier lowering, and ξ, the depth of the Fermi level below the conduction band, which can be computed if the doping level is known.

2.3.3 Ohmic Contacts

An ohmic contact is defined as a metal-semiconductor contact that has a negligible contact resistance R_c, relative to the bulk or spreading resistance of the semiconductor, given by $R_C = \left(\frac{\partial J}{\partial V}\right)^{-1}_{V=0}$, when evaluated at zero bias. A good ohmic contact would have very small voltage drop even at large current levels, and that the voltage drop would be the same for both forward and reverse current flow.

The following two major approaches can be used to achieve ohmic contacts to semiconductors:

(a) If one can find metal-semiconductor combinations in which the barrier height is determined by the difference in their work functions, it should be possible to create an ohmic contact by choosing the metal with $\phi_m < \phi_{sc}$ in the case of *n*-type semiconductor, (Fig. 2-6a and b) and $\phi_m > \phi_{sc}$ in *p*-type semiconductor, a typical ideal ohmic contact. A low-resistance symmetrical contact to a semiconductor is obtained if the barrier is small compared with *kT*. When this is the case, carriers can flow over the barrier in either direction with little resistance as shown in Fig.2-6c. It can be shown that, [1]

$$R_C = \frac{k}{qA^*T}\exp\left(\frac{q\phi_{Bn}}{kT}\right) \qquad (2.24)$$

Equation (2.24) shows, that low barrier height should be used to obtain small R_c. Since for most semiconductors, because of the presence of interface states, ohmic contacts cannot be obtained by proper choice of metal work function and a metal does not generally exist with low-enough work function to yield a low barrier.

(b) An alternate and more practical contact is a tunnel contact shown in Fig. 2-6d. Such contacts have a high enough doping in the semiconductor so that there is only a thin barrier separating the metal from the semiconductor interface, and carriers can readily tunnel across such barrier. The required doping density for such contact is 10^{19} cm^{-3} or higher [1].

The fabrication of ohmic contacts frequently includes a high temperature annealing step so that the deposited metals can either alloy with the semiconductor or the high-temperature anneal, reduces the unintentional barrier at the interface. In case of Ge, Au-Sb alloy with (0.1% Sb) is first evaporated onto back of the Ge. These contacts are then annealed at 350˚C under inert conditions such as nitrogen or argon [12] to reduce contact resistance by increasing the tunneling current as shown in Fig 2-6 (d). The use of a reducing atmosphere reduces any further oxidation of the metal during

annealing, while it can also reduce any interfacial oxide between the metal and semiconductor.

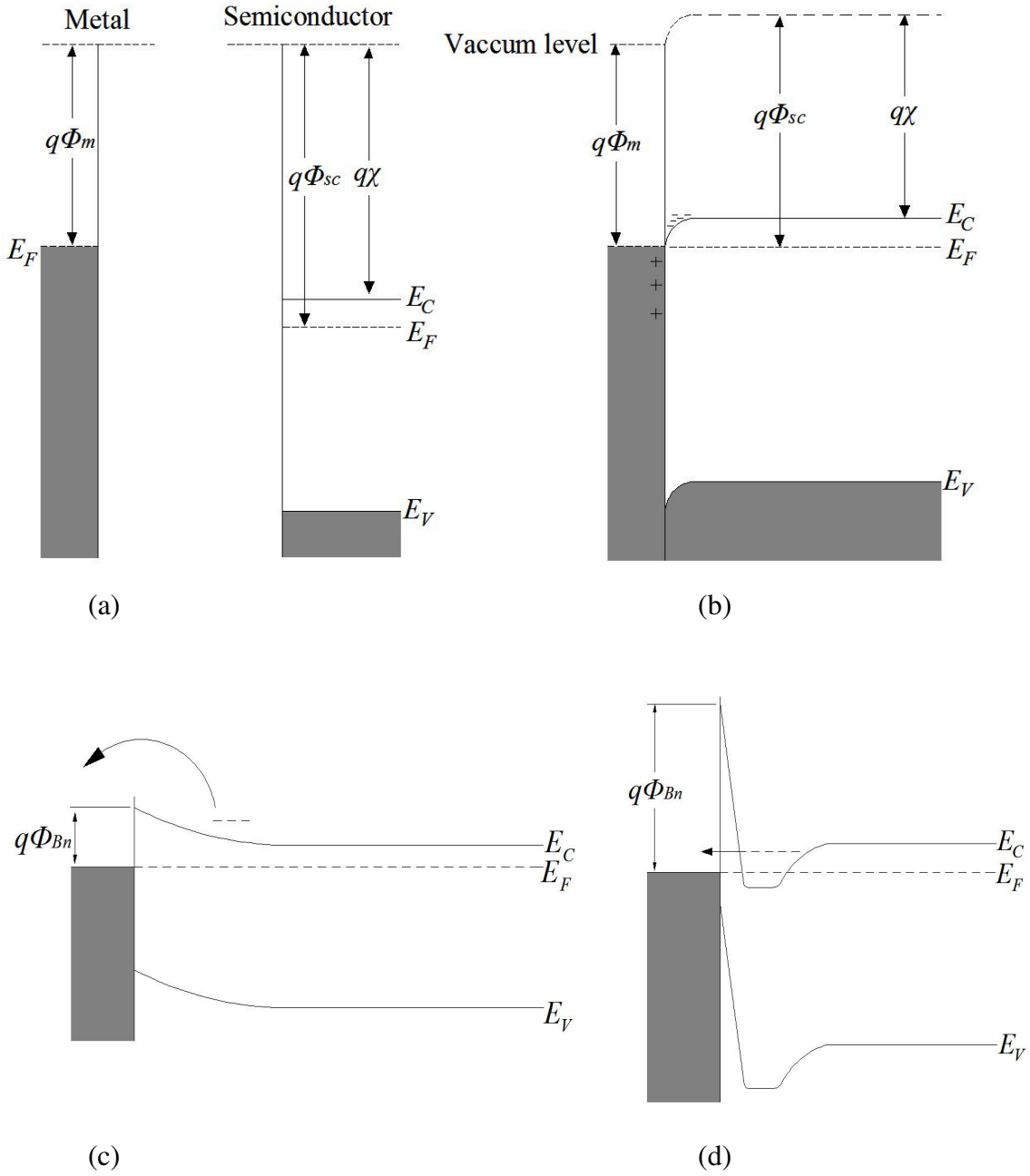

Fig. 2-6. Energy band diagrams of a metal/n-type semiconductor with $\phi_m < \phi_{sc}$. (a) Materials isolated from each other and (b) at thermal equilibrium after contact is made (ideal ohmic contact formation) redrawn from ref. 16. Ohmic contact formation by, (c) low barrier height and (d) high doping contacts, redrawn from ref. 1.

2.4 Current Transport Mechanisms in Metal – Semiconductor Junctions

The electrical properties of Schottky contacts are determined by the transport mechanisms across the barrier. The current transport in metal-semiconductor contacts is mainly due to majority carriers. The various ways in which electrons can be transported across a metal – semiconductor junction under a forward bias are:

(a) emission of electrons from the semiconductor over the top of the barrier into the metal [the dominant process for Schottky diodes with moderately doped semiconductor (e.g., $N_D \leq 10^{17}$ for Si) operated at moderate temperatures (e.g., 300 K)],

(b) quantum-mechanical tunneling through the barrier (important for heavily doped semiconductors and responsible for most ohmic contacts),

(c) recombination in the charged space region, and

(d) hole injection from the metal to semiconductor (equivalent to recombination in the neutral region).

In addition, we may have edge leakage current due to a high electric field at the contact periphery or interface current due to traps at the metal-semiconductor interface. The inverse processes occur under reverse bias. It is possible to make practical diodes in which (a) is the most important and such diodes are generally referred to as 'nearly ideal'. Process (b), (c) and (d) cause departures from ideality. There are two basic processes that govern the emission of electrons from the semiconductor over the top of the barrier into the metal, (i) electrons are transported from the bulk of the semiconductor and across the depletion region of the semiconductor by the mechanism of drift and diffusion in the electric field of the barrier, and (ii) at the interface, their emission into the metal is determined by the rate of transfer of electrons across the boundary between the metal and semiconductor. These two processes are effectively in series and according to the diffusion theory by Schottky [10] the first process is more important, whereas according to the thermionic–emission theory of Berthe [14] the assumption is that the current-limiting process is the actual transfer of electrons across the interface between the semiconductor and the metal. In case of the moderately doped Si and Ge Schottky diodes used in this study, the dominant mechanism for reverse bias and small forward bias is thermionic-emission. Assuming that the velocity distribution of the electrons in

the conduction band is Maxwellian and ideal rectifier characteristics, the current density, J flowing across the barrier can be written as,

$$J = A^{*}T^{2}\exp(-q\phi_{B}/kT)[\exp(qV/kT)-1] \tag{2.25}$$

where, A^{*} is the effective Richardson constant, ϕ_{B} is the barrier height and, T the temperature of the junction, provided the barrier height is independent of bias. The current density for a non-ideal diode can be written as,

$$J = J_{0}[\exp(qV/nkT)-1], \quad \text{where } J_{o} = A^{*}T^{2}\exp(-q\phi_{B}/kT) \tag{2.26}$$

with series resistance R_s and $V > 3kT/q$ equation (2.26) is now given by,

$$J \approx J_{0}\exp\left(\frac{q(V-IR_{s})}{nkT}\right) \tag{2.27}$$

where, J_o, is the saturation current density obtained by extrapolating the current density from the log-linear region to $V = 0$ and, n, is the ideality factor defined as

$$n = \frac{q}{kT}\left[\frac{\partial V}{\partial(\ln J)}\right] \tag{2.28}$$

The ideality factor has been introduced in equations (2.26) and (2.27) to account for deviation of the diodes from ideal behaviour. For an ideal Schottky diode, the barrier height is independent on the bias and current flows only due to thermionic emission. The saturation current density, J_o, can be expressed as,

$$J_{0} = A^{*}T^{2}\exp\left[-q\left(\frac{\phi_{Bo}-\Delta\phi_{ifl}}{kT}\right)\right] \tag{2.28}$$

where, ϕ_{Bo} is the zero bias barrier height, and $\Delta\phi_{ifl}$ is the barrier lowering by the image force. The effective zero bias barrier height is given by, $\phi_{e} = \phi_{Bo} - \Delta\phi_{ifl}$. From

the graph of $ln(J)$ versus V, it is possible to determine n, J_o and R_s. A least squares curve fitting procedure is applied to the linear region (forward bias region) of this graph. The ideality factor is proportional to the inverse of the gradient of this fit. The value of J_o, is obtained by the extrapolation of the linear fit to $V = 0$ V. An expression for the effective barrier height (at $V = 0$ V), is given by,

$$\phi_{eo}^{I-V} = \frac{kT}{q} \ln\left(\frac{A^* T^2}{J_o}\right) \tag{2.29}$$

A theoretical value for the effective Richardson constant, A^*, can be determined by using the following equation,

$$A^* = \frac{4\pi q m^* k^2}{h^3} \tag{2.30}$$

where m^* is the electron effective mass.

References

[1] S.M. Sze, *Physics of Semiconductor devices,* Wiley & Sons, Canada, 1981.

[2] C. Kettel, *Quantum Theory of Solids*, Wiley, New York, 1963.

[3] L.C. Allen, *Phys. Rev*. **98** (1955) 993.

[4] F. Herman, Proc. *IRE*, **43** (1955) 1703.

[5] J.C. Phillips, *Phys. Rev*. **112** (1958) 685.

[6] R.A. Smith, *Semiconductors,* 2nd ed., Cambridge University Press, London, 1979.

[7] C. Kittel, *Introduction to solid state Physics,* Wiley, New York, 1976.

[8] W. Paul and D.M. Warschauer, Eds., *Solids under pressure*, McGraw-Hill, New York, 1963.

[9] E.E. Haller, *Mater. Sci. in Semiconductor processing* **9** (2006) 408.

[10] S. Li, *Semiconductor Physical Electronics,* Springer, 2006.

[11] N.F. Mott, *Proc. Camb. Phil. Soc*. **34** (1938) 568.

[12] M P. Lepselter and J.M. Andrews, *Ohmic Contacts to Semiconductors,* The Electrochemical Society Symposium Series, New York 1969, p159.

[13] M.S. Tyagi, *Introduction to Semiconductor Materials and Devices,* John Wile and Sons, USA, 1991.

[14] H.A. Bethe, *MIT Radiat. Lab. Rep.* **43** (1942) 12.

[15] E.H. Rhoderick, *Metal-Semiconductor Contacts,* Clarendon, Oxford, 1978

[16] B.G. Streetman, S. Banerjee, *Solid State Electronic Devices,* Prentice Hall, 5thed. USA, 2000.

Chapter 3

Defects in Semiconductors

3.1 Introduction

In an ideal crystal lattice, each atom is at its designated position and deviations from this perfect structure are called imperfections or defects. These defects may introduce electronic energy states into the semiconductor band gap, which can be placed into two categories: shallow levels and deep levels. Shallow levels are located near their related band edges (valence band for acceptors and conduction band for donors) i.e. ~0.1 eV from the band edge, thus these levels are thermally ionized at room temperature. The ionization energy of a shallow level can be approximately described by a modified hydrogenic model [1]. For example, a shallow donor resembles a hydrogen atom with a positive nucleus binding an electron. Impurity elements which are used as dopants in semiconductors normally create these shallow levels which are ionized at room temperature and provide free carriers to form p-type or n-type semiconductor. Deep levels are those defects positioned deeper in the band gap than the dopant levels and are found to bind the carriers much more strongly into highly compact, localized states. The deep levels have higher ionization energies, therefore contribute very little to the free charge carriers. Defects with deep levels in the band gap are often referred to as, ‘traps’, ‘recombination centers’, or ‘generation centers’. Deep levels are important in semiconductors since they modify the properties of the semiconductors and therefore, those of the devices fabricated thereon. Deep levels are desirable in some applications, e.g. in fast switching devices, where they can be exploited as recombination centers which quickly remove minority carriers, enhancing the device’s switching speed thereby increasing efficiency [2,3]. Deep levels may also be a nuisance if present in semiconductors that are used for photovoltaic applications since they reduce the cells’ efficiency by allowing created electron-hole to recombine. Thus deep level study is of paramount importance in the

semiconductor device industry so that those deep levels which are useful can be deliberately added and those that are deleterious can be reduced or eliminated. This chapter will outline the common properties of deep levels (i.e. structure, charge states, formation and migration mechanisms) in silicon and germanium.

3.2 Primary Defects

Defects in semiconductors can be divided into two main categories; point defects and extended defects. Point defects are not extended in space in any dimension and this implies that the perturbation of the lattice is localized about a lattice site and involves only a few nearest neighbours. There are two kinds of point defects of great interest in semiconductor crystals, intrinsic (e.g. vacancies or self-interstitial) and extrinsic point defects (e.g. impurity atoms occupying substitutional or interstitial lattice sites. Small agglomerations of several point defects like divacancies, vacancy-impurity complexes, vacancy-donor etc are also generally considered as point defects. Extended defects are extended in nature (such as, grain boundaries, dislocations or stacking faults). The discussion in this section is focussed more on point defects which are more relevant to the work covered in this thesis.

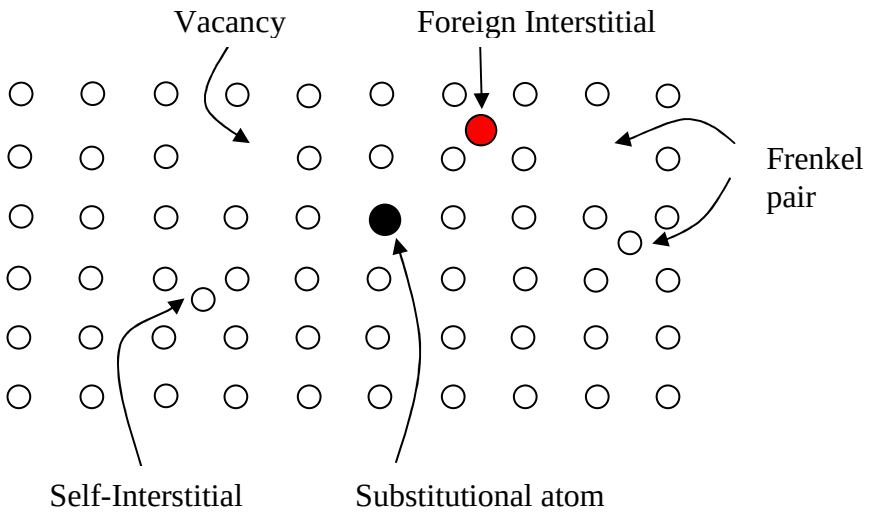

Fig. 3-1. A diagram showing the vacancy, self-interstitial, substitutional defects.

3.2.1 Vacancy Defect

If an atom is removed from its regular lattice site the empty lattice site is called a vacancy defect (V), and is shown in Fig. 3-1. The vacancy in some semiconductors (e.g. in Ge and Si) can have up to five charge states, V^{++}, V^{+}, V^{0}, V^{-} and $V^{=}$. In order

to form a vacancy by removing an atom from its lattice site four bonds are broken in a diamond crystal structure as shown in Fig. 3-2a [4,5]. The broken bonds can form new bonds depending on the charge state (i.e. which is just the number of electrons occupying the dangling bonds) of the vacancy (Fig. 3-2b and c). This causes small inward and outward displacement of neighboring atoms, which either preserves the local symmetry (relaxation) or alters it (distortion). The amplitude of the displacements depends on the charge state of the defect. Another geometric configuration for describing a vacancy is the 'split-vacancy'. The 'split-vacancy' results when an atom resides at the bond center between the empty sites [6], Fig. 3-2d. The 'split-vacancy' is often important primarily to help describe the transition state in vacancy migration [7]. The lattice relaxation depends on the charge state of the point defect (Jahn-Teller effect). Jahn-Teller effect is simply a geometrical distortion which occurs when the electronic state is degenerate, in which case the nuclear state is unstable. Atomic displacements always exist which by lowering the symmetry, split the degenerate level.

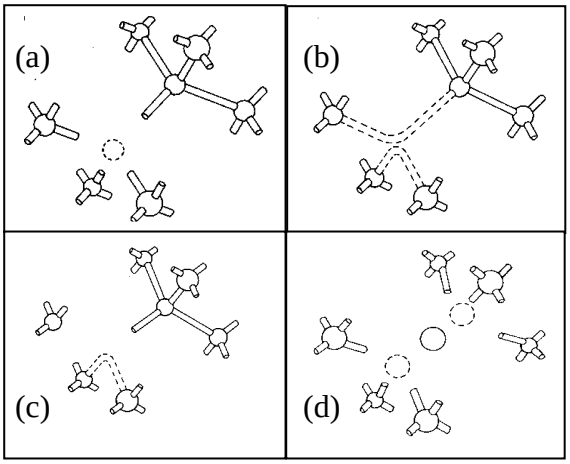

Fig. 3-2. The vacancy configuration in diamond lattice. (a) Four bonds are broken in order to create the vacancy. (b) When there is one electron per dangling bond (i.e., for the neutral vacancy V^0) they form two new bonds leading to local distortion. (c) When an electron is missing (i.e., for the positive vacancy V^+) one of these two bonds is weakened since it contains only one electron. The distortion is thus different from that in the case of V^0. (d) The 'split-vacancy configuration, redrawn from ref. 4.

It should be noted there is general agreement in defect modeling studies that the vacancy formation energy in germanium (1.7 eV – 2.5 eV) is significantly smaller than in silicon (~4.0 eV), for all charge states. When two neighboring atoms are removed and also when two migrating vacancies meet and combine a divacancy is formed. A divacancy can also exist in four different charge states in Si [8].

3.2.2 Interstitial Defect

Interstitials are atoms, which occupy a site in the crystal structure, which is not a regular lattice site as shown in Fig. 3-1. An interstitial defect can be of the same species as the atoms of the lattice (self-interstitial) or of a different nature (an interstitial impurity). Interstitials are generally high-energy configurations. Once again, the introduction of an interstitial induces a relaxation and distortion of the lattice, which surrounds it. The type of configuration the interstitial assumes depends on its ability to make bonds with its neighbors and therefore can change with its charge state. A nearby interstitial defect and vacancy defect is called a Frenkel pair.

3.3 Secondary Defects

The isolated lattice vacancy (V) and self-interstitial (I) are primary defects produced after high-energy particle irradiation in semiconductors. The primary defects are mobile at low temperatures, e.g. in Si the vacancy becomes mobile above 150 K - 200 K and the interstitial is mobile even at 4.2 K [8]. Therefore, deep level transient spectroscopy measurements of room temperature irradiated silicon will not reveal an isolated vacancy or silicon interstitials. The V and I which survive the recombination of simple defects can diffuse into the semiconductor and interact with other intrinsic and extrinsic defects giving rise to complex room temperature stable defects, some of which are depicted in the schematic diagram shown in Fig. 3-3. For example, in silicon when a vacancy becomes mobile, it can be trapped by an oxygen atom to form a V-O complex (A-center), or the doping impurity (e.g. P) to form a V-P complex (*E*-center), or by another vacancy to form divacancies. Other complex defects are via the mobile interstitial (I). It is expected that room temperature defect evolution in silicon shown in Fig. 3-3 should hold similarly for germanium.

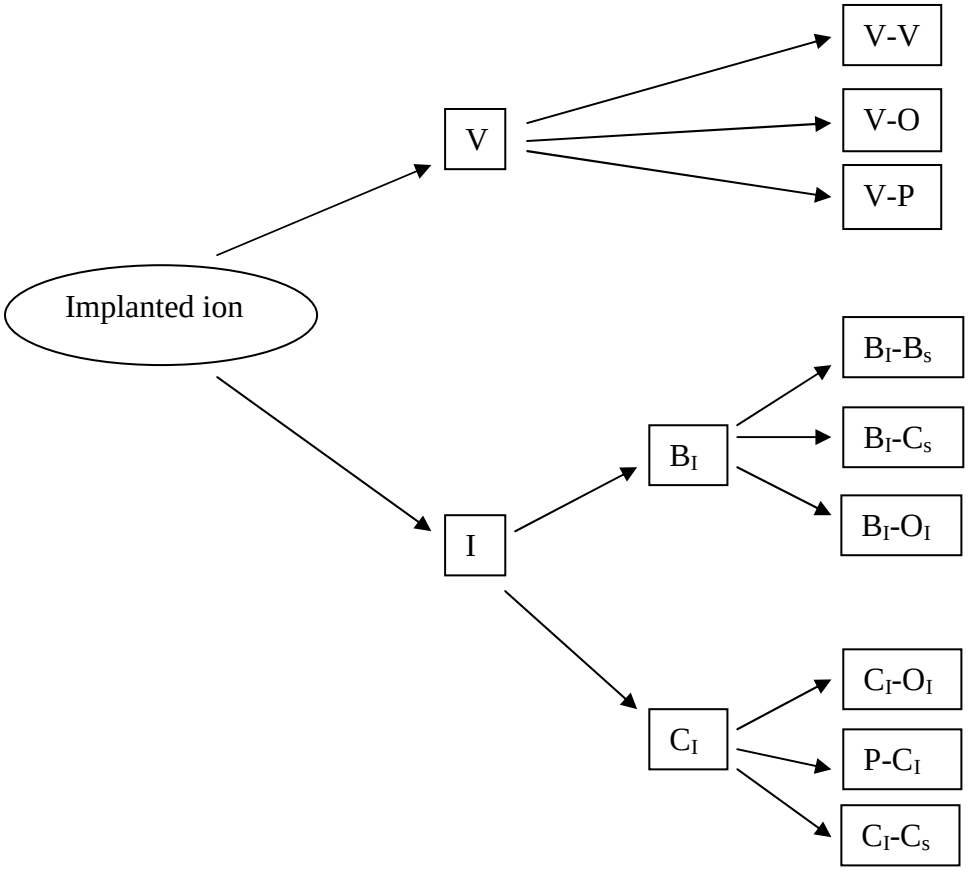

Fig. 3-3. Schematic of room temperature defect evolution in crystalline silicon.

3.3.1 The Divacancy

The divacancy is formed by the removal of two neighbouring atoms. Generally divacancies can be created in semiconductors by particle irradiation either as a primary defect, when collision cascade is dense enough, or as a secondary defect by pairing of single vacancies diffusing randomly. The vacancy in germanium is negatively charged in a broad interval of Fermi level position in the band gap, therefore the formation of divacancies by pairing of single vacancies is suppressed by the coulombic repulsion of the vacancies [9]. The divacancy in Ge has not yet been identified by experimental techniques. Using density functional theory (DFT) cluster calculations, Janke *et al* [10] estimated the energy barrier for migration and dissociation of the divacancy. The dissociation energy consisting of the binding energy between two vacancies and the migration of a single vacancy was found to be between (1.5-1.7) eV whereas the migration barrier of the divacancy was found to be 1.1 eV. This corresponds approximately to a thermal stability of 420 K. The

divacancy in silicon is well known, and can appear in four charge states, V_2^+, V_2^0, V_2^- and $V_2^=$.

3.3.2 The *E*-center

The *E*-center can be described as a vacancy trapped next to a substitutional donor atom. The *E*-center can be formed as a primary defect or when the impurity atom captures a mobile vacancy. As to the formation of an *E*-center, although local atomic strain effect may need to be considered, the key role is played by the coulombic interaction between a positively charged antimony and a negatively charged vacancy [11]. Let's consider the *E*-center in phosphorus-doped silicon, V-P. In the neutral charge state i.e. PV^0, two of the three silicon atoms surrounding the vacancy pull together to form an electron pair, leaving an unpaired electron in the orbital of the third silicon atom, while two electrons with antiparallel spins are accommodated by the phosphorus atom. When the Fermi level is above the *E*-center an extra electron is accepted and becomes negatively charged, PV^-. The formation of *E*-center in silicon removes two electrons in the conduction band by converting a positively charged P donor atom to a negatively charged V-P center. The formation of the *E*-center is regarded as an intermediate step in dopant diffusion in silicon and germanium [12].

3.3.3 The *A*-center

The *A*-center (V-O) may be regarded as a vacancy trapped next to an oxygen atom in an interstitial position. Similar to the *E*-center the *A*-center can be formed as a primary defect or when an oxygen impurity traps a mobile vacancy. The *A*-center competes for the vacancies with the *E*-center and its concentration is dependent on the relative O impurity concentration in the sample. The *A*-center has also been found to be an efficient recombination center [13], and therefore can be used as to control minority carrier lifetime in silicon for fast switching device application.

3.3.4 Other Complex Defects

The mobile Si interstitial (I) diffuses and will replace either carbon (C) or group III impurities e.g. boron (B) (depending on the relative concentration of the two species) through the Watkins replacement [14,15] to form interstitial carbon (C_I) or interstitial B_I respectively. The C_I or B_I are mobile at room temperature and will eventually form

defect complexes with other impurities {e.g. interstitial boron – substitutional boron (B_I-B_s), interstitial boron – interstitial oxygen (B_I-O_I), interstitial boron – substitutional carbon (B_I-C_s), interstitial carbon – interstitial oxygen (C_I-O_I) or interstitial carbon – substitutional carbon (C_I-C_s)} as shown in Fig. 3-3. For a particular defect with a large concentration, it tends to aggregate as the temperature increases from room temperature. In case of a divacancy, when mobile or after dissociating, it can form trivacancies, quadrivacancies, pentavacancies, and higher order defects. This behavior should also be true for self-interstitials and for any type of extrinsic defects.

Most of the primary and secondary defects discussed in the previous sections are electrically active and introduce deep levels in the semiconductor band gap. A deep level may act as a minority carrier trap, majority carrier trap or recombination centre depending on its position in the band gap and on relative capture cross-section of minority and majority carriers. A majority carrier trap is an electron trap in n-type semiconductor or a hole trap in p-type semiconductor. Conversely a minority carrier is a hole trap in n-type semiconductor or an electron in p-type semiconductor. If a majority- or minority- carrier lives a mean lifetime in the captured state and is thermally ejected to the band from which it came, the center may be regarded as majority carrier trap or minority carrier trap respectively. From defect spectroscopy measurements such as deep level transient spectroscopy (DLTS) it is possible to extract the defect properties such as the concentration, energy level, and capture cross-section of defect level. The capture cross-sections, $\sigma_{majority}$ and $\sigma_{minority}$ can now be used to deduce whether the defect will act as minority carrier trap, majority carrier trap or a recombination centre.

Recombination centers are deep levels with approximately equal capture cross-sections for both electrons and holes and these centers are normally located near the middle of the band gap. After capturing a majority carrier, if the majority carrier stays trapped at the center long enough for the trap to capture a minority carrier, then recombination takes place and the center is acting as a recombination center. Most of the defect spectroscopy techniques measure the defect concentration, energy level, and capture cross section for majority and minority carrier traps, e.g. when using DLTS, all the detected defects are in a situation where they behave as majority or

minority carrier traps. Hence it is difficult to say which of the detected defects will be a recombination center. There have been attempts to improve on the technique used to distinguish traps from recombination centers. Markvart *et al* [16] developed an improved version of DLTS, known as recombination DLTS that can be used to identify defects that act as recombination centers. These centers act as "stepping stones" for carriers and contribute to the current-voltage characteristics of rectifying junctions at a recombination rate, U given by [3,17]

$$U = \frac{{}_{p}\,{}_{n}v_{th}(pn - n_i^2)N_T}{{}_{n}[n - n_i \exp\{(E_T - E_i)/kT\}] + {}_{p}[n + n_i \exp\{-(E_T - E_i)\}]} \qquad (3.1)$$

where E_i, E_T, N_T, n_i, n, p, σ_n, and σ_p are the intrinsic Fermi level, defect level, defect concentration, intrinsic carrier density, electron concentration, hole concentration, electron capture cross section and hole capture cross section respectively. From equation (3.1) it is clear that the recombination rate is higher for larger E_T (i.e. most efficient recombination centers are those close to the middle of the band gap and with similar capture cross-sections σ_n and σ_p).

3.4 Theory of Displacement of Atoms in Solids

When passing through matter high-energy particles are decelerated and in the process transfer energy to the material. The transferred energy can modify the structure and properties of the materials. In case of crystalline semiconductors, particle-induced materials modification will occur as long as the projectile particles can transfer energy, E, larger than the displacement energy, E_d, to the lattice atoms [3]. The capacity of a solid to slow a projectile is called the stopping power, and is defined as the amount of energy lost per unit length of trajectory in the solid. The stopping power depends on the type and energy of the projectile and on the mass of the target material.

3.4.1 Energy-Loss Mechanisms

When a particle enters a target material there are two main mechanisms that cause an energy loss: (a) elastic collisions with the nuclei of the target material (nuclear stopping) and (b) inelastic collisions with bound or free electrons (electronic

stopping). In electronic stopping, the term inelastic is used to signify that the collisions may result both in the excitations of bound electrons of the medium and in the excitations of the electron cloud of the ion. The relative effect of the two mechanisms depends on the mass of the target material as well as the energy, mass and charge of the incident particle. Fig. 3.4 is a "universal" diagram showing the nuclear stopping $(d\ /d\ )_n$ and electronic stopping $(d\ /d\ )_e$ in terms of Thomas-Fermi (TF) ion energy, ε and path length, ρ as a function of $\varepsilon^{1/2}$ (which is proportional to the velocity of the implanted ion) [3,18]. The parameters ε and ρ are dimensionless quantities which can be expressed in terms of laboratory energy E and distance x, respectively as;

$$= \frac{4\ \ _0 aM_2}{Z_1 Z_2 e^2 (M_1 + M_2)} E \qquad (3.2)$$

and

$$= N\ \ a^2 \frac{4M_1 M_2}{(M_1 + M_2)} x \qquad (3.3)$$

where M_1 and M_2 are the mass numbers of the incident and target atom respectively, Z_1 and Z_2 are their atomic numbers, e is the electronic charge, N is the concentration of atoms, ε_o is the permittivity of free space and a is the screening radius. The screening radius is normally expressed by [19]

$$a = \frac{0.8853 a_0}{(Z_1^{2/3} + Z_2^{2/3})^{1/2}} \qquad (3.4)$$

where a_0 = 0.529 Å is the Bohr radius. The universal curve shown in Fig. 3-4 enables the approximation of nuclear stopping and associated quantities (e.g. damage production and sputtering) for all particle-target combinations using a single curve. The ion bombardment analysis can be divided into two distinct regimes.

(a) *Nuclear microanalysis regime*: High-energy ions are slowed down mainly by electronic stopping. The contribution from the nuclear stopping tends to be

small at high energies because fast ions have only short time to interact with the target nuclei.

(b) *Ion implantation regime*: When the ion has slowed down sufficiently, the collisions with the nuclei become more and more probable, and the nuclear stopping finally dominate the slowing down process. In this regime nuclear stopping reaches a maximum value (ε_1) around $\varepsilon^{1/2}$ = 0.6 and decreases thereafter as shown in Fig. 3-4 and this corresponds to process associated with low energy ions e.g. ion beam etching and sputtering.

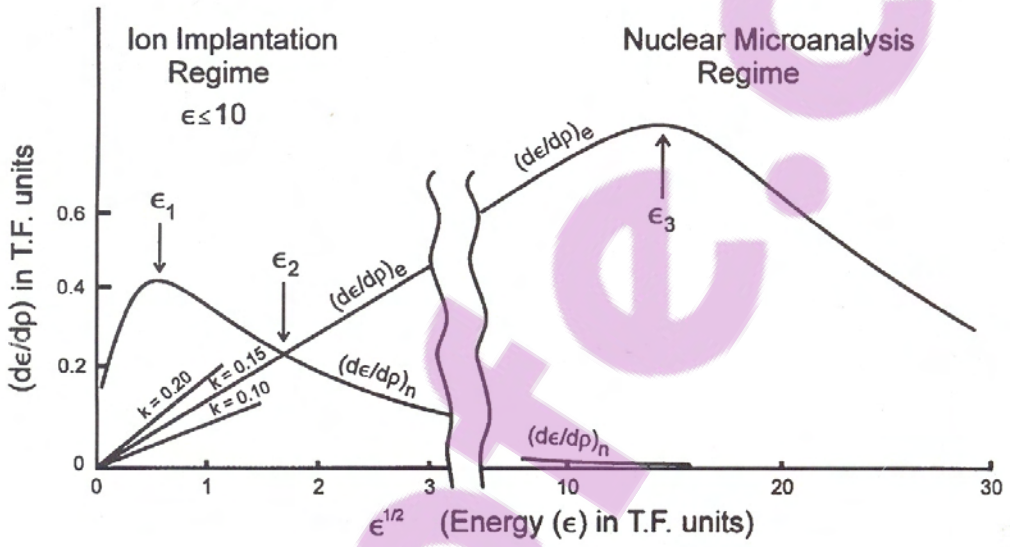

Fig. 3.4. Nuclear and electronic stopping versus the reduced energy of an implanted ion redrawn from ref. 3.

It is important to note that in contrast to the nuclear stopping $(d\ /d\ )_n$ which depends only on ε (i.e. independent of the type of incident particle and target atoms), electronic stopping $(d\ /d\ )_e$ can be expressed by [3]

$$(d\ /d\ )_e = k\ ^{1/2}, \quad \text{for} \quad ^{1/2} < 14 \qquad (3.5)$$

where k is a function of $M_1, M_2,\ Z_1$ and Z_2, thus electron stopping does not exhibit true ε-scaling and therefore may not be described by a universal curve.

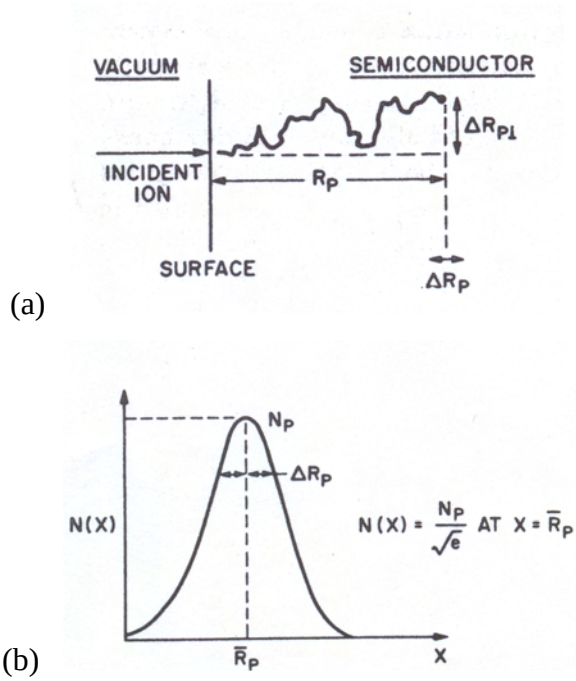

Fig. 3.5. (a) Basic parameters for an implanted ion. R is the total path length, R_p is the projected range, ΔR_p and ΔR_{pL} are the projected standard deviations in the directions parallel and perpendicular to the incident beam, respectively. (b) N(x) is the number of ions per cm^3 at depth x.

The process of ion stopping is a statistical process and so some ions will undergo many collisions, stopping in a distance shorter than the average value. The range R of the projectile is related to its mean track length and for a projectile with initial energy ε_0 the range can be written as

$$R = \int_0^{\varepsilon_0} \frac{1}{(d\varepsilon/dx)_{total}} d\varepsilon \qquad (3.6)$$

where

$$(d\varepsilon/dx)_{total} = (d\varepsilon/dx)_n + (d\varepsilon/dx)_e \qquad (3.7)$$

If $M_1 \geq M_2$ the projected range R_p is obtained by multiplying the range R with the projection factor $\sim(1 + M_2/3M_1)^{-1}$. The average or projected range R_p is defined as the

projection of R on the incident ion beam direction, a projected standard deviation or straggle ΔR_p is the statistical fluctuation along incident ion direction if the spatial distribution of the implanted ions is approximately Gaussian as depicted in Fig. 3-5. The implanted ions may also be scattered along the direction perpendicular to the incident direction and the statistical fluctuation along this direction is the projected lateral straggle ΔR_{pL}. This lateral penetration of ions may limit dimensions in some devices [20]. The ion concentration profile in the solid is related to the projected range R_p, standard deviation ΔR_p and ion dose (fluence) Φ, (assuming Gaussian approximation) by

$$N(x) = \frac{\Phi}{\Delta R_p \sqrt{2}} \exp\left[-\frac{(x - R_p)^2}{2\Delta R_p^2} \right] \tag{3.8}$$

The profile given by equation (3.8) is often called Lindhard-Scharff-Schiott (LSS) [21] profiles for implants in semiconductors. The assumption behind the purely Gaussian stopping distribution described by equation (3.8) is that the implantation takes place into amorphous material, which ignores the effects of channeling related to the single crystal nature of the target.

Computer based simulation of implantation profiles are now possible using Monte Carlo-based techniques such as Transport of Ions in Matter (TRIM) [22] and Stopping Range of Ions in Matter (SRIM) [23]. These simulation codes should be treated with caution when used for crystalline material since they assume an amorphous material and ignore the effects of channeling, diffusion effects during and after ion implantation and also do not account for annihilation of vacancies and interstitials and thus overestimates the concentration of vacancies and interstitials produced by the implantation.

3.4.2 Defect Production by Irradiation

It is important to describe the dynamics of collision because it is fundamental to defect production in semiconductors. Assume that an incident particle with kinetic energy E and mass M_1 strikes a target atom of mass M_2.

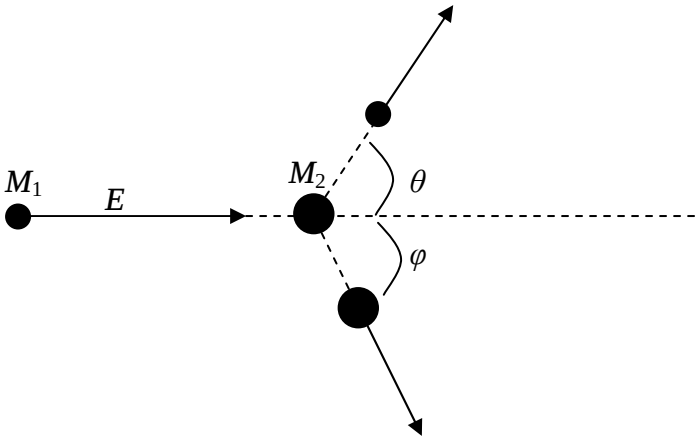

Fig. 3-6. Illustration of the collision between an incident particle of mass M_1 and energy E with a target atom of mass M_2.

The kinetic energy T transmitted to the target atom depends directly on the angular deflection θ of the incident particle (Fig. 3-6). For purely elastic collision, (i.e. when momentum and kinetic energy is conserved) the energy transferred is given by

$$T = 2E\frac{M_1}{M_2}\frac{1-\ (\ )}{(1+M_2/M_1)^2} \tag{3.9}$$

where E is the energy of the projectile and M_1 and M_2 have previously been defined and $\eta(\theta)$ is a function implicitly given by

$$\cos\ = \frac{1+(M_2/M_1)}{\sqrt{1+2(M_2.M_1)\ +(M_2/M_1)^2}} \tag{3.10}$$

In the non-relativistic limit the maximum energy T_{max} is transferred for θ = 0, i.e., for $\eta(\theta)$ = -1, therefore

$$T_{max} = \frac{4M_1M_2}{(M_1+M_2)^2}E \tag{3.11}$$

In the case where the mass of projectile is approximately equal to the target, the expression of the transferred energy will simplify to

$$T_{max} = E \tag{3.12}$$

For a neutron irradiation, $M_1 << M_2$ the energy transferred is now given by

$$T_{max} = \frac{2M_1}{M_2} E \tag{3.13}$$

In the case of electron irradiation, $M_1 << M_2$ relativistic corrections are required and the energy transferred in now written as

$$T_{max} = \frac{2M_1}{M_2} E\left(2 + \frac{E}{M_1 c^2}\right) \tag{3.14}$$

where c is the speed of light. Equation (3.14) can be approximately represented by

$$T_{max} = \frac{2148}{Z} E^2 \tag{3.15}$$

In this case the Z is the atomic number of the target atom, E is in MeV and T_{max} is in eV. In order for an atom to be permanently displaced from its lattice position, the energy that it receives must be greater than the displacement energy. The minimum energy necessary to displace an atom from its lattice position is called the threshold energy (T_d). Normally the threshold energy is assumed to be isotropic (i.e. independent of the direction in which the atom is displaced in the lattice.

Table. 3.1. The threshold energies and corresponding minimum incident electron energies for atom displacement in silicon and germanium.

Material	T_d (eV)[a]	E_{min} (keV)[b]
silicon	21.0	370
germanium	27.5	424

[a]Experimental values obtained from ref. 24.

[b]Values calculated based on equation (3.14).

It should be pointed out that threshold energies for most materials is generally greater than the formation energy of Frenkel pairs, because defect formation is a complex multi-body collision process (e.g. a recoil atom can bounce back to its lattice position or kick back another atom to its lattice position) [25]. Table. 3.1 summarizes the threshold energies and the minimum electron projectile energy E_{min} necessary to displace an atom in silicon and germanium. If an incident particle has energy much greater than the threshold energy (T_d), it will transfer energy to the target atom. The displaced atom may in turn collide and displace other atoms, creating cluster damage, until it eventually comes to rest, usually in an interstitial site and sometimes in a vacancy site. Light energetic particles (such as Si, He, Ar, neutrons, electrons and protons) tend to leave tracks of relative small defect concentrations. These ions initially slow down mainly by electron stopping process with little displacement damage until eventually nuclear stopping becomes dominant at the end of their range.

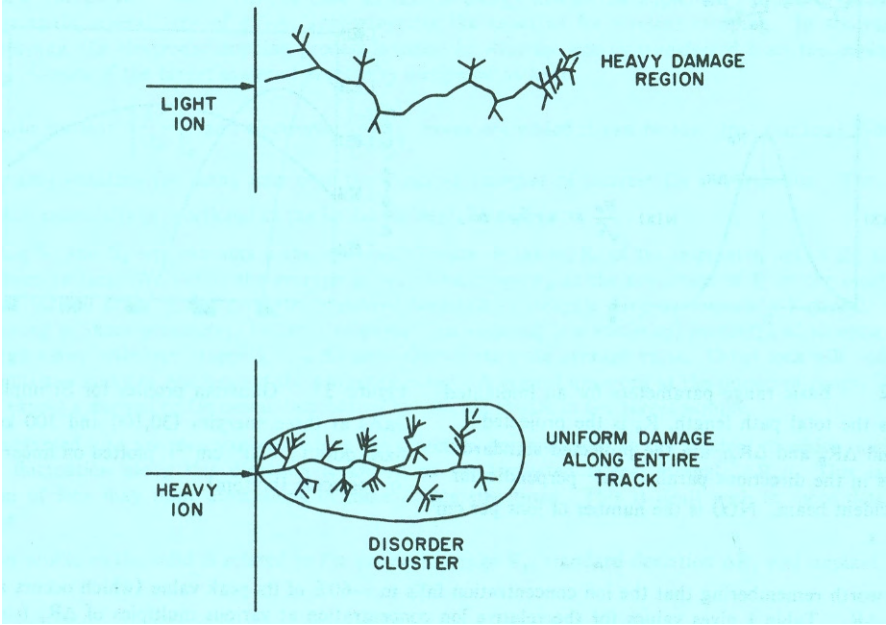

Fig. 3-5. Schematic of ion track in a solid, and associated damage for a light ion (top) and a heavy ion (bottom), redrawn from ref. 20.

Therefore there is generally little lattice damage along the track except for the end of the range. Heavy ions by contrast may create damage clusters along their track. A comparison of lattice damage by light and heavy ions is depicted in Fig. 3-5. The heavy ions may undergo relatively higher degree of nuclear stopping than light ions even right from the surface. The volume of the crystal in which the ion energy is

deposited is usually larger than the volume in which the lattice damage occurs. When the damaged areas start to overlap with increasing ion dose, an amorphous layer can result, which implies that all the nuclei have been displaced from their lattice position and the long range order which describes a crystal is no longer present.

The number of displaced atoms ($N_{\text{disp.}}$) by irradiating ion can be estimated by [26]

$$N_{disp.} \approx \frac{E_n}{2T_d} \tag{3.16}$$

where E_{n} is the total energy deposited in primary and secondary nuclear collisions. The expression in (3.16) should be used with caution, because it overestimates the number of displaced atoms since it overlooks the effects of (i) ion channeling and (ii) vacancy-interstitial recombination.

3.4.3 Defect Annealing Mechanisms

Defect characterization techniques such as deep level transient spectroscopy (DLTS) and photoluminescence (PL) cannot be used to probe the defect structure. The only way to correlate the defect structure obtained from electron paramagnetic resonance (EPR) to the DLTS and PL measurements is by thermal annealing studies. The characteristic temperature at which a defect disappears is the defect's annealing temperature. This annealing temperature is the parameter that allows for results obtained by different techniques to be compared.

The defects annealing mechanism can be classified into two main categories:

(a) Diffusion, as the temperature is increased defects migrate to sinks (e.g. by moving to the surfaces or grain boundaries) or they are subsequently trapped by other defects or impurities (e.g. direct recombination of the interstitial with a vacancy, complex formation or hydrogen passivation) to form new defects. The mean distance between the interstitial and the vacancy depends on the energy deposited by the irradiating particles, thus the annihilation process of the interstitial and a vacancy is mainly related to the irradiation energy [27]. The ability of a defect to migrate through the crystal is determined by the thermal energy of the crystal and its charge state.

(b) Dissociation, which is the breaking-up of the complex defects.

Each of the process i.e. defect migration, recombination, and complex formation is characterized by migration enthalpy or activation energy (E_a). It should be noted that for the simple defects the migration energy for vacancies in a solid is much higher than that for interstitials. At a fixed annealing temperature (T_a) the annealing kinetics can be deduced by monitoring the decrease in defect concentration with time. The defect annealing kinetics can provide information on the defect distribution, annealing mechanism and hence their identity. Consider an irradiated sample with a given defect level with concentration N_T, the number of defects which anneal per unit time is proportional to the number of defects $N_T(t)$ present at time t and thus can be written as

$$\frac{dN_T}{dt} = -Kf(N_T) \tag{3.17}$$

where K is the rate constant and if $f(N_T) = N_T$, then the annealing kinetics is said to be of first order and if $f(N_T) = N_T^2$ then it is of the second order. Solving the differential in equation (3.17) gives annealing kinetics for first order as

$$N_T(t) = N_T(0)e^{-Kt} \tag{3.18}$$

where $N_T(0)$ is the initial defect concentration at $t = 0$. The rate constant K given in equation (3.17) and (3.18) has the form

$$K = K_0 e^{-\frac{E_a}{kT}} \tag{3.19}$$

where k is Boltzmann constant, K_0 is a pre-exponential constant (which contains the vibrational frequency associated with the process) and E_a is the associated activation energy (which might be migration energy, dissociation energy etc depending on the process). Experimentally the activation energy can be obtained from isothermal annealing studies. The variation of N_T versus time is measured at a constant temperature T_1 and a plot of $\ln(N_T)$ vs. t is straight line for first order kinetics which will give a rate constant K_1 from the gradient. If the process is repeated for other constant temperatures T_2 and T_3, then rate constants K_2 and K_3 are obtained respectively. From equation (3.19) a graph of $\ln(K)$ vs. $1/T$ is an Arrhenius plot and

will yield the activation energy E_a for the defect annealing from the gradient and K_0 from the vertical axes intercept.

It is interesting to note that most simple defects anneal out at between 200˚C and 400˚C in silicon, while higher order defects are introduced at higher temperatures between 350˚C and 500˚C. The structure of these higher order defects is critically dependent on the irradiation condition (i.e. irradiation ion energy and ion mass). It has also been shown that the formation of a silicide phase at a metal-Si interface during thermal annealing injects vacancies into the substrate. Thus the silicidation technique can be used to remove interstitial – related defects in processed p-type Si [28].

References

[1] G.L. Miller, D.V. Lang and L.C. Kimerling, *Ann. Rev. Mater. Sci.* **7** (1977) 377.

[2] A. Hallen and M. Bakowski, *Solid-State Electron*, **32** (1989) 1033.

[3] F.D. Auret and P.N.K. Deenapanray, *Crit. Rev. in Sol. State and Mater. Sci.*, **29 (**2004) 1.

[4] M. Lannoo and J. Bourngoin, *Point Defects in Semiconductors I, Theoretical Aspect* Springer series in solid state science 22, (1981).

[5] W. Fank, *Inst Phys. Conf. Ser*. **22**, (1975) 23.

[6] A. Antonelli, E. Kaxiras and D.J. Chadi, *Phys. Rev. Lett.* **81** (1998), 2088.

[7] S.A. Centoni, B. Sadigh, G.H. Gilmer, T.J. Lenosky, T.D. de la Rubia and C.B Musgrave, *Phys. Rev. B* **72** (2005) 195206.

[8] G.D. Watkins, *Mater. Sci. Semicond. Processing* **3** (2000) 227.

[9] J. Coutinho, R. Jones, V.J.B. Torres, M. Barroso, S. Oberg and P.R. Briddon, *J. Phys.: Condens. Matter*. **17** (2005) L521-7.

[10] C. Janke, R. Jones, S. Oberg and P.R Briddon, *Phys. Rev B* **75** (2007) 195208.

[11] A. Mesli, L. Dobaczewski, K. Bonde Nielsen, V.L. Kolkovsky, M. Christian Petersen, and A. Nylandsted Larsen, *Physical Review B* **78** (2008) 165202.

[12] A.N. Larsen and M. Mesli, *Physica B*, **401-402** (2007) 85-90.

[13] V. Rianeri, G. Fallica and S. Libertino, *J. Appl. Phys*. **79** (1996) 9012.

[14] G.D. Watkins, in: Hulin (Ed.), *Radiation Damage in Semiconductors*, Dunod, Paris, 1964, p97.

[15] G.D. Watkins, *Phys. Rev. B* **12** (1975) 5824.

[16] T. Markvart, D.P. Parton, J.W. Peters and A.F.W. Willoughby, *Materials Science Forum* **143-147** (1994) 1381.

[17] W. Schockley and W.T. Read, *Phys. Rev*. **87** (1952) 835.

[18] J. Lindhard, V. Nielsen, M. Scharff, and P.V. Thompsen, *Kgl. Dan. Vid. Selsk, Mat. Fys. Medd.* **33** (1963) 10.

[19] J. Lindhard and M. Scharff, *Phys. Rev.* **124** (1961*)* 128.

[20] S.J. Pearton, *Solid State Phenomena*, Vol. **1-2** (1988) 247.

[21] J. Lindhard, M. Scharff, and H. Schiott, *Kgl. Dan. Vid. Selsk, Mat. Fys. Medd.* **33** (1963) 14.

[22] J.P. Biersack and L.G. Haggmark, *Nucl. Instrum. Methods* **174** (1980) 257.

[23] J.F. Ziegler *"The Stopping and Range of Ions in Matter"* Vol 2-6, Pergamon Press, 1977-1985

[24] M. Lannoo, J. Bourngoin, *Point Defects in Semiconductors II, Experimtal Aspect* Springer series in solid state science 35, (1983).

[25] H. H. Andersen, *Appl. Phys.* **18**, (1979) 131.

[26] G.H. Kinchin and R.S. Pease, *Rep. Prog. Phys.* **18** (1955) 1.

[27] A. Mesli, L. Dobaczewski, K. Bonde Nielsen, V.L. Kolkovsky, M. Christian Petersen and A. Nylandsted Larsen, *Physical Review B* **78** (2008) 165202.

[28] Dong-Zhi Chi and S. Ashok, *Mat. Res. Soc. Symp. Proc.* 442 (1983).

Chapter 4

DLTS and Laplace-DLTS Aspects

4.1 Introduction

Deep level defects can be detrimental to or enhance the operation of devices fabricated on semiconductors as discussed in the earlier chapter. Therefore, it is essential to develop a sensitive experimental tool for characterizing the deep level defects in a semiconductor. The deep-level transient spectroscopy (DLTS) is a high-frequency (1 MHz) transient capacitance technique, which has proved to be a very useful tool to probe the defects close to the semiconductor surface since it was first discovered by Lang in 1974 [1,2]. Recently, high-resolution Laplace-DLTS (LDLTS) [3-4], which greatly enhances the resolution and spectroscopic nature of capacitance based defect characterization tools has been developed. In this chapter the emission and capture of carriers form deep level defects is discussed in section 4.2, the DLTS and LDLTS theory is presented in sections 4.3 and 4.4 respectively. The electric field effect on the deep levels is discussed in section 4.5.

4.2 Emission and Capture of Carriers from Deep Levels

The fabrication and development of efficient semiconductor devices require prior knowledge of the properties of deep levels as carrier traps or generation-recombination centers. As mentioned in the previous chapter, the generation-recombination centers can reduce minority carrier lifetime and diffusion length which may, for example, limit bipolar transistor performance [5], reduce the efficiency of photovoltaic cells [6] or increase the switching speed in semiconductor switches. A defect level can be defined as an electron trap if, when it captures an electron from the conduction band the electron stays there until it is re-emitted back to the conduction band. This may occur for an empty level when the electron capture rate c_n, from the conduction band is much larger than the hole capture rate c_p from the valence band,

i.e. $c_n \gg c_p$. Conversely, a recombination center is one for which c_n and c_p are almost similar, i.e. $c_n \approx c_p$. According to Shockley and Read [7] a deep level almost always changes its electron occupancy via carrier transitions between the level and the bands. Figure 4-1 shows the four common processes, neglecting transfer between the deep levels. The figure shows a trap which may exist in either two states, negative or neutral. Similar treatment is possible for other pairs of two states, e.g. neutral and positive or negative and double negative. If a trap is neutral it may capture an electron from the conduction band Fig. 4-1 process (a) or it may capture an electron from the valence band process (d) leaving behind a hole (hole emission). Processes (b) and (c) are electron emission and hole capture respectively.

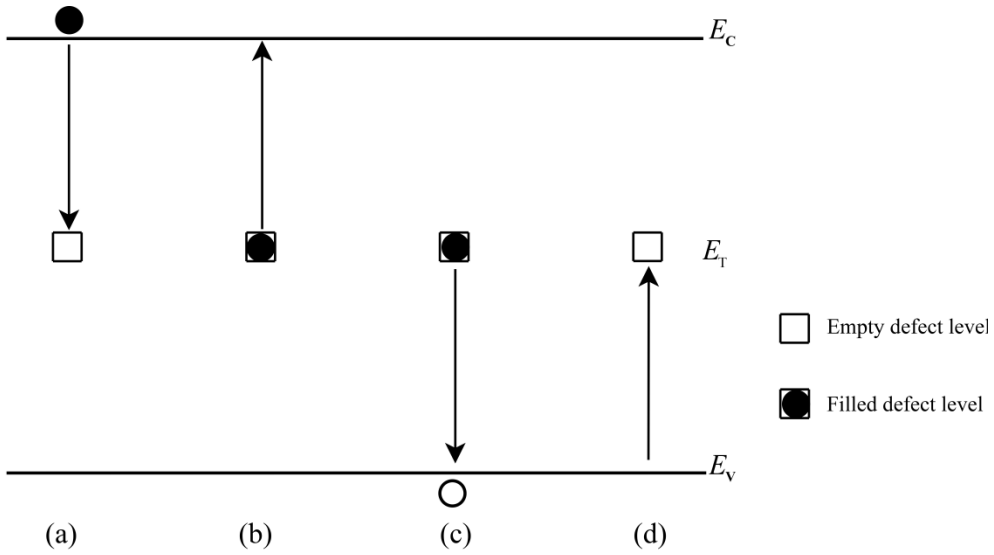

Fig. 4-1. Schematic representation of transitions of carriers between deep states (E_T) and the valence (E_V)- and conduction (E_C)- bands, neglecting the transfer between deep levels (a) electron capture, (b) electron emission, (c) hole capture, (d) hole emission. The arrow indicates the transition of the electron in the process (redrawn from ref. 7).

The kinetics which governs the charge transfer between the deep level and the bands are fully described by the Shockley-Read-Hall [7,8] (SRH) model. The model is developed assuming thermal (or near thermal) equilibrium and studying of deep level by DLTS uses the perturbation of the occupancy of the levels and then monitoring the return to equilibrium. The electron capture rate is given by

$$c_n = {}_n\langle v_n \rangle n \tag{4.1}$$

where σ_n, is the defect's electron capture cross-section, n is the electron concentration in the conduction band and $\langle v_n \rangle$ is the average thermal velocity of free electrons which is given by

$$\langle v_n \rangle = \sqrt{3kT / m^*} \tag{4.2}$$

where m^* is the effective mass of the electron, k is the Boltzmann constant, and T is the temperature in Kelvin. Similarly, the hole capture rate is given by

$$c_p = {}_p\langle v_p \rangle p \tag{4.3}$$

where σ_p, is the defect's hole capture cross-section, p is the hole concentration and $\langle v_p \rangle$ is the thermal velocity of the holes. A similar expression to that of $\langle v_n \rangle$ in equation (4.2) can be written for $\langle v_p \rangle$. The thermal emission rate e_n, of electrons from traps to the conduction band is proportional to the Boltzmann factor exp(-E_T/kT), and can be expressed as a function of temperature by [5,6,9]

$$e_n(T) = \frac{{}_n\langle v_n \rangle N_C}{g} \exp\left[-\frac{E_T}{kT}\right] \tag{4.4}$$

where $E_{T,}$ is the energy level below the conduction band minimum (also referred to as the defect activation energy if one assumes that σ is temperature independent), g is the degeneracy of the defect level, T is the temperature in Kelvin, N_C is the effective density of states in the conduction band given by

$$N_C = 2M_C\left(\frac{2\ m^* kT}{h^2}\right)^{3/2} \tag{4.5}$$

here M_c is the number of conduction-band minima, h is Planck's constant.

An analogous expression can be written for hole emission rate e_p, to the valence band. In equation (4.4), the terms $\langle v_n \rangle$ is proportional to $T^{1/2}$, and N_C is proportional to $T^{3/2}$, while σ_n may or may not be temperature dependent, thus the product $\langle v_n \rangle N_C$ has T^2 dependence. If e_n is measured as a function of temperature and ignoring the temperature dependence of σ_n, an Arrhenius plot of $\log(e_n / T^2)$ against $1/T$ is a straight line which yields E_T from the slope and σ_{na}, the apparent capture cross-section (from intercept at $T^{-1} = 0$). The parameters E_T and σ_{na} are often referred to as the '*defect signature*'. If a temperature-dependent capture cross-section is assumed then it usually takes the form [4]

$$_n(T) = \ _\infty \exp\left[\frac{\Delta E}{kT}\right] \tag{4.6}$$

where σ_∞, is the capture cross-section extrapolated to $T = \infty$ and ΔE_σ is the thermal activation energy of the capture cross-section (i.e. thermal barrier for carrier capture). The cascade capture into shallow levels and multiphonon capture into deep levels are some of the possible contributing factors to capture cross-section temperature dependence [10]. The temperature dependence of the capture cross-section may be determined from the plot of $\log(\sigma_n)$ vs. $1/T$, where ΔE_σ, is extracted from the slope and σ_∞ after extrapolation to $T = \infty$. Thus, the modified activation energy for a deep level which exhibits a temperature-dependent capture cross-section can be written as,

$$\Delta E_a = E_T + \Delta E \tag{4.7}$$

The modified activation energy has two components; (i) the energy difference between the trap level and the bottom of the conduction band E_T, and (ii) the thermal activation energy of the capture ΔE_σ, as depicted in Fig. 4-2. A more general expression of the thermal emission rate is now given by,

$$e_n(T) = \frac{_n\langle v_n \rangle N_C}{g} \exp\left[-\frac{E_T + \Delta E}{kT}\right] \tag{4.8}$$

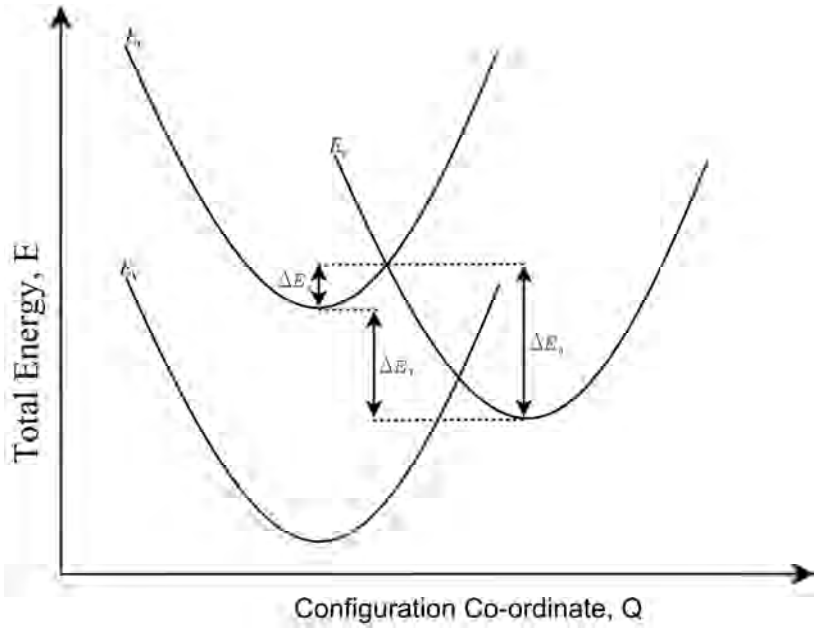

Fig. 4-2. Configuration co-ordinate (CC) diagram depicting the energy level of the defect below the conduction band ΔE_T (=E_T), the thermal activation energy of the capture cross-section ΔE_σ, and the total energy an electron requires to escape from the trap level to the conduction ΔE_a, redrawn from ref. 6.

In this study, the defect characterization is based on E_T (the position of the defect level from the band edge) and σ the apparent capture cross-section, therefore great care should be taken when these thermal emission measurements are compared with results from other techniques, e.g. optical measurements.

The physical meaning of E_T is that it is the Gibbs free energy change for the ionization of the state given by [11]

$$E_T = \Delta H - T\Delta S \tag{4.9}$$

where ΔH and ΔS are the changes in enthalpy and entropy due to the change in charge state of the level. Substituting equation (4.9) into (4.4) yields

$$e_n(T) = \frac{{}_n\langle v_n \rangle N_C}{g} \exp\left[-\frac{\Delta S}{k}\right] \exp\left[-\frac{\Delta H}{kT}\right] \tag{4.10}$$

Therefore, the Arrhenius plot yields the activation enthalpy of the deep level, and not the free energy, which can only be determined from optical measurements [6,9].

4.3 Deep Level Transient Spectroscopy (DLTS)

The conventional deep level transient spectroscopy (DLTS) is a powerful high frequency (MHz range) capacitance transient thermal scanning technique that is used to probe the space-charge region of a p-n junction, Schottky diode or MOS device structure. This technique is based on the transient capacitance change associated with the thermal emission of charge carriers from a trap level to thermal equilibrium after an initial non-equilibrium condition in the space-charge region. The DLTS technique offers the following characterization features:

(a) High sensitivity and good resolution.

(b) Straight forward, easy analysis of spectra and rapid scanning.

(c) Capability of measuring over a wide range of depths in the forbidden gap and detection of very shallow levels.

(d) Spectroscopic nature (i.e. signals due to different traps can be resolved from one another) [1].

A DLTS scan reveals each trap by a positive or negative peak on a flat base-line plotted as a function of temperature. The sign of each peak indicates whether it is due to a majority- or minority- carrier trap and positions of the peaks are simply and uniquely determined by the instrument rate-window and the thermal emission properties of the respective trap [1]. It is also possible to extract the thermal emission rate, activation energy, concentration profile and capture cross-section of each trap from the DLTS measurements. Since all the experimental work on defect levels studies in this study was based on the depletion region formed by the Schottky diode on a semiconductor, the discussion below will be confined to capacitance transient within the space-charge region of a Schottky barrier diode.

4.3.1 Capacitance Transient Processing

The relationship between capacitance and depletion width for a Schottky barrier diode has been dealt with in detail in chapter 2. The depletion width W is given by

$$W = \sqrt{\frac{2\ _s}{qN_D}(V_{bi} - V_a)} \qquad (4.11)$$

where, N_D is the density of ionized impurities due to dopants and other defects with levels in the band gap, q is the electronic charge, ε_s is the permittivity of the semiconductor, V_{bi} is built-in potential, and V_a is an externally applied voltage. The corresponding junction capacitance is

$$C = A\sqrt{\frac{q\,\varepsilon_s N_D}{2(V_{bi} - V_a)}} = \frac{A\,\varepsilon_s}{W} \qquad (4.12)$$

where A, is the area of the junction. The capacitance of the depletion region depends on the applied bias voltage and the dopant concentration as shown in equations (4.11) and (4.12). It is the sensitivity of the capacitance to the change in charge in the depletion region that is exploited and forms the basis of DLTS.

In the derivation of the depletion width equation, the depletion approximation has been used, which assumes that the semiconductor can be divided into two distinct regions, i.e. the bulk region which is electrical neutral and the space charge region which is depleted of charge carriers. In a real junction, as depicted in Fig. 4-3, there is a region λ, which lies between the truly depleted region and the bulk region. This region is defined as the distance between the depletion region edge and the point where the deep levels E_T crosses the Fermi level E_F. Fig. 4-3 also illustrates the energy band diagrams and space charge for a metal-n-type semiconductor with deep donors for (a) unbiased junction and (b) after applying a bias voltage V_a. In equilibrium, and under zero bias, deep levels in the region λ are below the Fermi level and therefore filled with carriers (a). After applying a reverse bias V_a the depletion region increases, the space charge region is altered, thus decreasing the capacitance of the depletion region. The deep levels N_T and shallow dopants N_D contribute to the charge density ρ in the depletion region and only the shallow dopants N_D are the source of the charge density in the region λ.

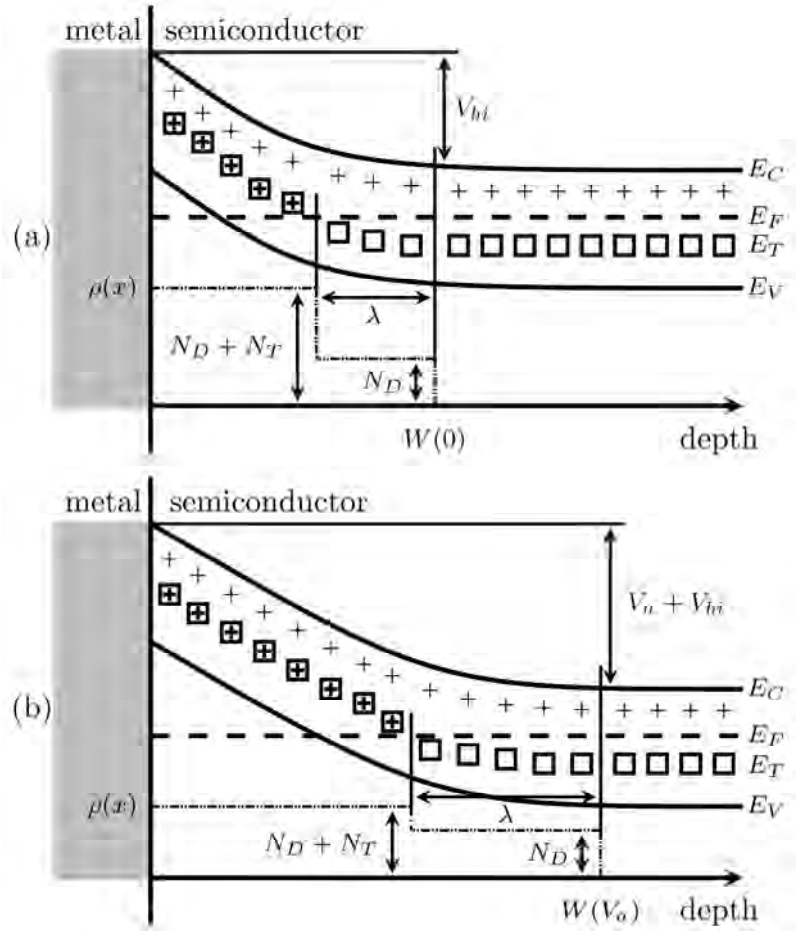

Fig. 4-3. Energy band diagram, the region λ, and space charge for an n-type metal-semiconductor junction with deep donor levels for (a) an unbiased and (b) after applying a quiescent reverse bias of V_a. For each condition the corresponding charge density ρ distribution is also shown, after ref. 14.

If the concentration of holes and electrons trapped at the deep levels is altered, (by say thermally stimulated emission of the carriers to the conduction or valence band), then this change can be monitored by measuring the junction capacitance or capacitance transient at constant applied bias voltage [6,12]. To ensure that the deep levels are filled with charge carriers after thermal stimulated emission, continuous refilling of the deep levels is achieved by application of a repetitive voltage filling pulse superimposed on a constant reverse bias voltage. The variation of the depletion region width and capacitance after the application of a voltage bias and a filling pulse sequence for majority and minority carrier traps in n-type semiconductor (e.g. n-type Ge) is depicted in Fig. 4-4 and Fig. 4-5 respectively. For simplicity, the bending of the bands due to the electric field in the space charge region has not been indicated. Also

the lambda effect has been ignored, so it is assumed that the defect levels in the depletion region are above the Fermi level and those deeper than the depletion region are beneath the Fermi level.

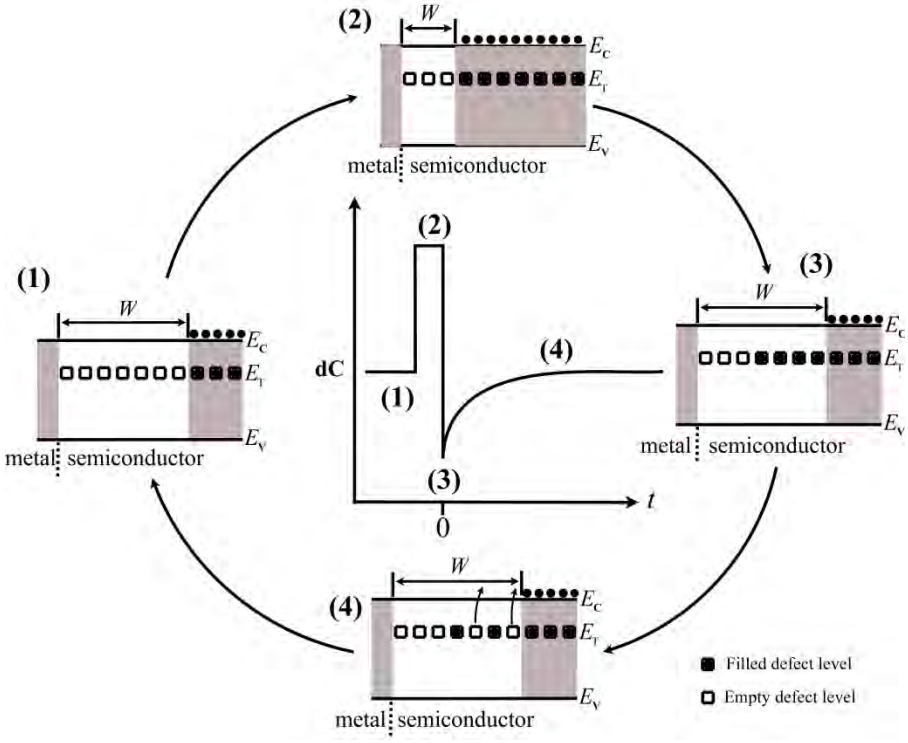

Fig. 4-4. Variation of the depletion region width and capacitance after the application of a voltage bias and a filling pulse sequence for a majority carrier (electron) trap in n-type semiconductor, after ref. 6.

The capacitance transient resulting from the pulse sequence is shown in the center. Under a quiescent reverse bias V and steady state, Fig. 4-4 part (1), the deep levels under the Fermi level are assumed filled and those above are empty as governed by the Fermi distribution function. The empty deep levels in the band gap are indicated by empty squares. After applying a majority carrier filling pulse in part (2), the depletion width is reduced, trapping electrons in those levels that are now below the Fermi level, symbolized by the solid squares. It is assumed here that the pulse width t_p is long enough to allow the complete filling of the trap levels. There is a corresponding step increase in capacitance because of the reduced depletion width. Immediately after the pulse is removed and the quiescent reverse bias V restored, part (3), the filled states lie within the depletion region, above the Fermi level, therefore the levels will start emitting the trapped carriers with a characteristic rate to the

conduction band where they are instantaneously swept away by the junction electric field, part (4).

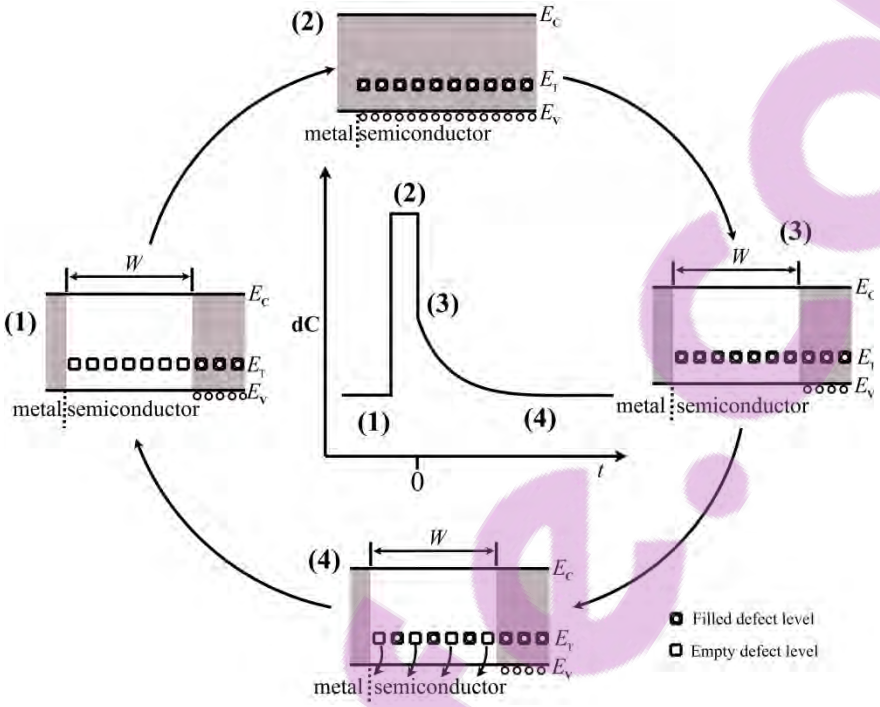

Fig. 4-5. Variation of the depletion region width and capacitance after the application of a voltage bias and a filling pulse sequence for a minority carrier (hole) trap in n-type semiconductor.

The capacitance variation as the trapped carriers are emitted to the conduction band is the so-called majority capacitance transient. The emission rate can be determined from the time dependence of the capacitance transient. The density of occupied defect levels at time *t* after removing the filling pulse is given by [6]

$$N(t) = N_T \exp(-e_n t) \tag{4.13}$$

where e_n is the electron thermal emission rate and N_T is the trap concentration junction capacitance, if $N_T \ll N_D$, can then be given by an exponential time varying function as

$$C(t) = C_o - \Delta C_o \exp(-e_n t) \tag{4.14}$$

here C_o is the equilibrium reverse bias capacitance and ΔC_o the change in capacitance immediately after the removal of the pulse, i.e. at $t = 0$ as shown in Figs. 4-4 and 4-5. When a large enough pulse is applied such that the junction is forward biased, (minority carrier injecting pulse), Fig. 4.5 part (2) and part (3), minority carriers (holes in this case) are trapped. After removing the pulse and the quiescent reverse bias V restored, part (4), the trapped carriers are emitted to the valence band giving rise to the minority carrier capacitance transient, which is of opposite sign to the majority carrier transient.

4.3.2 DLTS Principles

The utility of DLTS is in the processing of the capacitance transients obtained after repeated pulsing sequence discussed in section 4.3.1. The basic idea of DLTS method can be represented by the illustration in Fig. 4-6. The system response occurs only when the emission rate of the trap falls within the 'rate window'. For a given rate window, the system response is shifted to higher temperatures for a trap with higher emission rate and hence the system can resolve signals from different traps as a function of temperature, as shown in Fig. 4-6.

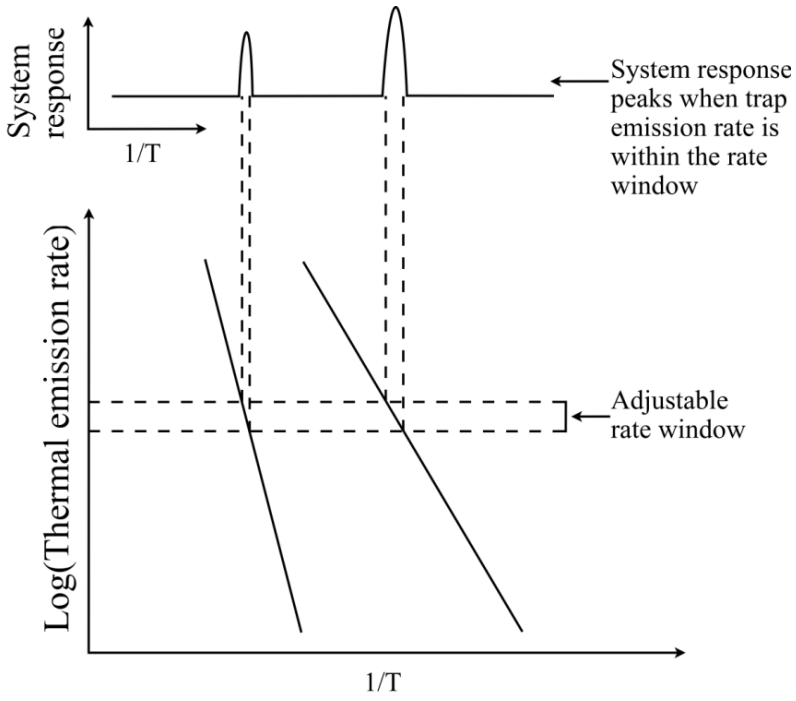

Fig. 4-6. A Schematic illustration of how a rate window produces a peak in its response when the emission rate of the input signal matches the rate selected by the window, redrawn from ref. 1).

In consequence, DLTS has the ability to set up an emission 'rate window' so that the measurement system gives an output only when a transient with a rate within this narrow window occurs. Since the emission rate is strongly temperature dependent, a thermal scan can reveal the presence of different traps at characteristic temperature when their emission rates coincide with the window. Most early DLTS systems used the dual-gated (double boxcar) signal filter for determining the rate window and averaging transients to enhance the signal-to-noise ratio (SNR) of the output, enabling low concentration defects to detected [1,9]. As the temperature is scanned, the filter takes samples of the transients at preset times t_1 and t_2 and produces an output proportional to their average difference, as shown in Fig. 4-7(a). Thus, the rate window is determined by the values of t_1 and t_2. The output signal changes from a small response as the decay time constant ($\tau = 1/e$) moves into the range detectable by the filter, to a maximum, and then drops as the decay time constant again falls outside the filter detectable range, giving rise to a DLTS spectrum depicted in Fig. 4-7(b). The early analog filter design by Lang [1] had an intrinsic dc rejection mechanism, which would give a zero output on the filter when no defect is detected. The normalized DLTS signal $S(T)$ is defined by

$$S(T) = \frac{C(t_1) - C(t_2)}{\Delta C(0)} \tag{4.15}$$

where $C(t_1)$ is the capacitance at t_1, $C(t_2)$ is the capacitance at t_2, and $\Delta C(0)$ is the capacitance change due to the filling pulse at $t = 0$ as described in figures 4-4 and 4-5. The position of the peak on the temperature axis depends on the rate window, e.g. a smaller rate window will shift a defect peak to lower temperatures. If DLTS spectra is produced by using different rate windows, then a series of spectra are produced as shown in Fig. 4-8(a). The emission rate at a maximum peak height is a uniquely defined and can be calculated via the expression for the time constant, (τ_{max}) at maximum peak height

$$_{max} = \frac{t_1 - t_2}{\ln\left(\frac{t_1}{t_2}\right)} \tag{4.16}$$

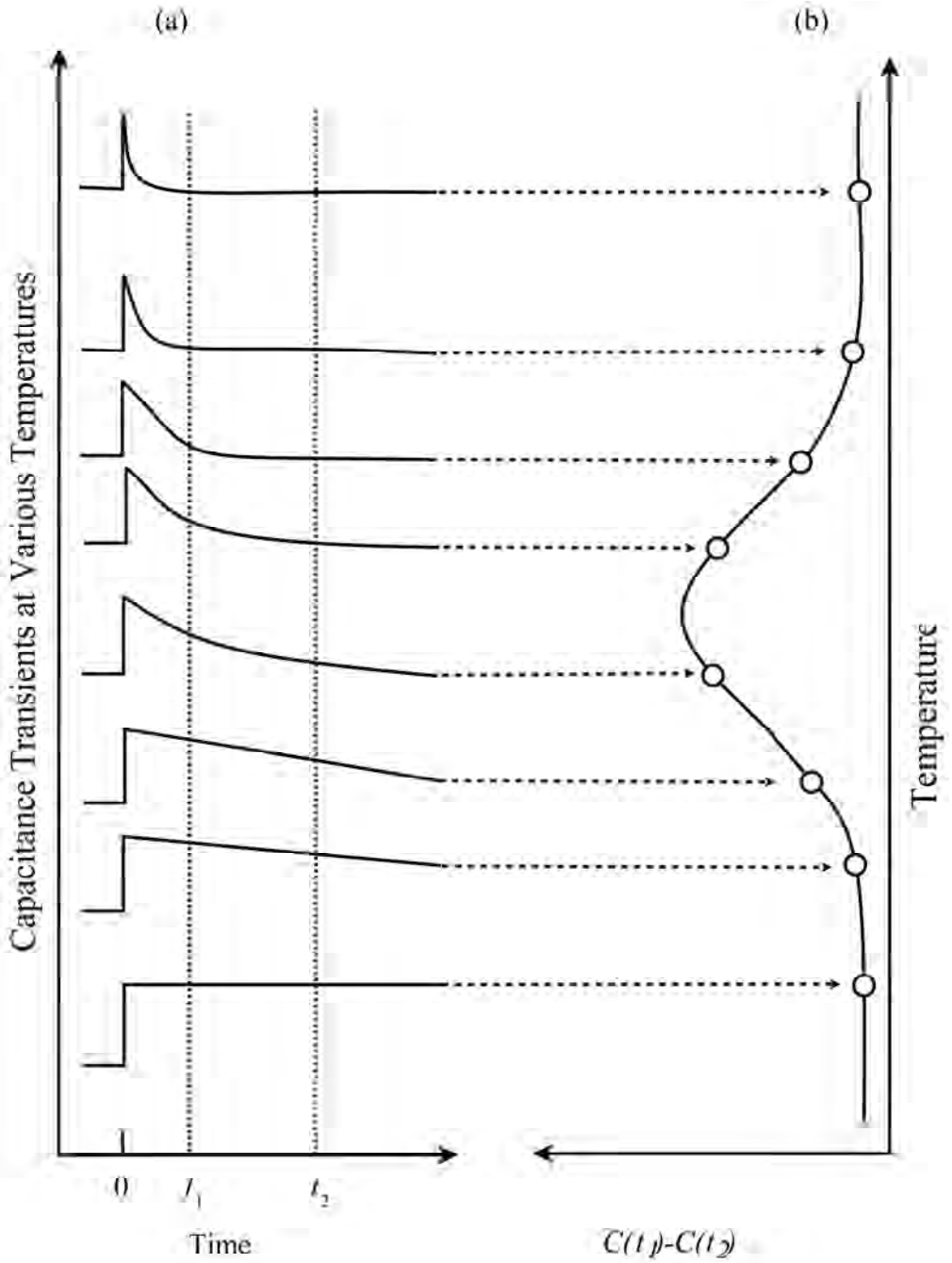

Fig. 4-7. A schematic diagram which shows how a rate window concept can produce a DLTS spectrum. Part (a) shows the capacitance transients at different temperature which after processing with a double boxcar, and thereby resulting in the spectra shown on part (b), after ref. 1.

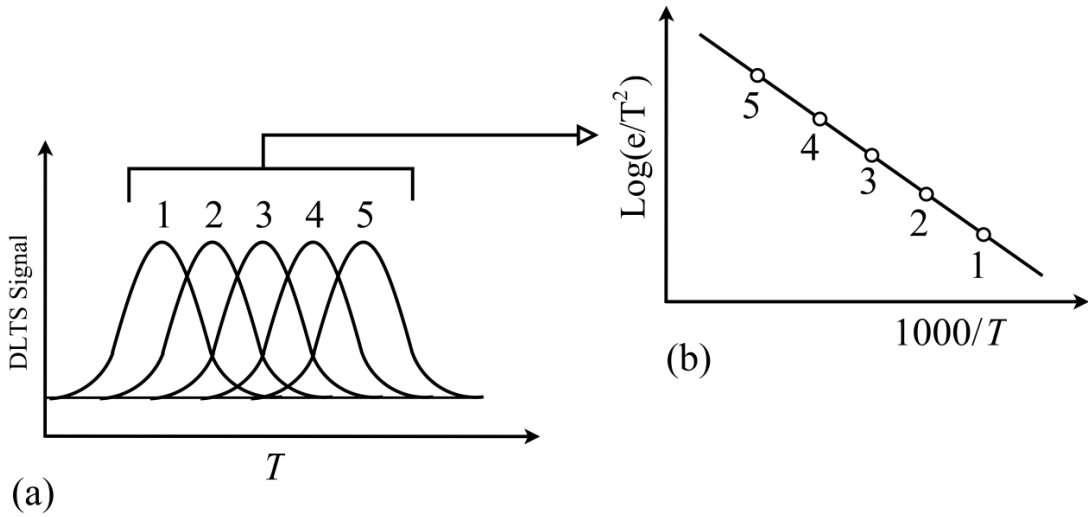

Fig. 4-8. A diagram showing the (a) DLTS spectra at various rate windows and (b) the Arrhenius plots obtained from the spectra, after ref. 1.

For each spectrum, the temperature at the maximum peak height can be measured and the emission rate e, for which the DLTS system shows a maximum response, is calculated via equation (4.16). These points are then used to plot a semi-log graph of $\log(e/T^2)$ vs. $1000/T$, (Arrhenius plot), shown on Fig. 4-8(b) from which the defect activation energy E_T and apparent capture cross-section σ, are extracted.

An alternative to the double boxcar weighting function used in the original Lang's work [1] is to use a lock-in amplifier (LIA) [13]. In a LIA set-up the rate window is set by altering the frequency of the filter. The LIA response to this transient is the integral product of the capacitance signal and the weighting function $w(t)$ given by

$$S(\ ) = \frac{1}{}\int_0 C(t)w(t)dt \qquad (4.17)$$

where $w(t) = \sin\left(\frac{2\ t}{}\right)$ is a sine wave of fixed frequency. The LIA gives the same result to that of the double boxcar method. For an exponential transient, using a sine wave weighting function the DLTS signal reaches a maximum when $= \left(\frac{1}{0.423}\right)$.

4.3.3 Defect Depth Profiling

The DLTS peak height is directly proportional to the concentration of a deep level, therefore the concentration can be obtained directly from the capacitance change corresponding to completely filling the trap with a saturation minority carrier pulse (in case of a minority carrier trap) or the largest possible majority-carrier pulse (in case of a majority-carrier trap). DLTS enables one to determine the defect spatial distribution within the semiconductor and thereby other parameters such as the introduction rate.

The concentration of deep levels N_T is often calculated by using simple expression [1,14]

$$N_T = \frac{2\Delta C(0)}{C} N_D \tag{4.18}$$

where N_D is the concentration of shallow impurities, C is the junction capacitance under quiescent reverse-biased conditions, and $\Delta C(0)$ is the capacitance change due to the pulse at t = 0 (i.e. just after removing the filling pulse). Equation (4.18) is only applicable if the minority carrier pulse or majority carrier pulse is large and long enough to completely fill the trap and when $\Delta C(0) \ll C$. The correct pulse for defect concentration determination can be checked by making several scans with increasing larger and longer pulses until the defect peak no longer increases in size. As has been pointed out in the past [1,14] using equation (4.16) sometimes results in significant underestimation of N_T especially for thin films and at low reverse bias voltages. In order to determine the corrected expression for N_T one has to consider the region λ (the so called λ effect), where the defect level crosses the Fermi level a distance λ shallower than the depletion region edge as shown in Fig. 4-3(b). The traps in this region are occupied and do not contribute to the change in capacitance when a filling pulse is applied. The width of the transition is given by [14]

$$= \left[\frac{2\ (E_F - E_T)}{q^2 N_D} \right]^{1/2} \tag{4.19}$$

where ε is the semiconductor dielectric constant, E_F is the Fermi level and q is the electronic charge. To obtain the deep level distribution profile, the deep levels in the region to be profiled must be filled with carriers. The depth profiling technique used in this study uses a fixed bias voltage and a variable filling pulse (fixed bias-variable pulse method) [15]. In the fixed bias-variable pulse method the incremental change in capacitance $\delta(\Delta C)$ is monitored as the majority carrier pulse V_p is changed by a small amount δV_p. The relative incremental change in capacitance due to the pulse increment can be expressed by [14]

$$\Delta\left(\frac{\Delta C}{C}\right)=\left(\frac{}{qw^2N_D}\right)\frac{N_T(x)}{N_D(x)}\Delta V_p \tag{4.20}$$

where x is the depth below the junction, N_D and w are the ionized shallow impurity concentration and depletion region width, respectively, corresponding to quiescent reverse biased conditions. The shallow impurity profile $N_D(x)$ is obtained from C-V measurements. The total signal due to the majority carrier pulse, is then determined by double integration of the Poisson equation according to a detailed derivation by Zohta and Watanabe [14], to give the corrected deep level concentration expression as

$$N_T=\frac{2\Delta C(0)N_D(x)}{C}\left[\left(\frac{x-}{x}\right)^2-\left(\frac{x_p-\ _p}{x}\right)^2\right]^{-1} \tag{4.21}$$

here x - λ and $x_p - \lambda_p$ are the depletion region widths before and after applying a filling pulse respectively, and λ is distance from where the deep levels cross the Fermi level to the depletion region edge and λ_p is the value of λ during the pulse. In the limit and low noise measurements, values of 10^{-5}-10^{-6} for $\Delta C/C$ can be achieved and if the shallow dopants concentration is $N_D \approx 10^{16}$ cm^{-3}, a low defect concentration of the order of 10^{10} cm^{-3} is detectable.

4.4 Laplace-DLTS

Since its discovery almost 35 years ago, conventional deep level transient spectroscopy (DLTS) has been a valuable tool in identifying deep level states in

semiconductors, thereby improving device efficiency. Unfortunately this technique has limitations in the details of information on the identity of defects it can measure due to its poor emission rate resolution. The double boxcar or lock-in-amplifier filter used in DLTS exhibit good sensitivity but has poor time constant resolution. Due to this poor time constant resolution, DLTS cannot be used to separate closely spaced transients, and thus its inability to study defect fine structure. Over the past 25 years there has been much effort applied to improve DLTS resolution by developing different weighting functions [16]. These higher order filters showed an improvement of resolution by a factor of up to 3 but at the expense of noise performance.

In 1990, Dobaczewski *et al* [3,4] developed an improved high-resolution version of DLTS, called Laplace-DLTS (LDLTS). This new concept is an isothermal DLTS technique and employs a regularized inverse Laplace transform instead of the conventional boxcar analysis. This results in an order of magnitude improvement in emission rate resolution in the studies of the thermal emission of carriers from deep states. Consequently, LDLTS can separate closely spaced transients (with emission rates differing by a factor greater than 2) when a number of defects with similar emission characteristics are present, thereby overcoming the major deficiency of DLTS. Apart from the remarkable sensitivity (ability to measure very low concentrations of defects), LDLTS can probe very narrow regions of the semiconductors (e.g. regions of shallow implants) and can also be used to study selectively the active regions of devices.

4.4.1 Laplace-DLTS Principles

Generally, in DLTS there are two main classes of transient processing methods, which are analog and digital signal processing. Analog signal processing is a real-time process which involves extracting the capacitance transients as the temperature is ramped. An Analog filter will then produce an output proportional to the signal input at a particular time constant range. In order to increase the resolution and sensitivity of DLTS, several different filters have been investigated which include, boxcar [1], lock-in amplifier [13], exponential [17] and multiple boxcar [18]. The digital signal processing involves digitizing the transient output of the capacitance meter, normally done with sample held at a fixed temperature and averaging many of these digitized transient to reduce noise. If the transient is digitized, then it is much easier to apply

signal processing tasks, even complex ones. The concept of digitizing capacitance at constant temperature and extracting the time constant is the basis of high resolution Laplace-DLTS. The extraction of all accessible time constants from the transients is achieved by numerical algorithm. There is a well-documented problem associated with the extraction and separation of multiple, closely spaced time constants. The problem is finding a suitable choice of algorithm to use in the extraction of the time constants. The problem is due to several factors, including that (i) the exponential decay transient baseline is not known with any degree of precision; hence this becomes an unknown variable in the analysis, (ii) both polarities of the transient may be present simultaneously and (iii) exponential transients are not ideal (due to dependence of the emission rate on electric field or due to inhomogeneous strain which produces a continuum of emission rates for a particular defect). Several algorithms that have been developed in an attempt to solve the transient extraction problem have been reviewed [4,6]. The techniques considered include, "a method of moments" by Ikossi-Anastasiou *et al* [19], "a Gaver-Stehfest approximation algorithm to effect a Laplace transform" by Nolte *et al* [20], and "Tikhonov regularization method" to separate the constituent exponentials in a photo-induced current transient spectroscopy (PICTS) signal by Eiche *et al* [21]. The Tikhonov regularization method uses a similar approach to the technique employed with the Laplace-DLTS work discussed here. To develop an algorithm for transient processing, assume that the recorded transient $f(t)$ is a non-exponential transient, which is composed of a superposition of exponential transients and is given by

$$f(t) = \int_0^\infty F(s)e^{-st}ds \qquad (4.22)$$

where $F(s)$ is the spectral density function. The function $f(t)$ given in equation (4.22) is the Laplace transform of the true spectral density $F(s)$. Thus, to find the true spectrum of emission rates in the transient, an inverse Laplace transform for the function $f(t)$, should be performed using some numerical method. For such a procedure, (assuming that all the decay transients are exponential and have the same sign), a spectrum of delta-like peaks is produced for multi-, or mono-exponential transients. All the numerical methods used in LDLTS attempt to find a spectral function with the least possible number of peaks, which is consistent with the data and

experimental noise [4]. Although the problem has been described in a general way, it should be noted that equation (4.22) does not have a general solution for any given function $f(t)$. For an analytical multi-exponential function such a solution exists and, according to Lerch's theorem [22] it is unique. However, if noise is superimposed on this function the number of solutions can be infinite. Therefore, the problem is to find the best estimate for $F(s)$, and according to the prior knowledge about the system being investigated and its boundary conditions, to exclude unphysical solutions and choose only the simplest one, i.e. the one that reveals the least amount of detail or information that was not already known or expected [3,6].

(a)

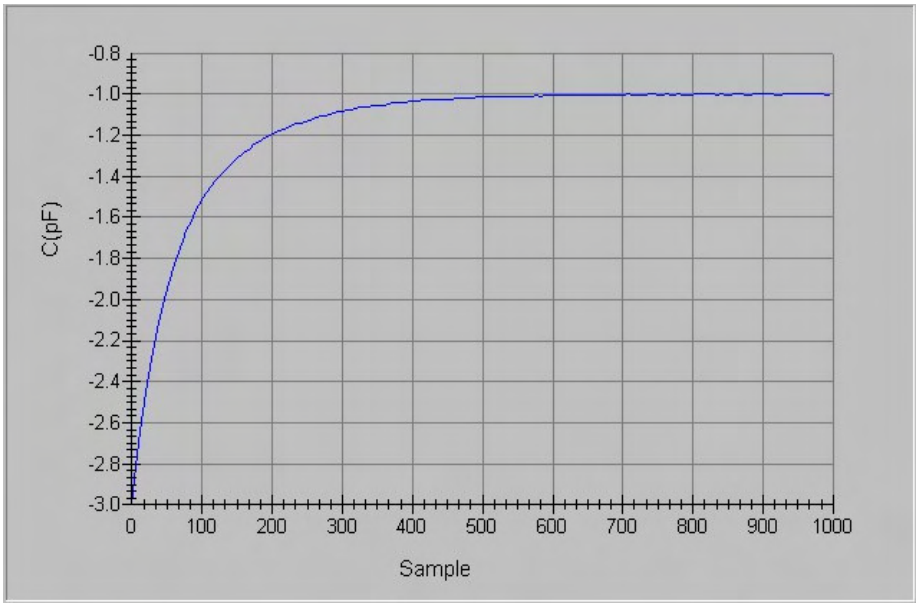

(b)

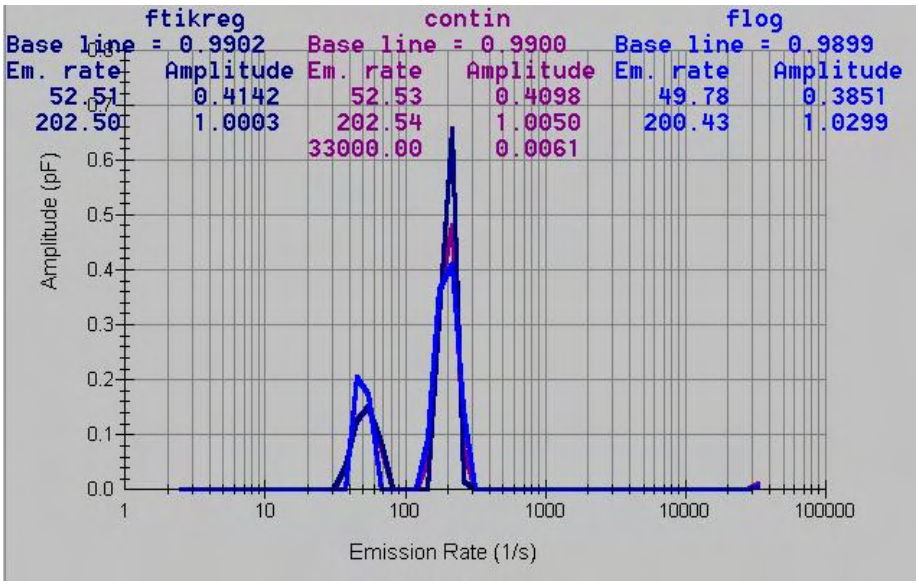

Fig. 4-9. (a) A majority-carrier capacitance transient and (b) the corresponding spectra obtained from the transient with use of the three numerical routines.

For Laplace transform inversion in the Laplace DLTS system used here, three numerical routines CONTIN [23], FTIKREG [24] and FLOG (which was specifically developed for Laplace DLTS by Matulis [25]), all of them based on the Tikhonov regularization method, however they differ in the way the principle for finding the regularization parameters are defined. The Laplace card sets the sample excitation parameters (or in some cases is used to trigger the external pulse generator, which supplies the biasing and pulsing conditions to the sample). The Laplace software then acquires the capacitance transient, shown in Fig. 4-9, graph (a) before the transient is converted into the LDLTS spectra depicted in graph (b) using the three numerical routines, i.e. CONTIN, FTIKREG and FLOG and from the spectra, the emission rates and magnitude of the signal can be measured.

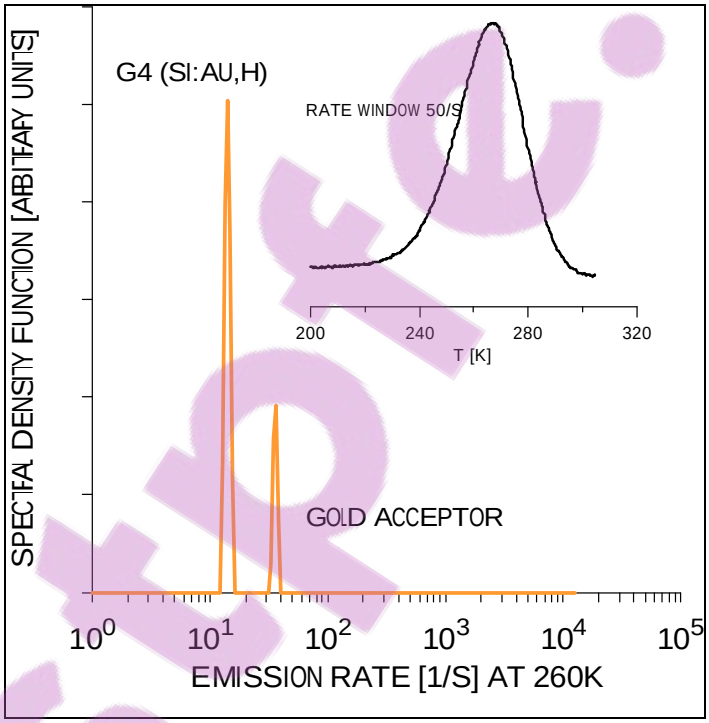

Fig. 4-10. DLTS and LDLTS spectra of hydrogenated silicon containing gold. The conventional DLTS spectrum is shown as an insert at the top of the figure. The broad peak centered at 260 K is attributed to electron emission from the gold acceptor G4. The main spectra were obtained by the Laplace technique and clearly separate the gold-acceptor level and the gold-hydrogen level G4 (redrawn from ref. 26).

The parallel use of three different numerical routines increases the confidence level in the spectra obtained. The evolution of LDLTS in past few years has enabled the theoretical limit of DLTS to be achieved. For relatively shallow states that emit at low temperature, the reduction in line width is remarkable and an increase in resolution of at least two orders of magnitudes is readily achievable but its sensitivity is about an order of magnitude less than that of DLTS. For example, if a sample with a trap concentration approximately 1% of the shallow dopant concentration and quiescent capacitance of about 10 pF is studied by LDLTS then the signal-to-noise ratio (SNR) of 1000 is readily achievable. This is necessary to separate defects with similar emission rates with time constant of 2 i.e. $(e_1/e_2) \approx 2$. An illustration showing a comparison of LDLTS (full figure) and DLTS (inset) spectra obtained from the same (Si:Au,H) sample is depicted in Fig. 4-10 [26]. DLTS shows a broad featureless spectrum of DLTS whilst the LDLTS resolves the broad DLTS spectrum into two peaks.

Finally, to completely characterize defect levels in the semiconductor by DLTS and LDLTS, both the majority and minority carrier traps should be identified. If the depletion layer is formed from a p-n junction then both majority and minority carriers can easily be injected into the depletion region by applying a correct filling pulse. However, when a Schottky diode is used to form the depletion region, a forward bias filling pulse will not always inject minority carriers into the depletion region, therefore minority carrier traps may not be observed. This is true for Si, but not entirely true for all semiconductors e.g. Ge. For Ge, metal-semiconductor Schottky barrier diodes with large barrier heights (in relation to the band gap) can be formed. It has been shown that for a high barrier height, an inversion layer with high concentration of minority carriers can be formed near the semiconductor surface [27,28]. When a forward filling bias is applied to such a diode it results in a flux of holes from the inversion layer to the semiconductor bulk. Thus the minority carrier traps can be filled, making them visible to the DLTS and LDLTS techniques. The minority carrier trap study using Schottky barrier diodes on Si is achievable if traps are filled by optical means. Throughout this work, the Schottky barrier diodes (SBDs) have been used because they are easy to fabricate, easy to use and quality diodes are possible.

4.5 Electric Field Effect

The DLTS and LDLTS techniques employed for defect characterization probe defects in the reverse-biased depletion region. Therefore the emission process takes place in the presence of a high electric field. For an n-type semiconductor, the magnitude of the electric field in the depletion region is given by

$$|E| = \sqrt{\frac{2qN_D}{}(V_{bi} - V_a)} - \frac{qN_D x}{} \qquad (4.21)$$

where q is the electronic charge, N_D is the shallow dopant concentration, V_{bi} the built-in-potential, V_a is the applied bias voltage and ε the permittivity of the semiconductor.

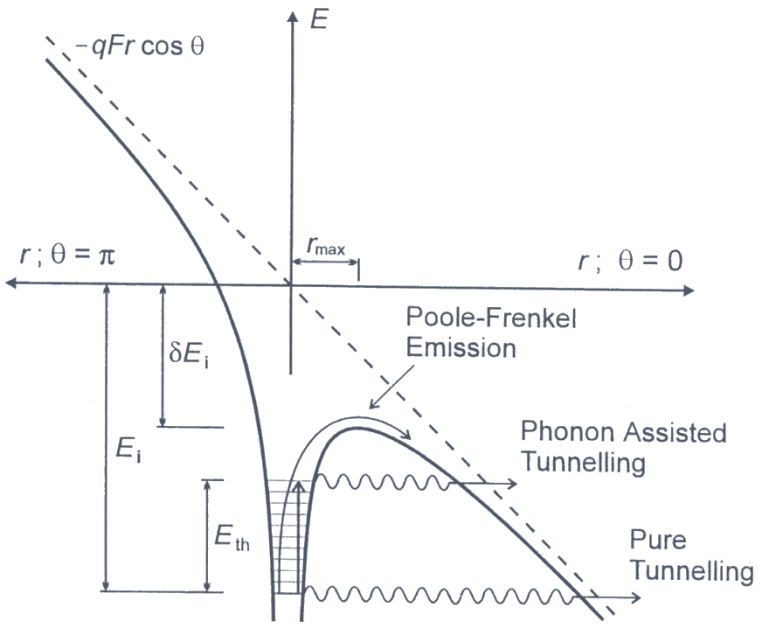

Fig.4-11. The Coulombic well and the three mechanisms of field enhanced emission; Poole-Frenkel emission, phonon assisted tunneling and pure tunneling where E_{th} is the position of the virtual level above the deep level, E_i is the ionization energy of the deep level and δE_i is the change in the ionization energy due to the electric field, redrawn from ref. 30.

The electric field in the depletion region can reach average values of 10^5-10^7 V/m, depending on the doping density and the bias voltage. Such high electric fields can influence the shape of defect potentials and may, therefore, enhance carrier emission

rates from potential wells, by the Poole-Frenkel effect [29,30,31] or phonon-assisted tunneling [6,32]. A potential well may be considered as a trap with significant spatial extent and can be described by different models, e.g. a Coulombic, square or Gaussian potential well. For a Coulombic potential well, the mechanisms of field-enhanced emission are depicted in Fig. 4-11. The Poole-Frenkel effect is a mechanism in which a carrier is thermally emitted over the top of the barrier, which has been lowered by the application of an electric field. The emission rate in the presence of the electric field F is now given by

$$e(F) = e(0)\exp\left(\frac{q^3}{kT}F^{1/2}\right) \tag{4.22}$$

where $e(0)$ is the zero field emission rate, q is the electron charge, T is the temperature in Kelvin and ε is the permittivity of the semiconductor. If a plot of $\log[e(F)]$ vs. $F^{1/2}$ is a linear plot, then it is experimental evidence of a charge leaving a trap of opposite sign. This implies a donor type defect in n-type material and acceptor type trap in p-type material. The Poole-Frenkel mechanism is dominant if the potential well has some appreciable spatial extent. The other mechanisms shown in Fig. 4-10 are phonon-assisted tunneling and pure tunneling. In the phonon-assisted tunneling process, a charge carrier absorbs thermal energy and is excited to a virtual state at E_{th} above the deep level. The electron will then be able to tunnel through the barrier from this virtual level to the conduction band. For any of the field-enhanced emission mechanisms, the electric field is spatially varying and so emission occurring from different positions in the depletion will be affected to a different extent, giving rise to non-exponential capacitance transients.

References

[1] D. V. Lang, *J. Appl. Phys*. **45** (1974) 3023.

[2] D. V. Lang, *J. Appl. Phys*. **45** (1974) 3014.

[3] L. Dobaczewski, P. Kaczor, I.D. Hawkins and A.R. Peaker, *J. Appl. Phys*. **76** (1994) 194.

[4] L. Dobaczewski, A.R. Peaker and K.B. Nielsen, *J. Appl. Phys*. **96** (2004) 4689.

[5] P. Blood and J.W. Orton, *Rep. Prog. Phys*. **41** (1978) 11.

[6] F.D. Auret and P.N.K. Deenapanray, *Crit. Rev. Sol. Stat Mater. Sci*. **29** (2004) 1.

[7] W. Shockley and W.R. Read, JR, *Physical Rev*. **87** (1952) 835.

[8] R.N. Hall, *Phys. Rev*. **83** (1951) 228.

[9] G.L. Miller, D.V. Lang and L.C. Kimerling, *Ann. Rev. Mater. Sci*. **7** (1977) 377.

[10] C.H. Henry and D.V. *Lang, Phys Rev. B* **15** (1977) 989.

[11] V.P. Markevich, I.D. Hawkins, A.R. Peaker, K.V. Emtsev, V.V. Litvinov, L.I. Murin and L. Dobaczewski, *Phys. Rev. B* **70** (2004) 235213.

[12] L.C. Kimerling, *J. Appl. Phys*. **45** (1974) 1839.

[13] F.D. Auret, *Rev. Sci. Instrum*. **57** (1986) 1597.

[14] Y. Zohta and M.O. Watanabe, *J. Appl. Phys*. **53 No.3** (1982) 1809.

[15] D.V. Lang, In "Thermally Stimulated Relaxation of Solids" (P. Braunlich, ed.) pp93-133, Springer-Verlag, Berlin, 1979.

[16] A.A. Istratov,.*J. Appl. Phys. **82*** (1997) 2965.

[17] J.A. Borsuck and R.M. Swanson, IEEE Trans. Electron Devices **27** (1980) 2217.

[18] C.R. Crowell and S. Aliphani, *Solid State Electron* **24** (1981) 25.

[19] K. Ikossi-Anastasiou and K.P. Roenker, *J. Appl. Phys*. **61** (1987) 182.

[20] D.D. Nolte and E.E. Haller, *J. Appl. Phys*. **62** (1987) 900.

[21] C. Eiche, D. Maier, M. Schneider, D. Sinerius, J. Weese, K.W. Benz, and Honerkamp, *J. Phys. Condens. Matter*. **4** (1992) 6131.

[22] G.A. Korn and T.M. Korn, in mathematical handbook , (McGraw-Hill, New York) (1968).

[23] S.W..Provencher, *Comput. Phys. Commun*. **27** (1982) 213.

[24] J. Weese, *Comput. Phys. Commun*. **69** (1991) 99; ibid. **77** (1993) 429.

[25] A. Matulis, Z. Kancleris, Semiconductors Physics Institute, Vilnius, Lithuania.

[26] P. Deixler, J. Terry, I.D. Hawkins, J.H. Evans-Freeman, A.R. Peaker, L. Rubaldo, D.K. Maude, J.C. Portal, L. Dobaczewski, K.Bonde Nielsen, A. Nylandsted Larsen, and A. Mesli, *Appl. Phys. Lett.* **73** (1998) 3126.

[27] V.P. Markevich, A.R. Peaker, V.V. Litvinov, V.V. Emstev, L.I. Murin, *J. Appl. Phys*. **95** (2004) 4078.

[28] E.H. Rhoderick, *Metal-Semiconductor Contacts* (Clarendon Press, Oxford, 1978).

[29] J. Frenkel, *Phys. Rev.* **54** (1938) 647.

[30] S.D. Ganichev, E. Ziemann, W. Pretll, I.N. Yassievich, A.A. Istratov, E.R Weber, *Phys. Rev. **B*** **61** (2000) 10361.

[31] N. Zangenberg, J. Goubet, A.N. Larsen, *Nuclear Instruments and Methods in Physics Research **B*** **186** (2002) 71.

[32] S. Makram-Ebeid and M. Lannoo, *Phys. Rev. **B*** **25** (1982) 6406.

Chapter 5

Experimental Techniques

5.1 Introduction

The experimental techniques that are used for sample preparation, metallization, particle irradiation and defect characterization are described in this chapter. The sample preparation, (i.e. cleaning processes, Schottky and ohmic contacts fabrication) is presented in section 5.2. Section 5.3 deals with the irradiation of samples by high energy electrons or low energy noble gas ions. The Schottky contacts and the defects characterization tools, i.e. current-voltage (*I-V*), capacitance-voltage (*C-V*) current-temperature (*I-T*), capacitance-temperature (*C-T*), deep level transient spectroscopy (DLTS) and Laplace-DLTS (LDLTS) are outlined in section 5.4. The annealing studies set-up, which enables defect annealing analysis is presented in section 5.5.

5.2 Sample Preparations

Before metallization, samples were cut into 1 cm x 0.3 cm for silicon and 0.5 cm x 0.3 cm for germanium followed by a chemical cleaning process. It is important to note that immediately after the cleaning process, metallization should follow to reduce oxide layer build-up and recontamination of the sample.

5.2.1 Silicon Cleaning Process

The cleaning steps are used sequentially, as follows;

(1) Degreasing; removing of dust particles, or grease in boiling trichloroethylene (TCE) and then boiling isopropanol for 3 minutes, followed by rinsing in de-ionized water.

(2) Organic cleaning; removal of insoluble organic contaminants and metals using a H_2O : 30% H_2O_2 : 25% NH_4OH (5:1:1) solution at (75 – 80ºC) for 10 minutes followed by rinsing in de-ionized water.

(3) Oxide stripping; removal of the self-passivating oxide film is done in two steps. (a) etching in 40% HF : 70% HNO_3 : 96% glacial CH_3COOH (2:15:5) solution for 3 s and the outstanding oxide layer is stripped by (b) dipping in dilute 40% HF : H_2O (1:10) solution for 5 s followed by a rinse in de-ionized water. This, however, still leaves some amount of silicon oxide on the surface in addition to other species such as hydrogen, fluorine and hydroxyl groups [1].

(4) The samples are blow-dried in stream of N_2 gas and ready for the metallization step.

5.2.2 Germanium Cleaning Process

The germanium cleaning steps are in sequence, as follows;

(1) Degreasing in trichloroethylene (TCE), acetone and then methanol, each for 5 minutes in an ultrasonic bath at room temperature. This degreasing step is followed by rinsing in de-ionized water.

(2) Organic cleaning; removal of insoluble organic contaminants and metals in a solution of 30% H_2O_2 : H_2O (1:5) for 1 minute and then rinsing in de-ionized water.

(3) The samples are blow-dried in stream of N_2 gas and ready for the metallization step.

5.2.3 Ohmic and Schottky Contact Fabrication

Immediately after the chemical cleaning procedure, ohmic and Schottky contacts were fabricated. To form ohmic contacts on Ge, a 100 nm thick layer of Au-Sb (6% Sb) was deposited on the back surface of the sample by resistive deposition after evacuating the chamber to pressure levels of approximately 10^{-6} Torr. The ohmic contact was thereafter annealed at 350ºC for 10 minutes in Ar gas. This subsequent annealing step helps to optimize the ohmic contact by lowering the barrier height, hence reducing its resistivity [2]. The annealing temperature is chosen such that it optimize the ohmic contact [3]. The use of a reducing atmosphere avoids any further oxidation of the metal during annealing, while it can also reduce any interfacial oxide between the metal and semiconductor.

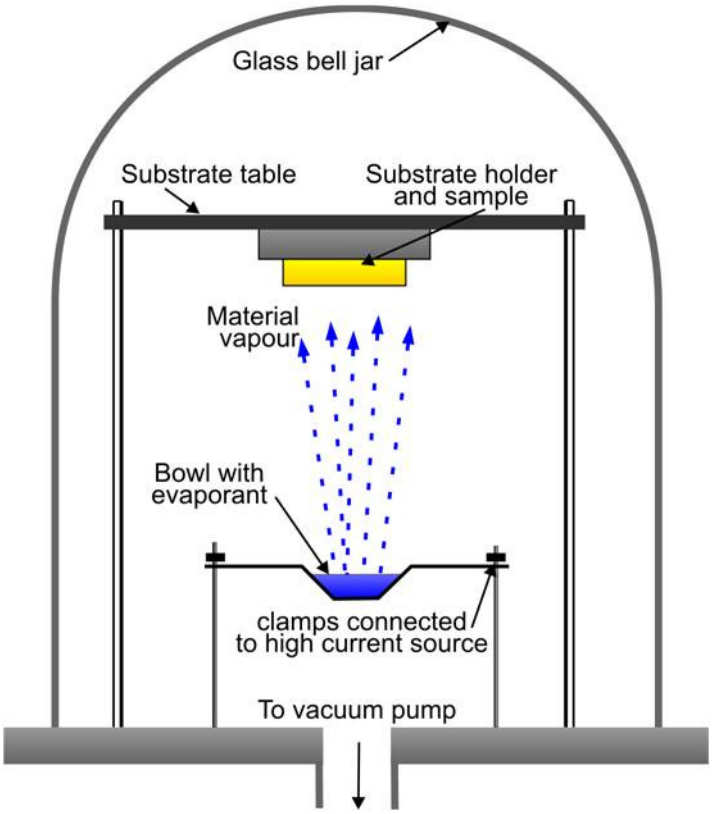

Fig. 5-1. The resistive deposition system.

The resistive deposition system is depicted in Fig. 5-1. In this technique, a current flows through the crucible containing the metal to be deposited until it reaches the melting point of the metal. The metal evaporates and deposits onto the sample above the crucible. The deposition rate is controlled by adjusting the current until the required evaporation rate has been achieved. The resistive deposition method is used for metals with low melting point (<1600^{o}C) e.g. Al, Au, Pd or Ni and the technique cannot be used to deposit higher melting point metals.

The Schottky contacts, 100 nm thick layer, were fabricated on both Si and Ge by evaporating the metals e.g. palladium (Pd) or gold (Au) on the polished side, through masks with circular holes 0.60 mm in diameter. The contacts were fabricated using resistive deposition or electron beam deposition. A typical electron beam system (EBD) is shown in Fig. 5-2. In this technique, a hot filament emits electrons which are then accelerated and focused onto the target (crucible containing the metal) by electric and magnetic fields. This results in the melting and evaporation of the metal which deposites onto the sample.

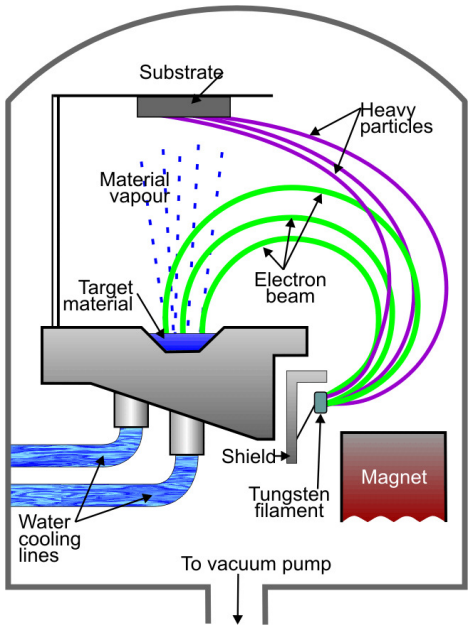

Fig. 5-2. The electron beam deposition (EBD) system.

The deposition rate is controlled by controlling the filament current. The EBD method can deposit any metal but its disadvantage is that it may introduce defects on and below the surface of the sample on which contacts are fabricated. After the sample metalization, as shown by an illustration in Fig. 5-3, the sample is ready for further processing, i.e. bombardment by energetic particles, and electrical characterization of the resulting defect levels.

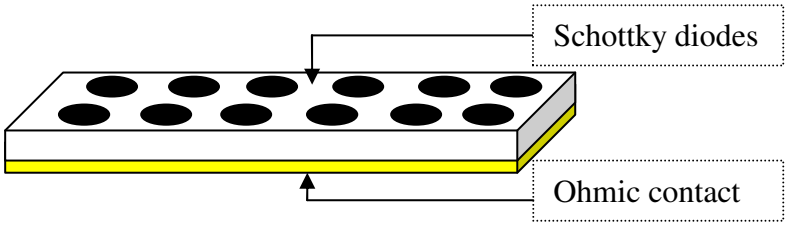

Fig. 5-3. A typical sample showing circular Schottky diodes on the top surface and ohmic layer on the back surface (the thickness of the ohmic layer has been enlarged for clarity).

5.3 Sample Irradiation

After metallization process, lattice defects were introduced by bombarding the samples from the Schottky side with high energy (MeV range) electrons, or noble gas ions (keV range) of well controlled fluencies as shown in Fig. 5-4.

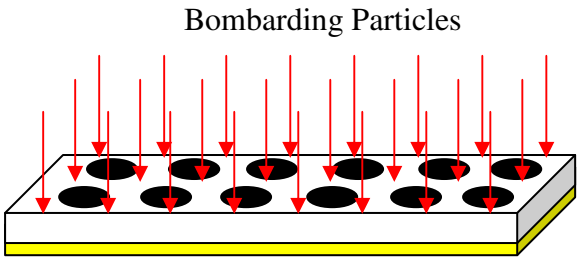

Fig. 5-4. Schematic diagram of a typical sample under irradiating particles.

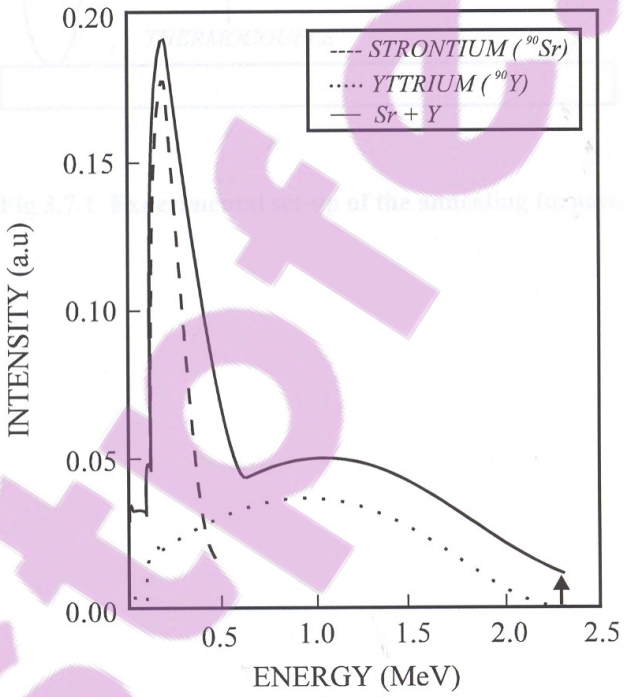

Fig. 5-5. Energy distribution of electrons emitted by a ^{90}Sr radionuclide. For clarity the sum of the Sr and Y contributions has been displaced by an amount indicated by the arrow, (redrawn from ref. 4).

Depending on the incident particle type, size and energy, some particles can go right through the sample and others may lose all their energy due to collision and eventually stop within the sample. All the irradiation processes were performed at room temperature.

5.3.1 Electron Irradiation

The electron irradiation of the samples was carried out using (1) a particle accelerator at Ohio State University in USA, for Si samples and (2) a strontium-90 (^{90}Sr) radionuclide source for Ge samples. The strontium source used is disc-shaped, with a diameter of 8.4 mm and an activity of 20 mCi. The ^{90}Sr radionuclide (half-life of 28.5 years) decays first to yttrium (Y) (half-life of 64.1 hours), with the emission of a 0.5 MeV electron. The Y in turn decays by the emission of a 2.27 MeV electron to zirconium (Zr). The electrons emitted from this radioactivity of ^{90}Sr have a continuous energy distribution as shown in Fig. 5-5. It is clear from this figure that, approximately 70% of the total number of emitted electrons, have energies above 250 keV, i.e. the threshold for producing defects by elastic collisions [4]. During the irradiation the samples were placed 1 mm below the center of the radioactive disc so that one can assume that the flux reaching the sample at this position is that which leaves the surface of the source. The total fluence rate of electrons emitted is calculated from the activity of the ^{90}Sr source. Each ^{90}Sr decay results in the emission of two electrons because the half-life of Y is much shorter than that of Sr. This total dose is equal to the area below the curve (Sr + Y) in Fig. 5-5. It is assumed that temperature of the sample remains constant during the irradiation process.

5.3.2 Low Energy Noble Gas Irradiation

The low energy (keV) noble gas ions irradiations were performed in the Auger electron spectroscopy system (AES). A collimated beam of Ar ions of energy 3 keV and fluencies in the range 10^{13} – 10^{14} ions/cm^2 was used for the sputtering process. The beam was incident on the sample at an angle of about 35^o to the normal.

5.4 Electrical Characterization

After metallization, current-voltage (*I*-*V*) and capacitance-voltage (*C*-*V*) measurements were used to monitor the quality and electrical properties of the diodes while deep level transient spectroscopy (DLTS) [5] and Laplace-DLTS (LDLTS) [6,7] were used to characterize defects in the semiconductor band gap before and after particle irradiation.

5.4.1 Current-Voltage and Capacitance-Voltage Measurement System

The diode properties which were extracted from (*I-V*) and (*C-V)* measurements are; series resistance R_s, free carrier density profiles N_D, barrier height ϕ_B, ideality factor n, and leakage currents I_r (measured at reverse bias of -1 V). These diode properties determine whether a diode is usable for DLTS measurements. A good diode for DLTS application is one that gives high signal-noise ratio, and these are diodes with high barrier height, low leakage current (<10^{-4} A) and low series resistance (<200 Ω). The diode electrical properties were monitored after each DLTS scan (since it is well known that diodes tend to degrade after several up-down temperature scans in DLTS system) and to monitor the carrier reduction after irradiation, or diode processing. The schematic diagram for the measurements is illustrated in Fig. 5-6 [8].

The (*I-V*) characteristics were measured using an HP 4140B pA meter/ DC voltage source with a lower current limit of 10^{-14} A and (*C-V*) measurements were done by an HP 4192A LF Impedance Analyzer. Samples were mounted in a metal box enclosure to eliminate light and electrical noise.

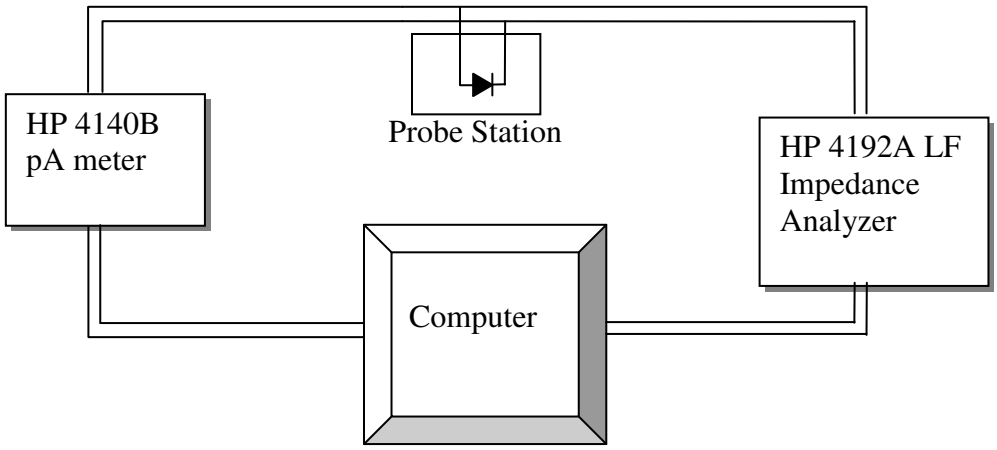

Fig. 5-6. Block diagram of (I-V) and (C-V) measurements station.

5.4.2 Deep Level Transient Spectroscopy (DLTS) and Laplace-DLTS Systems

The DLTS and L-DLTS system used for this study consists of the following units,

(a) A cryostat in which the sample is mounted. The temperature is controlled by a Lake Shore 340 temperature controller in the range (16 K – 380 K).

(b) A fast (1 MHz range) Boonton 7200 capacitance meter with 100 mV, 1 MHz ac voltage, which monitors thermal emission after excitation by a pulse generator.

(c) A Laplace card and software [7]. This card has an internal pulse generator for generating the desired quiescent bias voltage and pulses, and it is also the data collection and processing system which analyses and averages transients before displaying the spectra for both the conventional DLTS and LDLTS.

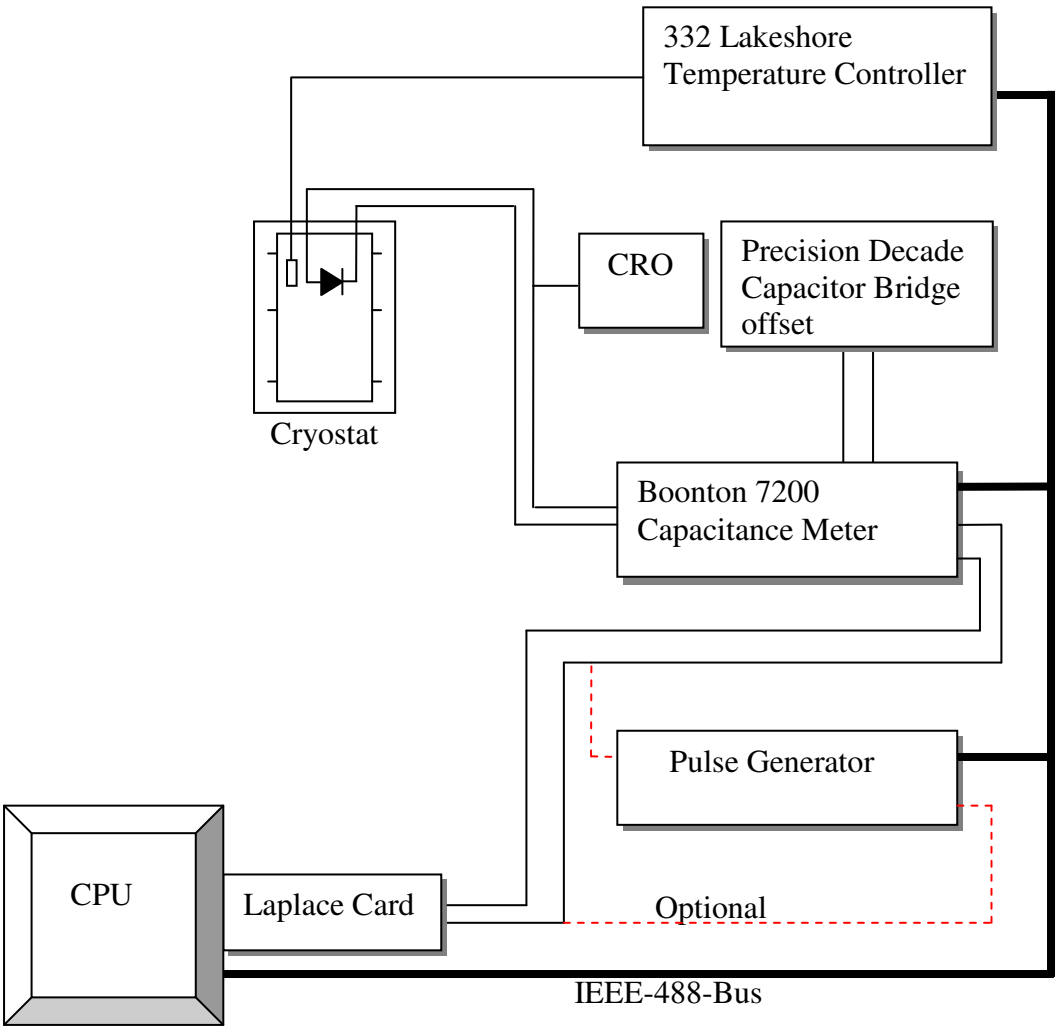

Fig. 5-7. The Schematic of the DLTS and LDLTS system used in this study.

(d) An external pulse generator (hp 33120A 15 MHz Function waveform generator), to provide the desired quiescent bias voltages and filling pulse to the diode which are not provided by the Laplace card.

The Schematic diagram of the DLTS and LDLTS used in this study is depicted in Fig. 5-7. The Laplace program sets the sample excitation parameters, the capacitance transient acquisition conditions, initiates the measurement, acquires the transient and

finally converts it into a conventional-DLTS or Laplace spectrum. In case of conventional DLTS the capacitance meter measures the capacitance transients after excitation. The transients are then processed by the Laplace card and as the temperature is ramped a DLTS spectrum is displayed on a computer for a particular '*rate window*' which can be set in the range 1 s^{-1} – 5000 s^{-1}. Similarly for the LDLTS the capacitance meter monitors the capacitance transients after excitation and the Laplace card then averages the transient and implements the inverse Laplace transforms to calculate the emission rates and magnitude of the signal using three different software routines CONTIN, FTIKREG and FLOG [7] before the computer displays the Laplace spectrum. The internal pulse generator (provided by the Laplace card) has been used when very good diodes were measured and the external pulse generator was connected in case of poor diodes since it has been established that very high signal: noise ratio (SNR) >1000:1, which is necessary to separate levels with close emission rates, could only be achieved with an external pulse generator but not with the internal pulse generator. When the external pulse generator is used a pulse from the Laplace card is used to trigger the pulse generator.

The Laplace card has also been used for the current-temperature (*I-T*) and capacitance-temperature (*C-T*) measurements by connecting the HP 4140B pA current meter and HP 4192A LF Impedance analyzer respectively and the measurements were automated by Labview routine.

5.5 Annealing Apparatus

The annealing studies were performed in a Lindberg "Hevi-duty" furnace with a maximum temperature of 1200ºC. The inert atmosphere was achieved by connecting the furnace to a supply of inert gas such as argon or nitrogen. The temperature was monitored using a thermo-couple with a digital display which was placed just under the sample holder.

References

[1] S. Wolf and R. Tauber; "*Silicon Processing; Vol.1*" Lattice Press, CA, (1986)

[2] F.D. Auret, W.E. Meyer, S. Coelho and M. Hayes, *App. Phys. Let*. **88**, (2006) 242110.

[3] H. Jian-guo and W. Zi-gin, *Physical Review B* **40** (1989) 1008.

[4] F.D. Auret, S.A. Goodman, G. Myburg and W.E. Meyer, *Appl. Phys. A* **56** (1993) 547.

[5] D.V. Lang, *J. Appl. Phys*. **45** (1974) 3023.

[6] L. Dobaczewski, P. Kaczor, I.D. Hawkins and A.R. Peaker, *J. Appl. Phys.* **76** (1994) 194.

[7] L. Dobaczewski, A.R. Peaker and K.B. Nielsen, *J. Appl. Phys.* **96** (2004) 4689.

[8] S.A. Goodman Ph.D Thesis, University of Pretoria (2004).

Chapter 6: Results

Radiation-induced defects in Ga-or B-doped silicon by 1 MeV electron irradiation

6.1 Introduction

Silicon (Si) integrated circuits are still currently dominating the technological advancement of semiconductor devices because of the several advantages of silicon over other semiconductors (such as, stable oxide, cheapest in its field of application, and better understood etc). The understanding of lattice defects in semiconductors is an important step in the device fabrication since defects can be detrimental to some devices (e.g. solar cells were they can act as minority carrier 'killers' thereby reducing the efficiency of the solar cells [1]) or beneficial to some (e.g. when they act as recombination centers in fast switching devices, hence enhancing the switching speeds [2]). Defects can be introduced into a semiconductor in a number of ways, (a) growth of semiconductor, (b) processing of device (e.g. plasma etching) or high-energy particle - irradiation and (c) under operating conditions. A notable example in the latter case is the degradation of B-doped Cz –Si solar cells under either illumination or carrier injection due to formation of a metastable defect involving B and O [2]. The lifetime degradation is not observed in Ga-doped Cz Si [2]. Silicon is a very useful material in the photovoltaic industry because of its relative high carrier lifetime ~1 ms, (hence larger diffusion lengths of ~1 mm) when compared to most semiconductors. Apart from germanium, silicon has a relatively low effective mass for holes and therefore p-type silicon is attractive for producing high frequency devices and solar cells.

Very little work has been done on Ga-related defects on p-type silicon [3-4]. The defects characterized by DLTS [5] and high-resolution Laplace-DLTS (LDLTS) [6-7] are presented in this chapter and the resolution of LDLTS is demonstrated.

6.2 Experimental Procedure

Boron and gallium-doped silicon with a carrier density of 1.5 x 10^{16} cm^{-3} and 3.5 x 10^{16} cm^{-3} respectively have been used. The samples were prepared for metal deposition by chemical cleaning (i.e. degreasing then dipping in dilute 10% HF solution). After blow-drying in N_2 gas, the samples were immediately loaded into the vacuum chamber, which was evacuated to a pressure of below 1 x 10^{-6} mbar to reduce oxidation before processing. Through a circular mask, of diameter 0.48 mm, Ti and then Al, 100 nm thick each, were deposited using electron beam deposition (EBD). After diode fabrication, the samples were then irradiated (at room temperature) with 1 MeV electrons to fluences of 1.5 x 10^{16} cm^{-2} (B-doped) and 3.5 x 10^{16} cm^{-2} (Ga-doped), respectively. Before the irradiation process the samples were annealed at 550°C to remove all the EBD induced defects. Prior to electrical characterization, {i.e. current-voltage (*I-V*), capacitance-voltage (*C-V*), DLTS and Laplace (LDLTS)} ohmic contacts were formed on the rear side of the sample using In-Ga eutectic. The defect 'signatures' {i.e activation enthalpy E_T (in eV), and apparent capture cross-section, σ_a (in cm^2)} were determined from Arrhenius plots of $ln(T^2/e_h)$ vs. $1000/T$, where e_h is the hole emission rate and T is the measurement temperature.

To study defect annealing characteristics of primary and secondary radiation induced defects isochronal annealing was performed on the Schottky contacts in the temperature range 30°C - 350°C in steps of 50°C for 20 minutes in Ar gas. Each annealing cycle was followed by electrical characterization of the defects.

6.3 Results

In this section the electronic and annealing properties of hole traps created in the samples by electron irradiation or proton irradiation are discussed. First, it is enlightening to look at the defect resolution capability of Laplace-DLTS over conventional DLTS.

6.3.1 Conventional DLTS versus Laplace-DLTS

The DLTS spectrum recorded from the Ga doped Cz Si sample after the electron irradiation is shown in Fig. 6-1. The spectra exhibit two dominant peaks positioned at around 115 K and 190 K with a shoulder peak at high temperature side of low temperature peak. On the other hand, the insets show the spectral density functions (SDF), i.e. LDLTS spectra (measured around the peak positions of the two broad peaks). LDLTS is clearly able to resolve the broad DLTS peaks into two groups of discrete levels as depicted in inset (a) and inset (b). Notably, the broad peak around 115 K is resolved into three discrete defects with levels at E_V + 0.18 eV, E_V + 0.19 eV, and E_V + 0.23 eV while the peak around 190 K is resolved into two discrete defects with levels at E_V + 0.33 eV and E_V + 0.34 eV. The levels E_V + 0.19 eV and E_V + 0.34 eV are the dominant peaks as evidenced by the height of the LDLTS signal.

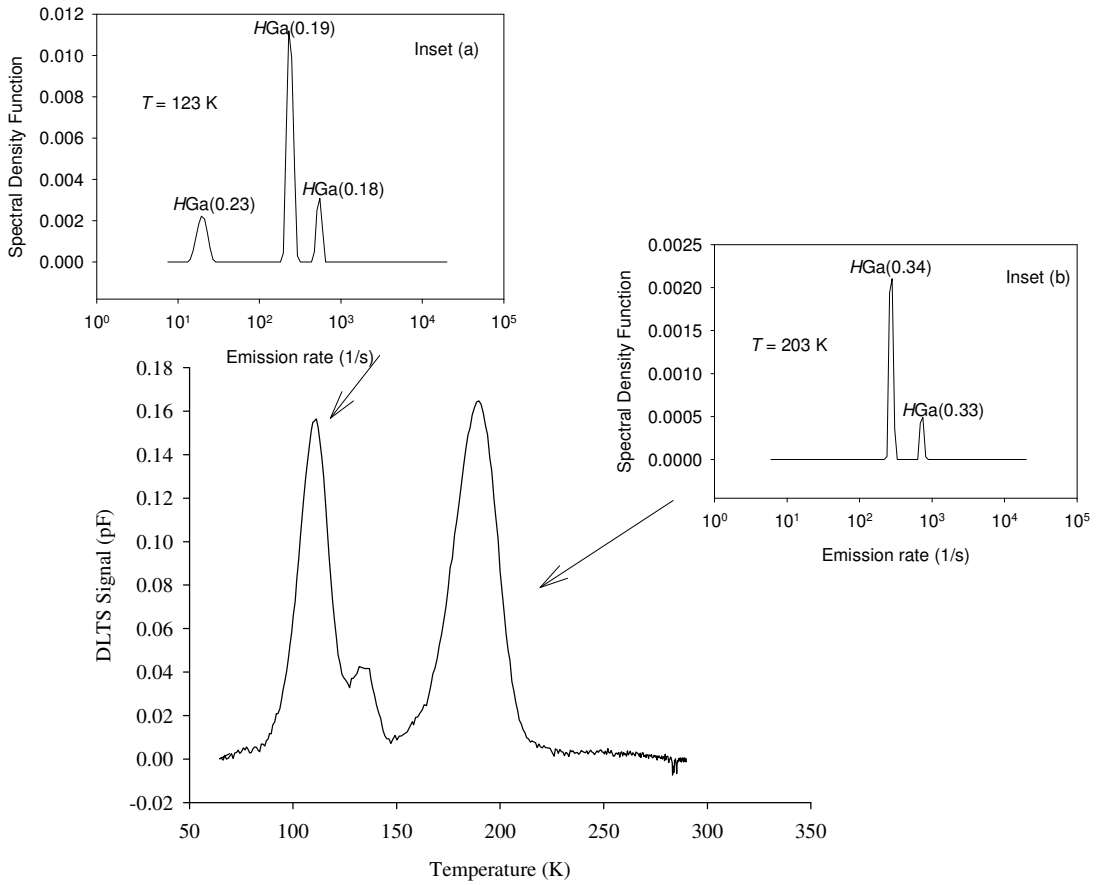

Fig. 6-1. Conventional DLTS spectra of electron irradiated Ga-doped Cz Si. Inset: The LDLTS spectra for each broad DLTS peak. The spectra were recorded at a reverse bias V_r = -2V, pulse voltage V_p = 0.5 V, pulse width of 1 ms and rate window (RW) of 80 s^{-1}.

6.3.2 Electron irradiation-induced defects in Ga –doped Czochralski grown Si

The DLTS spectra of primary and secondary defects introduced after electron irradiation of Ga-doped Czochralski (Cz) Si are shown in Fig. 6-2. The samples were defect free before the irradiation. The defects signatures (extracted from the Arrhenius plots, Fig. 6-4) and their annealing properties are summarized in Table 6.1 and Fig. 6-3. The defect levels, *H*Ga(0.18), *H*Ga(0.19), *H*Ga(0.23), *H*Ga(0.33) and *H*Ga(0.34) were observed after the irradiation as shown by DLTS spectra in Fig. 6-2 (a). In this nomenclature '*H*' is the hole trap, 'Ga' is the dopant and '0.19' is the activation enthalpy, i.e. (E_V + 0.19) eV. The origin of both *H*Ga(0.18) and *H*Ga(0.33) is not clear at the moment, but *H*Ga(0.34) has been assigned to the C_I-O_I complex [3,8,9].

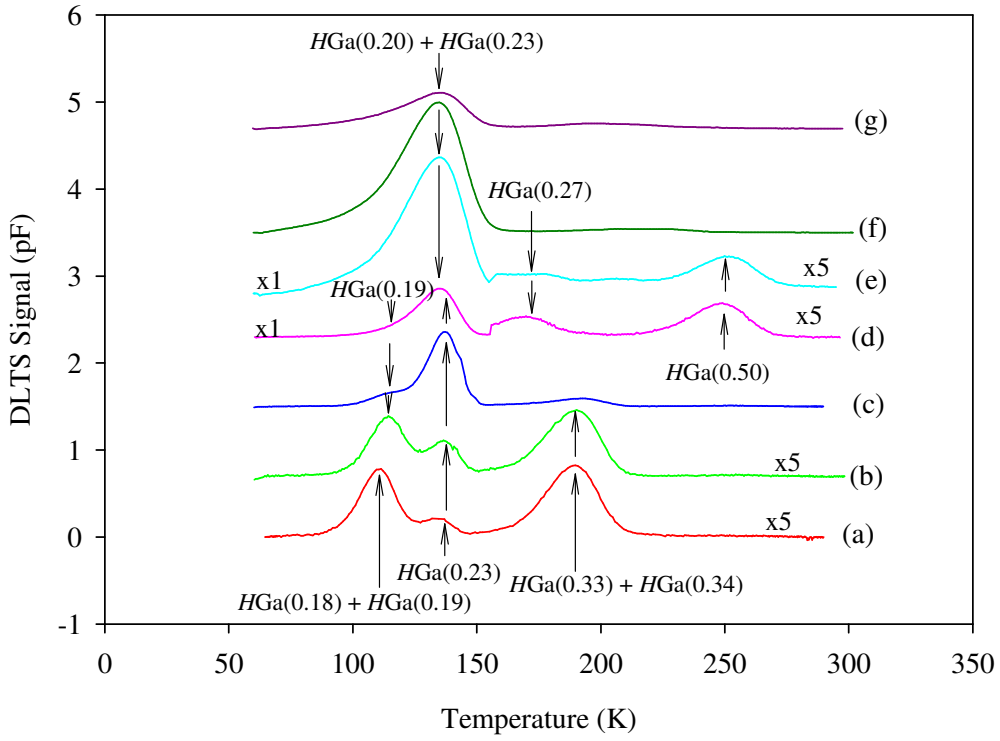

Fig. 6-2. DLTS spectra showing defects introduced in 1 MeV electron irradiated Ga – doped Cz Si for as (a) as-irradiated and after annealing for 20 minutes at (b) 100˚C, (c) 150˚C, (d) 175˚C, (e) 200˚C, (f) 300˚C and (g) 350˚C. These measurements were recorded at a quiescent reverse bias V_r = -2V, a filling pulse V_p = +0.5 V, pulse width of 1 ms and a rate window of 80 s^{-1}.

There has been some inconsistency in the literature about the identity of the divacancy in p-type Si, but *H*Ga(0.19) is identified as the (+/0) charge state of the divacancy

[3,10] because of its annealing behavior. *H*Ga(0.23) is suggested to be H related defect with the source of hydrogen being the wet etching processing step and it shows strong reverse annealing (i.e. increase in defect concentration with annealing temperature) around 150˚C, an indication that H could be coming from some passivated defect levels [11].

The introduction rates deduced from depth profile measurements for the dominant traps *H*Ga(0.34) and *H*Ga(0.19) are 2.5 x 10^{-2} cm^{-1} and 4.0 x 10^{-3} cm^{-1} respectively which is consistent with the results in the literature [12].

Table 6.1. Electronic properties of defects introduced in Ga-doped Cz Si.

Defect	E_T (eV)	σ_a (cm^2)	T_{peak} [a] (K)	T_{in} [b] (˚C)	T_{out} [c] (˚C)	Defect identity
After	*Irradiation*					
*H*Ga(0.18)	E_V + 0.18	1.4 x 10^{-15}	115	RT	100	? ref. 4
*H*Ga(0.19)	E_V + 0.19	5.1 x 10^{-16}	115	RT	225	$V_2^{+/0}$ [3,4,10,11, 12]
*H*Ga(0.23)	E_V + 0.23	2.6 x 10^{-16}	137	RT	---	H-related? [11]
*H*Ga(0.33)	E_V + 0.33	1.6 x 10^{-15}	190	RT	100	?
*H*Ga(0.34)	E_V + 0.34	8.0 x 10^{-16}	190	RT	175	C_I-O_I [3,8,9,11,12]
After	*Annealing*					
*H*Ga(0.20)	E_V + 0.20	3.2 x 10^{-16}	160	175	----	?
*H*Ga(0.27)	E_V + 0.27	2.9 x 10^{-16}	160	175	300	Ga-related?
*H*Ga(0.50)	E_V + 0.50	5.2 x 10^{-15}	250	175	300	Ga or H-related?

[a]Peak temperature at a rate window of 80 s^{-1}, [b]Temperature at which the defect is introduced. [c]Temperature at which the defect is removed.

The C_I-O_I complex is thought to be a recombination center which is responsible for the minority-carrier lifetime reduction and carrier removal in Si, thus has a dominant role to control the efficiency of Si solar cells [3].

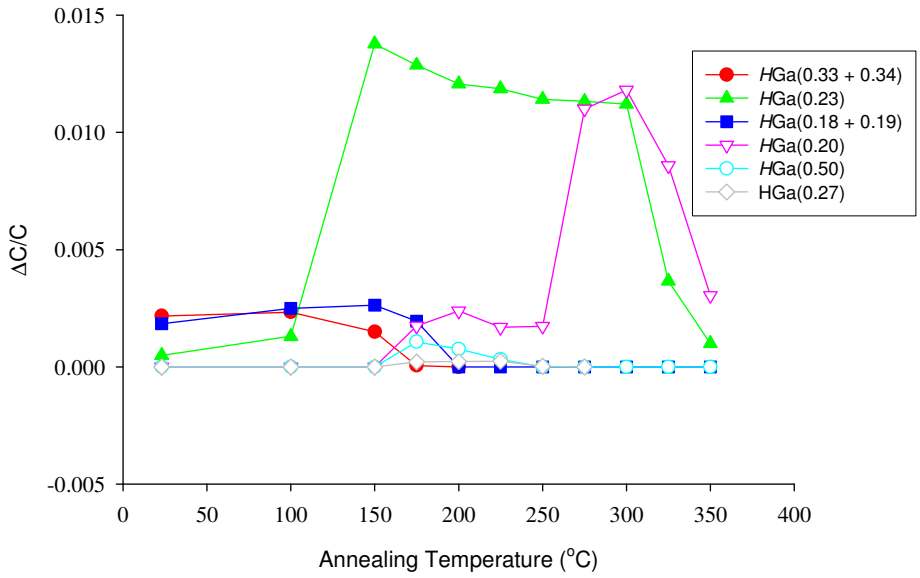

Fig. 6-3. Isochronal annealing behavior of defects in electron-irradiated B-doped epitaxial Si.

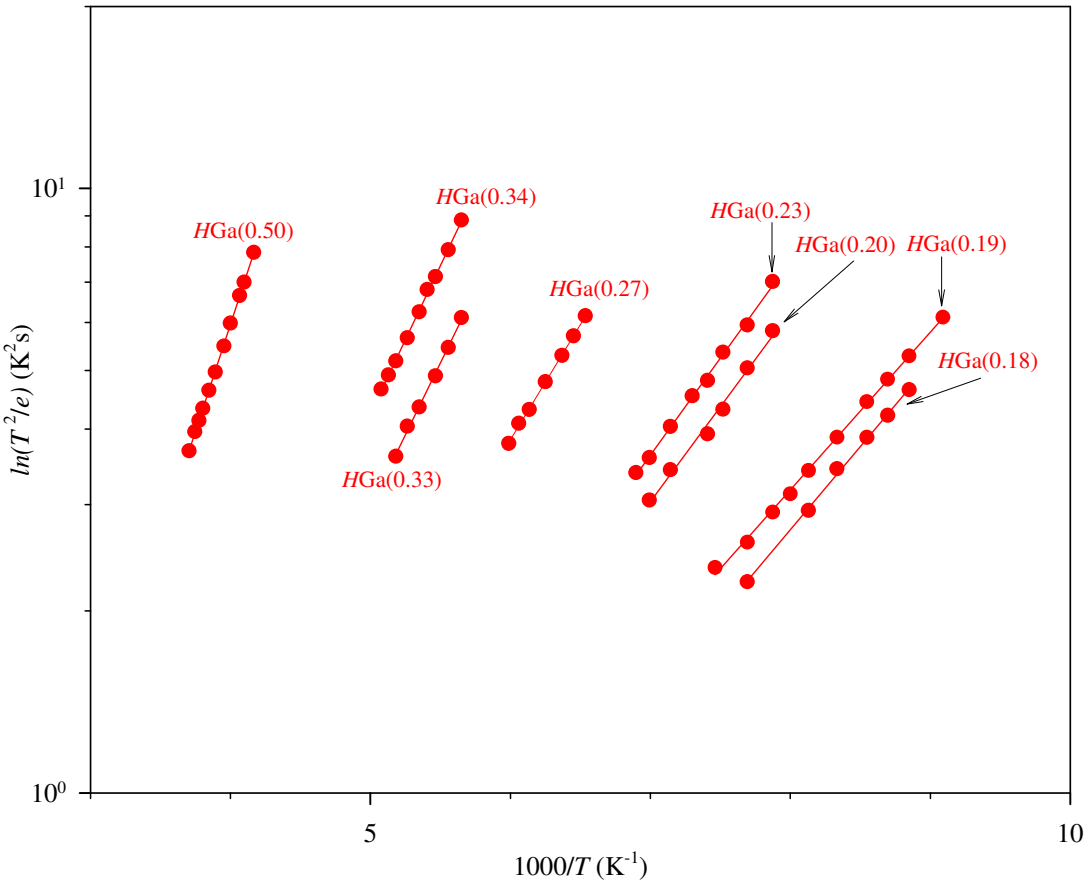

Fig. 6-4. Arrhenius plots of the defects introduced in Ga-doped Cz Si by 1 MeV electron irradiation.

From a practical perspective, the complete characterization of defects requires that the annealing kinetics of the defect is established. Annealing experiments serve to determine, amongst others, (i) the temperature range within which a defect can be removed after its initial introduction, (ii) whether secondary defects that may be detrimental to device performance are introduced during high-temperature steps in the processing of devices, and (iii) the structure of defects through comparative studies. Figures 6-2 and 6-3 show the annealing behavior of defects in electron-irradiated Ga doped Cz Si. The secondary hole traps *H*Ga(0.20), *H*Ga(0.27) and *H*Ga(0.50) are all introduced after annealing at 175˚C, Fig. 6-2 curve (d), and *H*Ga(0.27) and *H*Ga(0.50) anneal at 300˚C, curve (f), whereas the trap *H*Ga(0.20) is still present at the maximum annealing temperature of 350˚C used (note: the samples degraded beyond measurable conditions after annealing at >350˚C). The identity of these secondary defects is not clear at the moment.

Table 6.2. Electronic properties of defects introduced in B-doped epi-Si.

Defect	E_T (eV)	σ_a (cm^2)	T_{peak}[a] (K)	T_{in}[b] (˚C)	T_{out}[c] (˚C)	Defect identity
After	*Irradiation*					
*H*B(0.17)	E_V + 0.17	5.2 x 10^{-17}	115	RT	100	?
*H*B(0.18)	E_V + 0.18	1.3 x 10^{-16}	115	RT	225	$V_2^{+/0}$ [13,14.15]
*H*B(0.23)	E_V + 0.23	2.6 x 10^{-16}	137	RT	---	H-related? [11,15]
*H*B(0.34)	E_V + 0.34	1.6 x 10^{-15}	190	RT	100	?
*H*B(0.35)	E_V + 0.35	4.5 x 10^{-16}	190	RT	---	C_I-O_I [13,15]
*H*B(0.45)	E_V + 0.45	3.4 x 10^{-14}	240	RT	150	B-related?
After	*Annealing*					
*H*B(0.39)	E_V + 0.39	2.5 x 10^{-16}	230	150	300	B-related?

[a]Peak temperature at a rate window of 80 s^{-1}, [b]Temperature at which the defect is introduced. [c]Temperature at which the defect is removed.

6.3.3 Electron irradiation-induced defects in B-doped epitaxial grown Si

Primary hole traps *H*B(0.17), *H*B(0.18), *H*B(0.34), *H*B(0.35) and *H*B(0.45) were introduced by electron-irradiation in B-doped epitaxial Si, as depicted in Fig. 6-5 (a). The defect's electronic properties summarized in Table 6.2 were extracted from the Arrhenius plots shown in Fig. 6-7. Similar to the nomenclature used in the Ga doped sample, in this case '*H*' is the hole trap, 'B' is the dopant and '0.17' is the activation enthalpy, i.e. (E_V + 0.17) eV. The traps *H*B(0.17) and *H*B(0.18) have electronic structures (evidenced by the Arrhenius plots in Fig. 6-7) and annealing characteristics similar to *H*Ga(0.18) and *H*Ga(0.19) respectively, observed in the Ga-doped sample. *H*B(0.18) has been identified as the (+/0) of the divacancy [13,14], but the identity of *H*B(0.17) is not clear at the moment. The deduced introduction rates for the dominant levels *H*B(0.18) and *H*B(0.35) after 1 MeV electron irradiation were 5.0 x 10^{-3} cm^{-1} and 2.0 x 10^{-3} cm^{-1} respectively.

.

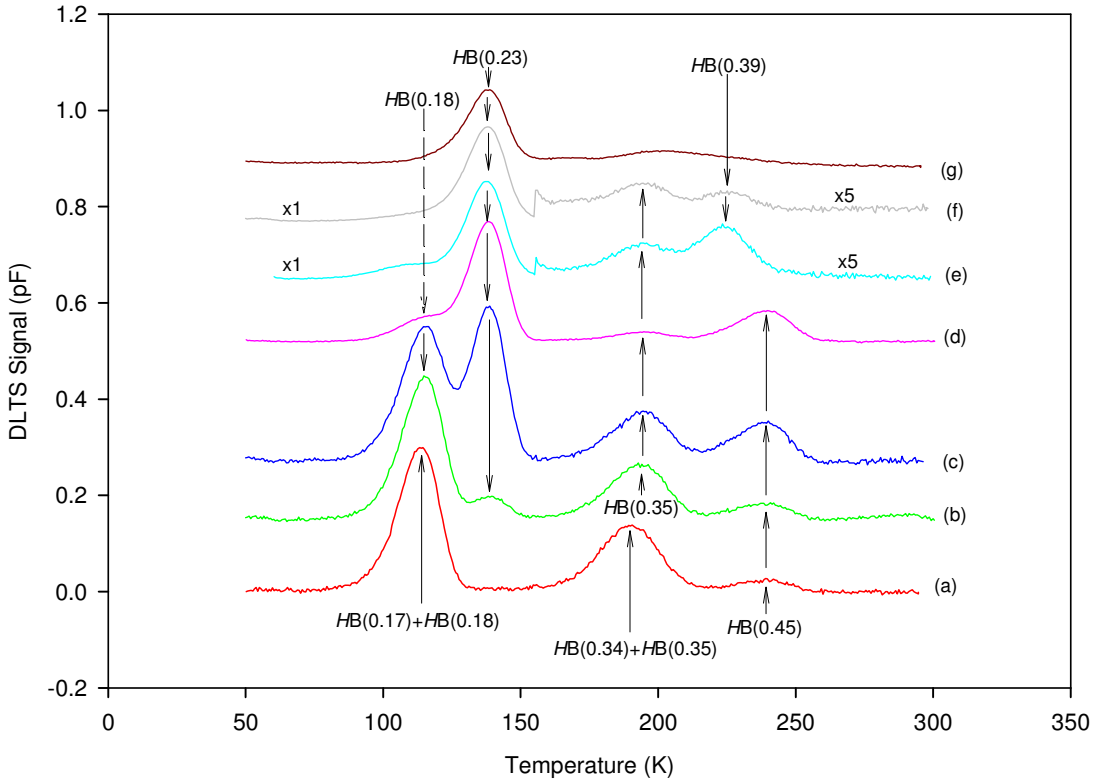

Fig. 6-5. DLTS spectra showing defects introduced in 1 MeV electron irradiated B – doped epitaxial Si for as (a) as-irradiated and after annealing for 20 minutes at (b) 100˚C, (c) 125˚C, (d) 150˚C, (e) 200˚C, (f) 250˚C and (g) 325˚C. The spectra were recorded at a rate window (RW) of 80 s^{-1}, a quiescent reverse bias of V_r = -2 V with a filling pulse V_p = 0.5 V and a pulse width of 1 ms.

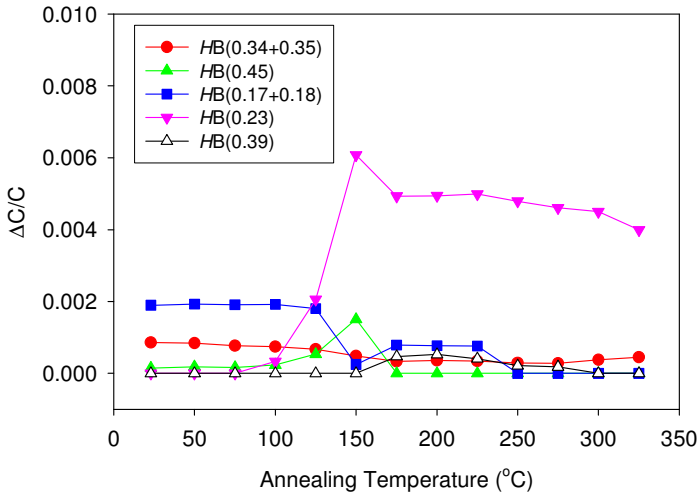

Fig. 6-6. Isochronal annealing behavior of defects in electron-irradiated B-doped epitaxial Si.

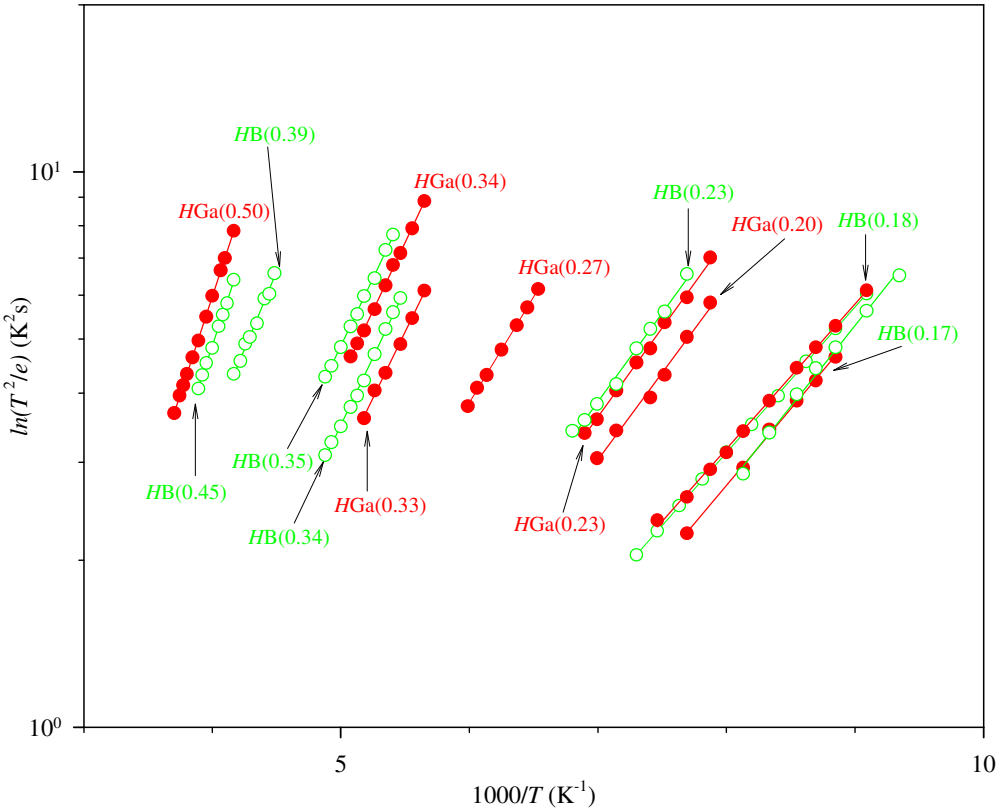

Fig. 6-7. Arrhenius plots of the primary and secondary defects introduced in B-doped epitaxial Si (green circles) compared to those introduced in Ga-doped Si (red circles) by 1 MeV electron irradiation.

*H*B(0.35) has been identified as the C_I-O_I complex [13,16] and the origin of *H*B(0.45) is speculated to be B related [13]. The annealing behavior of the defects introduced by

electron irradiation are depicted in Fig. 6-6 and Fig, 6-7. Similar to defects introduced in Ga-doped sample, *H*B(0.23) show reverse annealing characteristics in the temperature range between 100˚C and 150˚C as shown in Fig. 6-7 and this trap has been attributed to a H-related defect [11]. Upon annealing at 175˚C, *H*B(0.39) was introduced. Since this level is not observed in the Ga-doped sample, it is speculated that it might be B-related.

6.3.4 Electron irradiation-induced defects in B-doped Czochralski grown Si

In order to shed more light on the radiation induced defects in p-type silicon, defect characterization work has been extended to boron-doped Cz grown silicon. These samples have higher oxygen concentration when compared to epitaxial grown silicon.

Table. 6.3. Electronic properties of defects induced in B-doped Cz Si by 1 MeV electrons

Defect	E_T (eV)	σ_a (cm^2)	T_{peak}[a] (K)	T_{in}[b] (˚C)	T_{out}[c] (˚C)	Defect identity
After	*Irradiation*					
*H*B(0.17)	E_V + 0.17	1.3 x 10^{-17}	115	RT	100	?
*H*B(0.18)	E_V + 0.18	1.1 x 10^{-16}	115	RT	200	$V_2^{+/0}$ [4,10,11]
*H*B(0.23)	E_V + 0.23	2.0 x 10^{-16}	137	RT	---	H-related? [11]
*H*B(0.34)	E_V + 0.34	3.7 x 10^{-15}	190	RT	100	?
*H*B(0.35)	E_V + 0.35	2.5 x 10^{-16}	190	RT	175	C_I-O_I [4,13,17]
*H*B(0.45)	E_V + 0.45	3.2 x 10^{-14}	240	RT	150	B-related?
After	*Annealing*					
*H*B(0.22)	E_V + 0.22	2.1 x 10^{-15}	130	150	300	O-related?

[a]Peak temperature at a rate window of 80 s^{-1}, [b]Temperature at which the defect is introduced. [c]Temperature at which the defect is removed.

The electronic properties of defects introduced in B-doped Cz Si (extracted from the Arrhenius plots in Fig. 6-10) are summarized in Table 6-3. The primary hole traps observed after irradiation are *H*B(0.17), *H*B(0.18), *H*(0.23), *H*B(0.34), *H*B(0.35) and *H*B(0.45) they all have the same electronic structures to those introduced in epitaxial Si, as shown by Arrhenius plots in Fig. 6-10.

Upon annealing a new hole trap *H*B(0.22) is observed after annealing at 150˚C and this trap is not observed in the epitaxial sample, therefore it might be oxygen related. In Ga-doped a defect *H*Ga(0.20) has similar annealing characteristics. The trap level *H*B(0.23) is significantly suppressed after annealing at 150˚C and higher temperatures which is different from its annealing behavior as observed in the Ga-doped and epitaxial samples. The reason for this discrepancy is not clear at the moment.

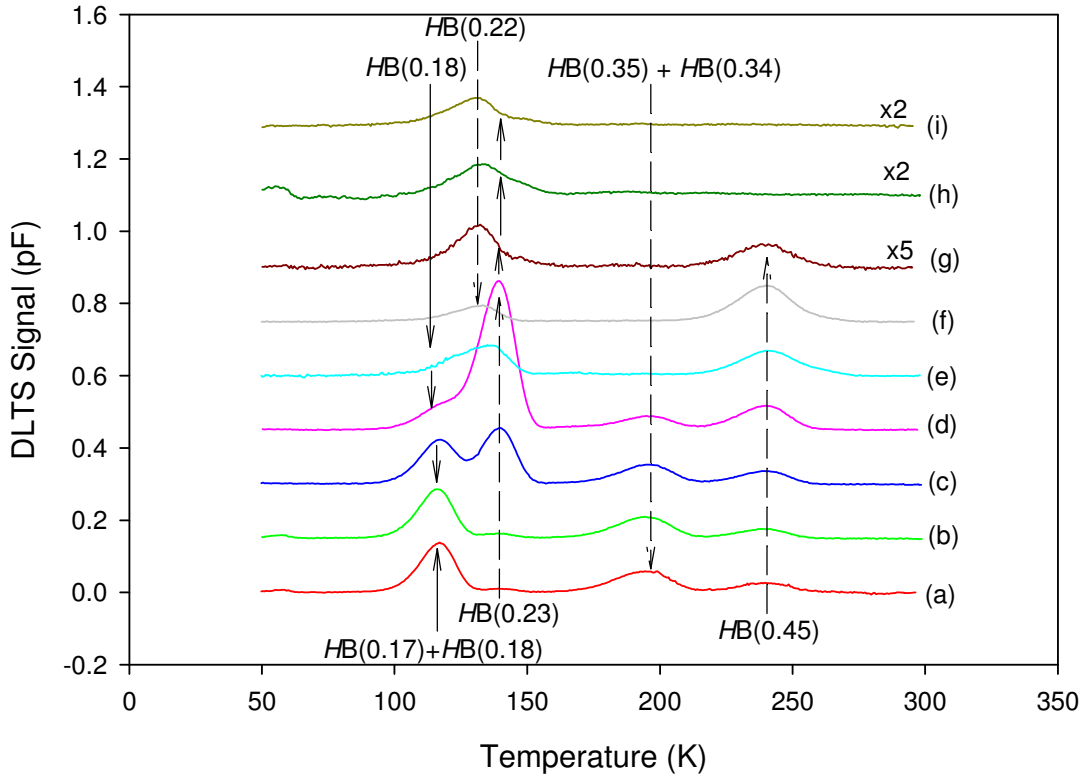

Fig. 6-8. Defects introduced in B-doped Cz Si after 1 MeV electron irradiation for (a) as-irradiated and after annealing at (b) 50˚C, (c) 100˚C, (d) 125˚C, (e) 150˚C (f) 175˚C, (g) 200˚C, (i) 275˚C . The spectra were recorded at a rate window (RW) of 80 s^{-1}, a quiescent reverse bias of V_r = -2 V with a filling pulse V_p = 0.5 V and a pulse width of 1 ms.

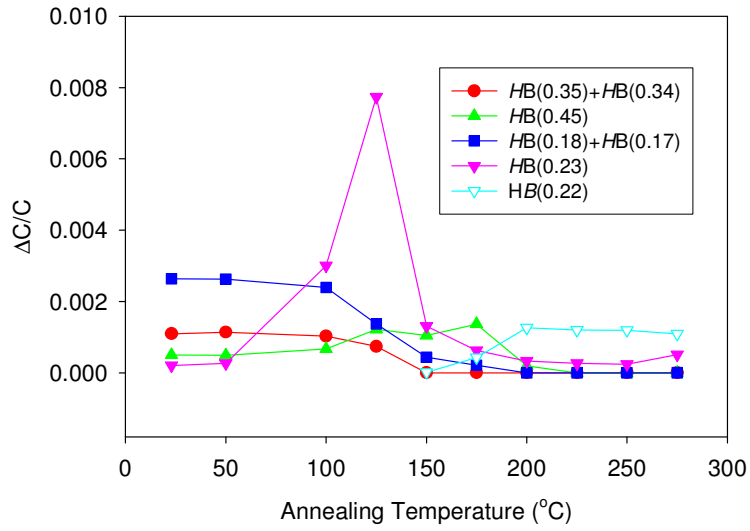

Fig. 6-9. Isochronal annealing behavior of defects in electron-irradiated B-doped Cz Si.

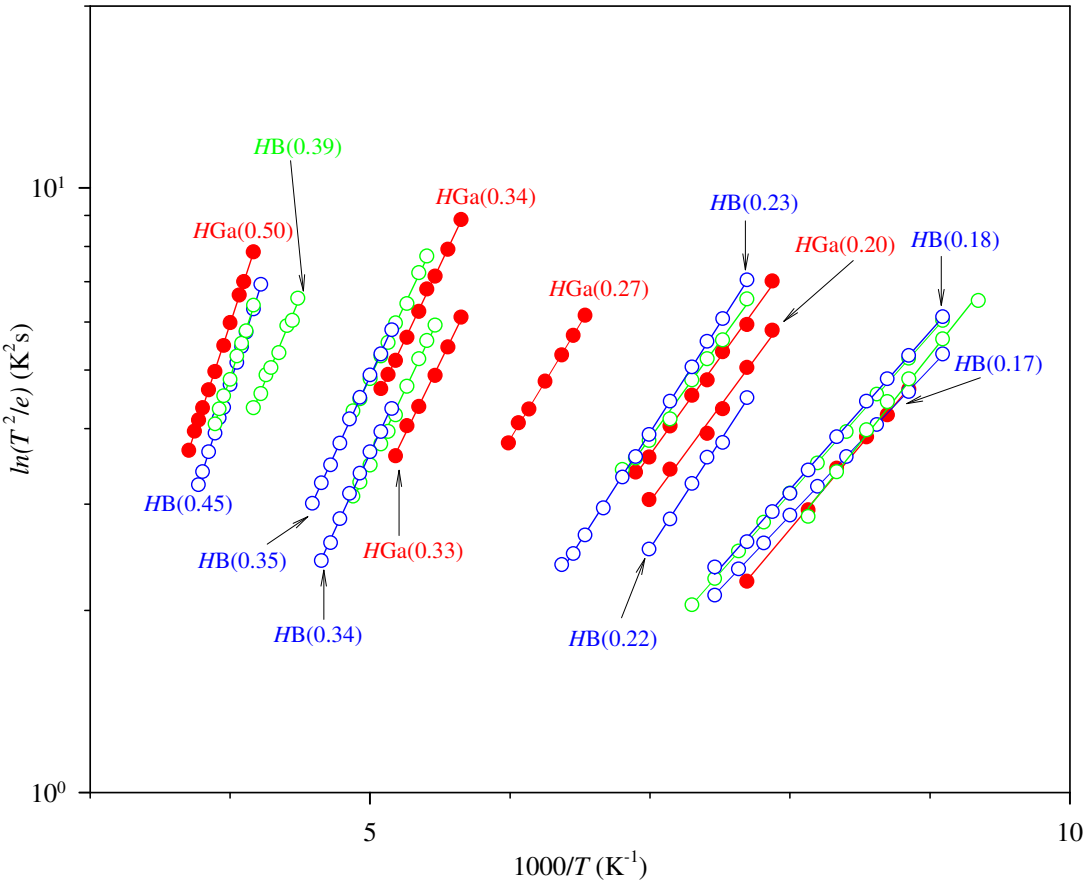

Fig. 6-10. Arrhenius plots of the primary and secondary defects introduced in B-doped epitaxial Si (green circles), Ga-doped Si (red circles) and B-doped Cz Si (blue circles) by 1 MeV electron irradiation.

6.4 Summary and conclusions

LDLTS has been succesfully used to separate closely spaced defects introduced in Ga-doped Cz, B-doped epitaxial and B-doped Cz silicon after 1 MeV electron irradiation. In Ga-doped samples, primary hole traps *H*Ga(0.18), *H*Ga(0.19), *H*Ga(0.23), *H*Ga(0.33) and *H*Ga(0.34) have been observed. The closely spaced pair of defects *H*Ga(0.18); *H*Ga(0.19) and *H*Ga(0.33); *H*Ga(0.34) appeared as a single peak in DLTS and was resolved by LDLTS. *H*Ga(0.19) has been identified as (+/0) charge state of the divacancy and *H*Ga(0.34) as the C_I-O_I center. The annealing studies further revealed the introduction of hole traps *H*Ga(0.20), *H*Ga(0.27), and *H*Ga(0.50). In the B-doped epitaxial and Cz silicon, the electron irradiation revealed similar hole traps *H*B(0.17), *H*B(0.18), *H*B(0.23), *H*B(0.34) *H*B(0.35) and *H*B(0.45). LDLTS was successfully used to separate the closely spaced defect levels *H*B(0.17) and *H*B(0.18) and similarly the levels *H*B(0.34) and *H*B(0.35) were resolved. *H*B(0.18) has been identified as the divacancy and *H*B(0.35) is the C_I-O_I complex. A defect level *H*B(0.22) was observed in the Cz sample but not in epitaxial sample, which may suggest that it is O-related. The deduced introduction rates for *H*B(0.17) and *H*B(0.35) after 1 MeV electron irradiation were 5.0 x 10^{-3} cm^{-1} and 2.0 x 10^{-3} cm^{-1} respectively, and introduction rates for *H*Ga(0.19) and *H*Ga(0.34) were 4.0 x 10^{-3} cm^{-1} and 2.5 x 10^{-2} cm^{-1} respectively and these rates are consistent with introductiomn rates related to electron irradiation.

References

[1] J. Schmidt and K. Bonde, *Phys. Rev. B* **69** (2004) 024107.

[2] D.C. Sawko and J. Bartko, *IEEE Nucl. Sci*. **30** (1983) 1756.

[3] A. Khan, M. Yamaguchi, Y. Ohshita, N. Dharmarasu, K. Araki, T. Abe, H. Itoh, T. Ohshima, M. Imaizumi and S. Matsuda, *J. Appl. Phys*. **90** (2001) 1170.

[4] M. Yamaguchi, A. Khan, T.K. Vu, Y. Ohshita and T. Abe, *Physica B* **340-342** (2003) 596.

[5] D. V. Lang, *J. Appl. Phys*. **45** (1974) 3023.

[6] L. Dobaczewski, P. Kaczor, I.D. Hawkins, and A.R. Peaker. *J. Appl. Phys*. **76** (1994) 194.

[7] L. Dobaczewski, A.R. Peaker and K.B. Nielsen, *J. Appl. Phys*. **96** (1994) 4689.

[8] A. Khan, M. Yamaguchi, T. Hisamatsu and S. Matsuda, *J. Appl. Phys*. **87** (2000) 2162.

[9] J. Trombetta and G.D. Watkins, *Appl. Phys. Lett*. **51** (1987) 1103.

[10] K. Nishimura, M. Yamaguchi, O. Anzawa, T.K. Vu, A. Khan, Y. Ohshita, T. Abe, M. Imaizumi, S. Matsuda, T. Ohshima and H. Itoh. *3rd World Conference on Photovoltaic Energy Conversion*, May 11-18 2003 Osaka, Japan plenary, Oral.

[11] Y. Tokuda and H. Sato, *Mater. Sci. In Semiconductor Processing*, **6** (2003) 277.

[12] P.M. Mooney, L.J Cheng, M. Süli, J.D. Gerson, and J.W. Corbett, *Physical Review B*, **15** No.8 (1977) 3836.

[13] M. Mamor, M . Willander, F.D. Auret, W. Meyer and E. Sveinbjörnsson, *Physical Review* B **63** (2000) 045201.

[14] B.J. Baliga and A.O. Evwaraye, *J. Electrochem. Soc*. **130** (1983) 1916.

[15] O. Feklisova, N. Yarykin, E.B. Yakimov and J. Weber, *Physica B*, **308-310**, (2001) 210.

[16] G.L. Miller, D. Lang, and L.C Kimerling, *Ann. Rev. Mater. Sci*. **7** (1977) 377.

[17] F.D. Auret, P.N.K. Deenapanray, *Critical Review in Solid State Mater. Scie.* **29** (2004) 1.

List of Publications

1. Cloud Nyamhere, P.N.K. Deenapanray, F.D. Auret and F.C. Farlow, "*Characterisation of Defects Created in Cz and epitaxial Si doped with Ga or B using Laplace-DLTS*", Physica B **376-277** (2006) 161-164.
2. Cloud Nyamhere, A.G.M. Das, F.D. Auret and M. Hayes, "*Deep Level Transient Spectroscopy Characterisation of Defects Introduced in p-Si Electron Beam Deposition and Proton Irradiation*", Journal of Physics, Conference Series, vol.**100** (2008), 042004.
3. A.G.M. Das, C. Nyamhere and F.D. Auret *"A Comparitive Study of electronic properties of defects introduced in p-Si (i) During Electron Beam Deposition of Ti/Mo, (ii) by proton irradiation and (iii) by electron irradiation*", Surface and Coatings Technology, Vol. **203** (2009) 2628-2631.

Chapter 7

Defects introduced in n- and p-type Si during contacts fabrication by electron beam deposition (EBD)

7.1 Introduction

It is well known that metallization techniques, e.g. sputtering and electron beam deposition (EBD), can introduce electrically active defects at and close to the metal-semiconductor junction [1]. The electron beam deposition technique is an important device processing step as it is used to evaporate metals with melting point greater than 1500˚C. Although process induced defects on different semiconductors have been characterized before, there is still lack of understanding on the type of radiation particles that create damage during device fabrication by electron beam deposition. It is generally believed that defects introduced by EBD are due to energetic ionized residual vacuum gases generated by collision between the gas particles and the electron beam. The ionized particles are accelerated onto the sample by the electric and magnetic fields present in the EBD chamber [2]. It is important to characterize these process induced defects so as to reduce or eliminate (by annealing) those that have adverse on the device performance.

Characterization of defects introduced in Si by EBD of metals and their annealing have been previously reported [1]. A complete annealing study, which establishes the removal of all defects, is necessary in order to standardize processing conditions for obtaining a defect-free space charge region below Schottky contacts formed by EBD [3]. In this study we have used LDLTS [4,5] and DLTS [6] as the characterization techniques. LDLTS is a powerful tool which can separate defect levels with similar emission properties.

7.2 Experimental Procedure

Boron-doped Cz silicon (p-type), with carrier concentration of 1.5 x 10^{16} cm^{-3} and phosphorus – doped (n-type), with carrier concentration of 5.0 x 10^{16} cm^{-3} were used for this study. The samples were cut into 1 cm x 0.4 cm sizes before cleaning. Prior to metallization the samples were chemically cleaned by degreasing in boiling trichloroethylene and then in boiling iso-propanol followed by an etching step in dilute HF, i.e. HF:H_2O (1:6) to remove the oxide layer. The samples were then rinsed in de-ionized water and blow-dried in nitrogen and thereafter immediately loaded into the vacuum chamber which was evacuated to a pressure of below 1 x 10^{-6} mbar to reduce oxide build-up before metallization.

On the p-type samples, titanium and then molybdenum, 100 nm thick each, were deposited through a circular mask of 0.48 mm in diameter, using electron beam deposition. The source of electron beam is a VARIAN 10 kW e-gun which employs a 10 kV (1 A) power source for the anode and a filament current of 40 A at 10 V. An electric field and magnetic field focus and accelerate the electric beam to the target metal. In-Ga eutectic was rubbed on the back-surface of the sample as the ohmic contact.

Similarly, on n-type samples, cobalt (Co), platinum (Pt), or ruthenium (Ru) Schottky contacts were fabricated through a circular of 0.48 mm in diameter using electron beam deposition. In-Ga eutectic was used as the back-surface ohmic contact.

After metallization current-voltage (*I-V*) and capacitance-voltage (*C-V*) were used to extract the free carrier concentration and monitoring the quality of the diodes. To determine the signature of the defects induced by electron beam deposition, DLTS and Laplace (LDLTS) were used. The defect 'signatures' (i.e. activation enthalpy in eV for holes or electrons E_T, and apparent capture cross-section, σ_a) were determined from Arrhenius plots of $\ln(T^2/e)$ vs. $1000/T$, where e is either the hole or electron emission rate and T is the measurement temperature. To shed more light on the structure and identity of defects, isochronal annealing cycles were done from room temperature up to 600°C. The defect depth profiles (i.e. defect concentration versus

depth) were obtained by fixed bias - variable pulse method with the edge region correction suggested by Zohta and Watanabe [7].

7.3 Results

The electrical characteristics of the defects introduced during metallization by electron beam deposition on n-type and p-type silicon is presented in this section. DLTS and LDLTS have been used to probe the defect electronic properties and depth profiles below the semiconductors surface.

7.3.1 Electron beam deposition induced defects in p-type silicon

Defects introduced during metallization, revealed by a DLTS spectrum in Fig. 7-1, curve (a) are *H*(0.17), *H*(0.23), *H*(0.37) and *H*(0.49). In this nomenclature "*H*" means "hole trap" and the number after *H* is the activation energy, in eV, obtained from the Arrhenius plots shown in Fig. 7-3. The electronic properties of the defects introduced during EBD are summarized in Table. 7.1.

Table 7.1. Electronic properties of defects introduced during EBD of Ti/Mo contacts on B-doped Cz Si

Defect	E_T (eV)	σ_a (cm^2)	T_{peak} [a] (K)	T_{in} [b] (°C)	T_{out} [c] (°C)	Defect identity
After	*electron*	*beam*	*deposition*			
H(0.17)	0.17	6.1 x 10^{-16}	100	RT	450	?
H(0.23)	0.23	1.7 x 10^{-15}	150	RT	400	H-related [8]
H(0.37)	0.37	1.5 x 10^{-15}	192	RT	450	C_I-O_I [8,9,10]
After	*annealing*					
H(0.39)	0.39	4.3 x 10^{-16}	213	350	450	?
H(0.49)	0.49	1.0 x 10^{-15}	265	350	550	B-H?

[a] Peak position at a rate window of 80 s^{-1}. [b]Temperature at which the defect is introduced. [c]Temperature at which the defect is removed.

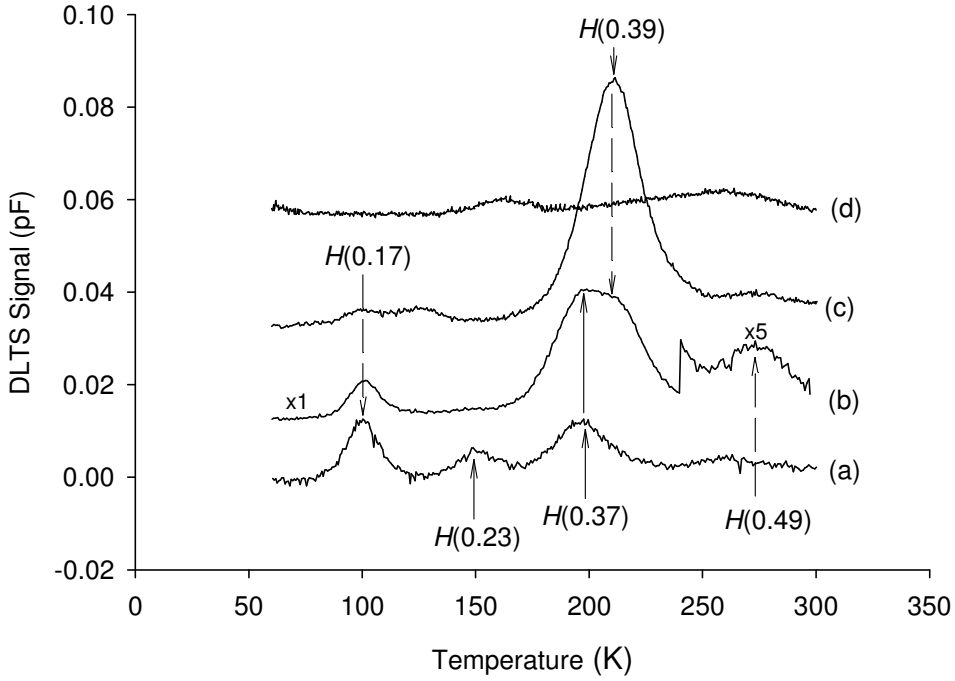

Fig. 7-1. DLTS spectra of the defects present in the depletion layer below the Ti/Mo Schottky contact on p-type Si (a) after deposition and after annealing at (b) 400˚C, (c) 450˚C, and (d) 550˚C. The spectra were recorded at an emission rate of 80 s^{-1}, a quiescent reverse bias of -2 V and a filling pulse amplitude of 2.2 V.

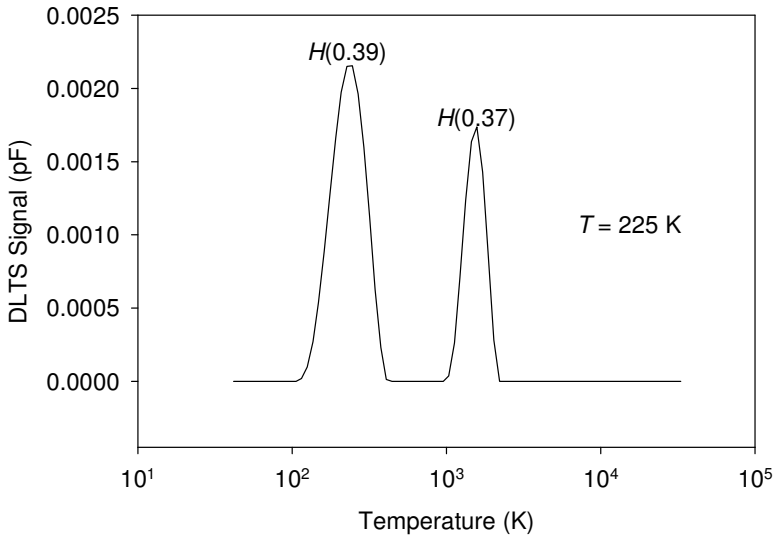

Fig. 7-2. LDLTS spectrum of the peak marked "H(0.37) + H(0.39)", recorded at 225 K. LDLTS clearly separates the signals of the two defects.

It should be pointed out that these defects were not observed in identical silicon samples on which Ni Schottky contacts were fabricated by resistive evaporation. All

the defects are therefore introduced by EBD. The annealing behavior of defects introduced by electron beam deposition of Ti/Mo is presented in Fig. 7-2, curves (a-d). Annealing at 400˚C removed *H*(0.23) (curve(b)), while *H*(0.17) and *H*(0.37) were removed after annealing at 450˚C (curve(c)). The defect level *H*(0.39) was introduced at 350˚C and its concentration reached a maximum at 450˚C and thereafter it annealed out at 550˚C. After annealing at 400˚C, LDLTS was used to separate the traps *H*(0.37) and *H*(0.39) which was not possible with DLTS as shown in Fig. 7-2. After annealing at 550˚C and higher temperatures, no defect peaks could be detected within the detection limit of our system.

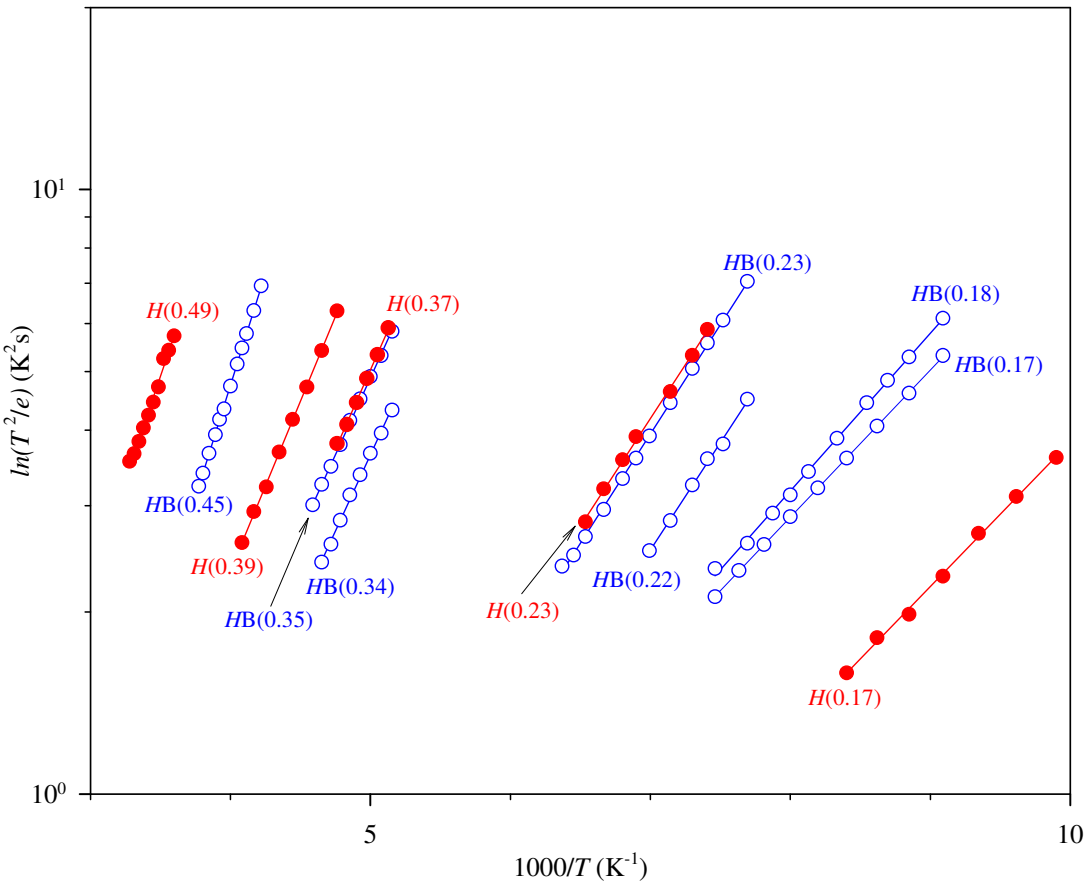

Fig. 7-3. Arrhenius plots of the defects present in the depletion layer below the Ti/Mo Schottky contact on B-doped Si after deposition (red circles) compared to the defects introduced in similar samples after 1 MeV electron irradiation (blue circles).

As shown in Table 7.1 and Arrhenius plots in Fig. 7-3, most of these defects have different properties to those introduced by electron irradiation of similar samples

presented in chapter 6. *H*(0.23) has been attributed to a H- related defect [8] which is similar to a defect level *H*B(0.23) discussed in chapter 6. *H*(0.37) has similar electronic properties to the C_I-O_I. A defect at E_V + 0.35 eV with a similar annealing behavior has also been reported by Auret *et al* after electron irradiation of p-type Si, as well as after EBD of contacts on p-type Si [9]. It has been convincingly demonstrated that this level is associated with the C_I-O_I [10]. *H*(0.39) may be a defect that forms as the C_I-O_I breaks up during annealing [10]. The nature of *H*(0.49) is not clear at the moment. It should be pointed out, however, that Mooney *et al* [8] and Auret *et al* [9] observed levels at E_V + 0.48 eV and E_V + 0.49 eV, respectively, in electron irradiated, B-doped Si. Although the trap level *H*(0.17) has similar energy level to the divacancy it should be pointed out that the level observed here has different structure and properties to the divacany as evidenced by the Arrhenius plots in Fig. 7-3 and also it anneals out at a much higher temperature than the annealing range (250˚C - 300˚C) of the divacancy [11].

DLTS depth profiles of EBD induced defects indicated that the concentration of all the defects decreased from the surface into the Si away from the junction (examples of such profiles have been presented in section 7.3.2). This is due to the fact that EBD introduces defects at and below the surface, which will then diffuse deeper into the material and form more stable complexes [1]. These defects have been shown to be caused by energetic particles accelerated from the vicinity of the electronic filament onto the sample by the electric and magnetic fields present in the vicinity of the metal source [2].

To shed more light on the source of defects during the deposition process, TRIM (version 2006.02) [12] simulations are presented here. Figs. 7-4 (a-d) show the TRIM simulation of the ion ranges and damage created by several common residual vacuum gases, which are thought to be responsible for the damage on substrate surface during electron beam deposition. For a maximum ion energy of 10 keV (which is expected in our electron beam deposition system), the projected ion range for C, O, and N is on average ~30 *n*m producing on approximately, 3 vacancies/ion/*n*m, whereas H ions of the same energy will have a projected range of 132 *n*m and each ion producing 18 x 10^{-3} vacancies/*n*m. Therefore it is expected that the primary damage will be very close to the semiconductor surface and the vacancy-interstitial pairs created will then

diffuse until they form stable complex defects. Considering the number of vacancies/*n*m created during EBD the formation of higher order vacancies or interstitial complexes is possible.

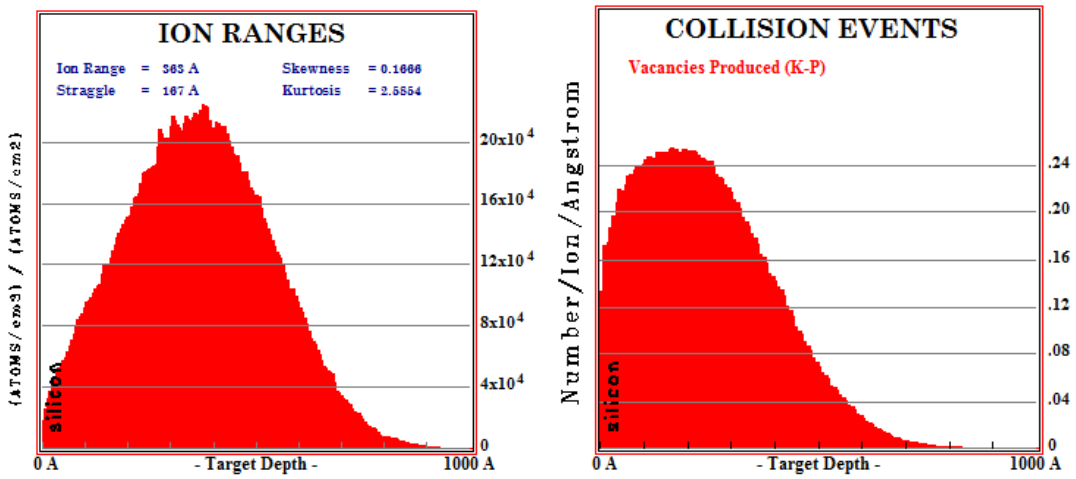

(i) (ii)

Fig. 7-4 (a). (i) TRIM simulation for the projected range and (ii) damage events of 10 keV carbon ions in silicon.

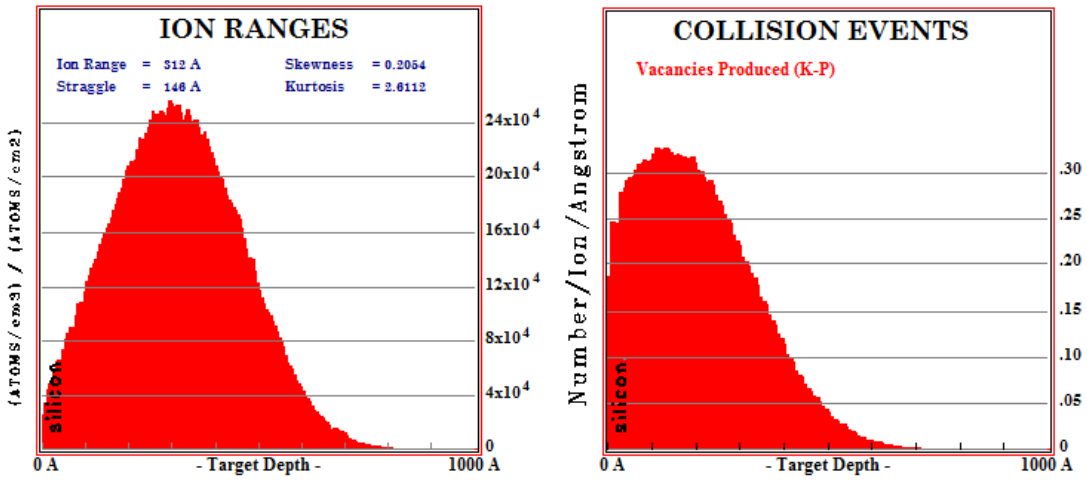

(i) (ii)

Fig. 7-4 (b). (i) TRIM simulation for the projected range and (ii) damage events of 10 keV nitrogen ions in silicon.

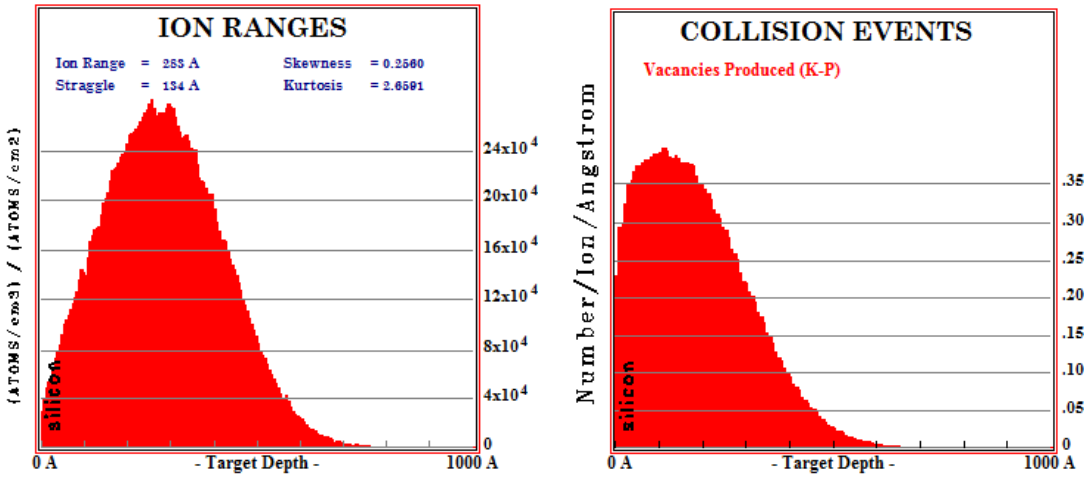

(i) (ii)

Fig. 7-4 (c). (i) TRIM simulation for the projected range and (ii) damage events of 10 keV oxygen ions in silicon.

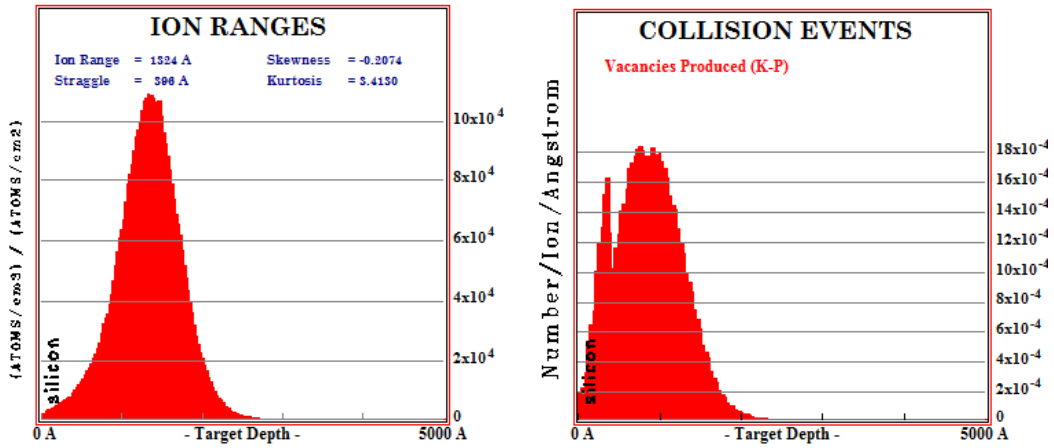

(i) (ii)

Fig. 7-4 (d). (i) TRIM simulation for the projected range and (ii) damage events of 10 keV hydrogen ions in silicon.

7.3.2 Electron beam deposition induced defects in n-type silicon

After the electron beam deposition of Ru Schottky barrier diodes, the defect levels *E*(0.45), *E*(0.42), *E*(0.22), *E*(0.15) and *E*(0.05) were introduced as shown in Fig. 7-5 (a). In this nomenclature, "*E*" is electron trap and the number '0.45' is the activation enthalpy (in eV). There were no defect levels observed within the detectable limit of our DLTS system in the same samples after metallization of Ni Schottky contacts by resistive evaporation. Defect *'signatures'* for the EBD induced defects which were extracted from the Arrhenius plots shown in Fig. 7-8 are

summarized in Table 7-2. The EBD induced defects have been compared to those introduced by MeV irradiation of similar samples.

Table 7.2. Electronic properties of defects introduced during EBD of Ru contacts on P-doped Si and those introduced by MeV electron irradiation in similar samples.

Defect	E_T (eV)	σ_a (cm^2)	T_{peak} [a] (K)	Defect	E_T (eV)	σ_a (cm^2)	T_{peak} [a] (K)	Defect identity
Electron	*beam*	*deposition*		*MeV*	*electron*	*irradiation*		
E(0.45)	E_C - 0.45	1.3 x 10^{-14}	215	E(0.46)	E_C -0.46	1.5 x 10^{-14}	215	V-P [2,13,14]
E(0.42)	E_C - 0.42	4.1 x 10^{-14}	205	E(0.43)	E_C -0.43	3.0 x 10^{-14}	205	$V_2^{-/0}$ [2,13,14]
E(0.22)	E_C - 0.22	9.0 x 10^{-15}	123	E(0.24)	E_C -0.24	7.8 x 10^{-15}	123	$V_2^{=/-}$ [13,14]
				E(0.17)	E_C -0.17	1.1 x 10^{-14}	90	V-O [13,14,15]
				E(0.14)	E_C -0.14	1.6 x 10^{-13}	67	C_s-Si_i ?
E(0.15)	E_C - 0.15	2.5 x 10^{-15}	83					?
E(0.05)	E_C - 0.05	1.4 x 10^{-19}	57					?
After	*annealing*							
E(0.28)	E_C - 0.28	8.6 x 10^{-17}	180					C_i -? [13,15,16]
E(0.18)	E_C - 0.18	3.8 x 10^{-16}	110					?

[a] Peak position at a rate window of 80 s^{-1}.

E(0.45) is the well known vacancy-phosphorus (E-center) and E(0.42) has similar electronic characteristics to the single charge state of the divacancy, while E(0.22) is attributed to the double charge state of the divacancy [2,13,14]. These two traps have similar structures to E(0.46) and E(0.43) observed after MeV electron irradiation. The E(0.42) and E(0.45) were successfully separated using LDLTS as shown in Fig. 7-6.

The origin of *E*(0.15) and *E*(0.05) is still subject to speculation at the moment. After annealing the defects were monitored by DLTS as shown in Figs. 7-5 and 7-7.

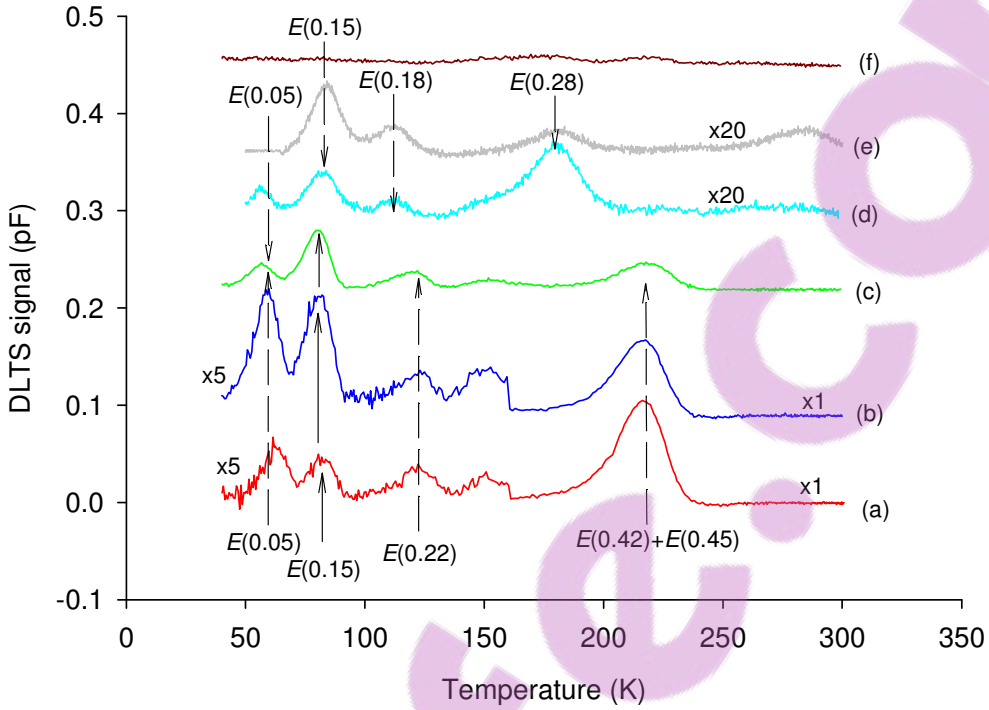

Fig. 7-5. DLTS spectra of defects introduced in P-doped Si after Ru Schottky contacts fabrication using EBD for (a) for as-deposited sample, and after annealing at (b) 150°C, (c) 250°C, (d) 350°C, (e) 400°C and (f) 450°C. The spectra were recorded at a quiescent reverse bias of -2 V, a filling pulse of 1.2 V and rate window (RW) of 80 s^{-1}.

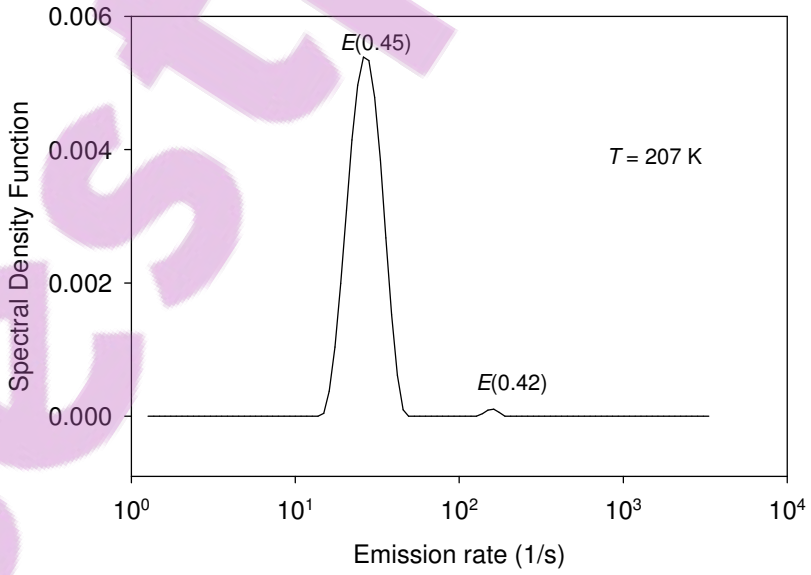

Fig. 7-6. LDLTS spectra for the levels E(0.45) and E(0.37) recorded at 207 K.

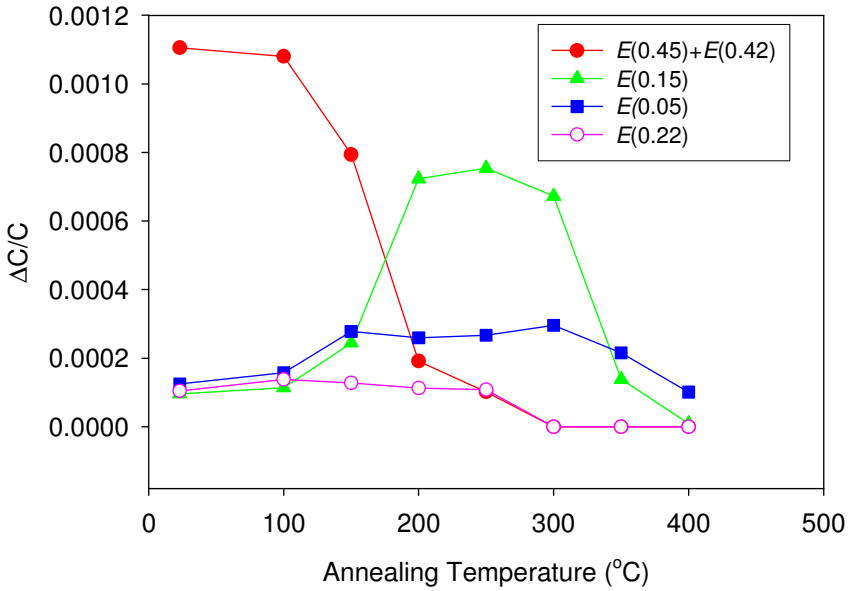

Fig. 7-7. Annealing behaviour of primary defects introduced in p-type silicon by electron beam deposition.

Annealing at above 250˚C, *E*(0.18) and *E*(0.28) were introduced, and *E*(0.18) has a different structure to the trap level *E*(0.17) assigned to the V-O (A-center) which was observed after electron irradiation as evidenced by the Arrhenius plots in Fig, 7-8, while *E*(0.28) is thought to be interstitial carbon- related [15,16]. Electron irradiation introduced the level *E*(0.14) which has different structure to *E*(0.15) observed after electron beam deposition. The depletion layer was defect-free after annealing at 550˚C or higher.

Depth profiling of the *E*-center shows a decrease in defect concentration with depth from the semiconductor surface as shown in Fig. 7-9, which is characteristic of damage caused by heavy energetic particles whose energy decreases with depth. The depth profiles of defects introduced after Ru and Pt Schottky contacts fabrication on the similar samples using EBD are depicted in Fig. 7-9 curves (a) and (b) respectively. The defect concentration at the semiconductor surface is higher for Ru than for Pt. This is attributed to the fact that Ru has a higher melting point (2250˚C) than Pt (2041˚C), hence during Ru deposition a higher filament current is used, therefore the particles in the vicinity of the filament will have a higher flux (than in case of Pt deposition) creating much more damage on and beneath the semiconductor surface.

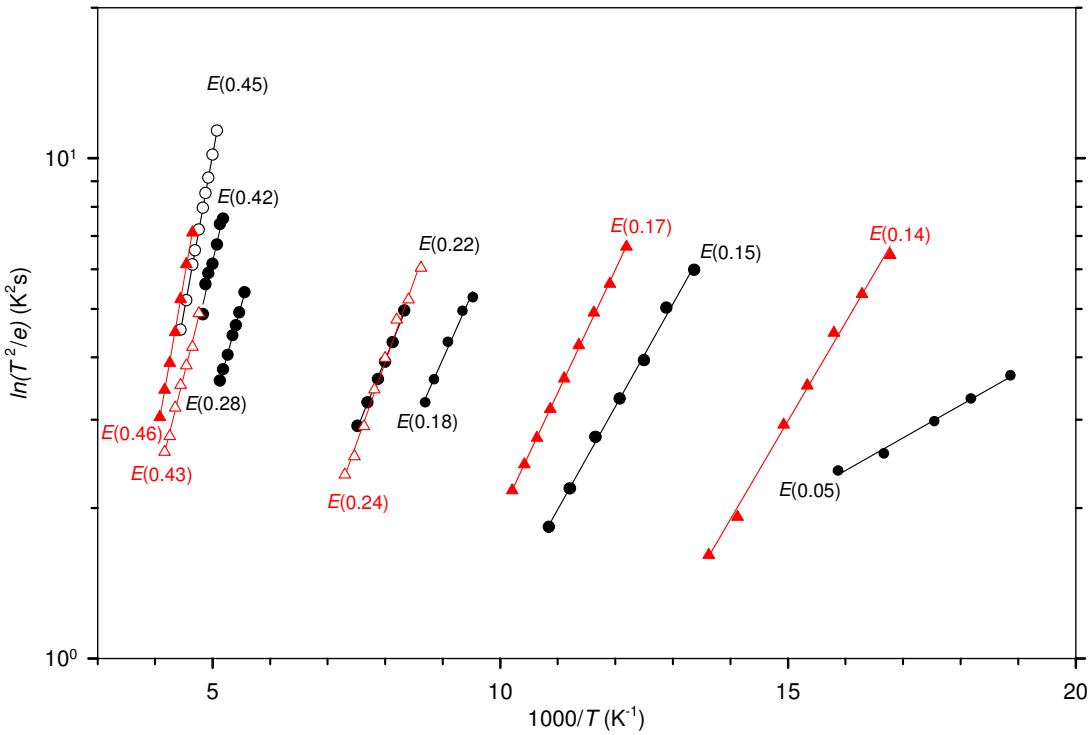

Fig. 7-8. Arrhenius plot of defects in P-doped Si after Ru Schottky contacts fabrication using EBD (black circles) and after 1 MeV electron irradiation (red triangles).

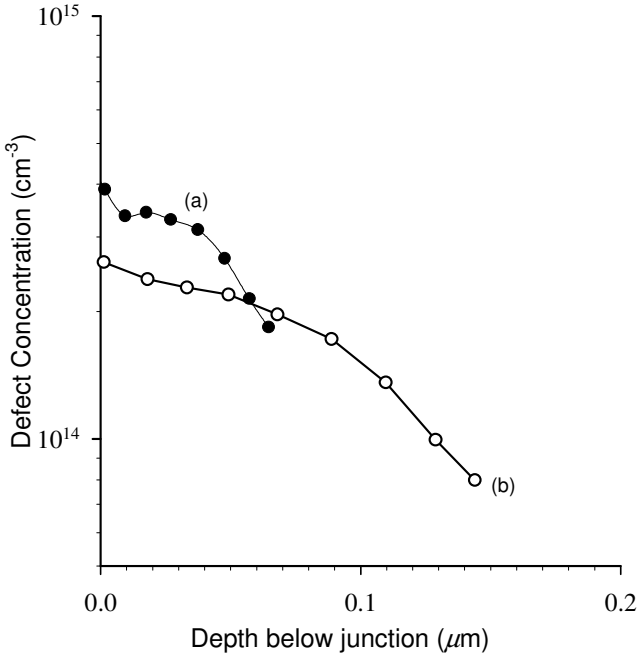

Fig. 7-9. Depth profile of E-center after (a) Ru (b) Pt Schotky contacts fabrication P-doped Si using EBD. Measurements were recorded using a fixed bias of -2 V and a variable pulse method, ref. 7.

7.4 Summary and Conclusions

Defects introduced during metallization on B-doped, and P-doped Si using EBD have been characterized by DLTS and LDLTS, and compared to those introduced by MeV electron irradiation in similar samples. The thermal stability of EBD induced defects have been investigated in the temperature range (100˚C – 600˚C). In case of p-type Si the Mo that was added on top of the Ti prevented annealing degradation of the Ti contact with the semiconductor at higher annealing temperatures. DLTS revealed that the main defects introduced during metallization are hole traps *H*(0.17), *H*(0.23), and *H*(0.37). After annealing two secondary defects *H*(0.39) and *H*(0.49) were observed. The trap *H*(0.37) has been assigned to the C_I-O_I and *H*(0.23) is hydrogen-related. The structure of *H*(0.17) seems to have a different structure to that of the single charged donor state of the divacancy while the origin of both *H*(0.39) and *H*(0.49) is still not clear. After annealing at 550˚C and higher a defect-free depletion region was obtained. LDLTS was successfully used to deconvolute signals of *H*(0.37) and *H*(0.39) defects which are both present after annealing at above 400˚C. It was concluded that electron beam deposition introduces some defects which are common to those introduced by high energy electron irradiation.

In phosphorus-doped Si, the primary defects introduced by EBD were *E*(0.45), *E*(0.42), *E*(0.22), *E*(0.15), and *E*(0.05). The closely spaced traps *E*(0.45) and *E*(0.42) were separated by LDLTS. *E*(0.45) has been identified as the V-P (*E*-center) while *E*(0.42) and *E*(0.22) have been identified as the single and double acceptor charge states of the divacancy, respectively. Upon annealing the defect levels *E*(0.18), and *E*(0.28) were observed. *E*(0.18) has a different structure to the trap *E*(0.17) observed after electron irradiation and assigned to the V-O (A-center). *E*(0.28) has been identified as being C_i- related. The identity of *E*(0.05) and *E* (0.15) is not clear at the moment. A defect-free depletion region was observed after annealing at 550˚C and higher. The depth profile of the, *E*-center (*E*(0.48)), showed a high concentration of the defects close to the metal - semiconductor surface and concentration decreasing with depth into the material.

References

[1] F.D. Auret and P.M. Mooney, *J. Appl. Phys*. Vol. **55** (1984) 984.

[2] C. Christensen, J.W. Petersen and A.N. Larsen, *Appl. Phys. Lett*. Vol. **61** (1992) 1426.

[3] F.D. Auret, A.G.M. Das, C. Nyamhere, M. Hayes and N.G. van der Berg, *Solid State Phenomena* **108-109** (2005) 561.

[4] L. Dobaczewski, P. Kaczor, I.D. Hawkins and A.R. Peaker, *J. Appl. Phys*. **76** (1994) 194.

[5] L. Dobaczewski, A.R. Peaker and K.B. Nielsen, *J. Appl. Phys*. **96** (1994) 4689.

[6] D.V. Lang, *J. Appl. Phys*. **45** (1974) 3023.

[7] Y. Zohta and M.O. Watanabe, *J. Appl. Phys*. **53** (1982) 1809.

[8] Y. Tokuda and H. Sato, *Mater. Scie. In Semiconductor Processing*, **6** (2003) 277.

[9] F.D. Auret and P.M. Mooney, *J. Appl. Phys*. **55** (1984) 984.

[10] J.M. Trombetta and G.D. Watkins, *Appl. Phys. Let*t. **51** (1987) 1103.

[11] K. Nishimura, M. Yamaguchi, O. Anzawa, T.K. Vu, A. Khan, Y. Ohshita, T. Abe, M. Imaizumi, S. Matsuda, T. Ohshima and H. Itoh. *3rd World Conference on Photovoltaic Energy Conversion*, May 11-18, 2003 Osaka, Japan plenary, Oral.

[12] J.P. Biersack and L.G. Haggmark, *Nucl. Instrum. Methods* **174** (1980) 257.

[13] P. Pellegrino, A. Y. Kuznestov and B.G. Svensson, *Physica B*, **273-274** (1999) 489.

[14] J. Lalita, N. Keskitalo, A. Hellén, C. Jadadisn and B.G. Svensson, *Nuclear Intruments and Methods in Physics Research* B ***120*** (1996) 27.

[15] P. Lévêque, A. Hallen, P. Pellegrino, B.G. Svensson and V. Privitera, *Nucl. Instr. and Meth. Phys. Res. B* **186** (2002) 375.

[16] J. Stahl, E. Fretwirst, G. Lindstrom and I. Pintilie, *Nucl. Instr. and Meth. A* **512** (2003) 111.

List of Publications

1. F.D. Auret, A.G.M. Das, C. Nyamhere, M. Hayes and N.G. van der Berg; "*Thermal Stability of Ti/Mo Schottky contacts on p-Si and Defects Introduced in p-Si During Electron Beam Deposition of Ti/Mo*", Solid state Phenomena, vols. **108-109** (2005) 561-566.
2. Cloud Nyamhere, A. Chawanda, A.G.M. Das, F.D. Auret and M. Hayes, "*Thermal stability of Co, Ni, Pt or Ru Schottky contacts on n-Si and defects introduced thereon during contacts fabrication using electron beam deposition*", Physica B, Vols. **401- 402** (2007) 226 - 229.
3. C. Nyamhere, A.G.M. Das, F.D. Auret and M. Hayes, "*Deep Level Transient Spectroscopy Characterisation of Defects Introduced in p-Si Electron Beam Deposition and Proton Irradiation*", Journal of Physics, Conference Series, vol.**100** (2008), 042004.
4. A.G.M. Das, C. Nyamhere and F.D. Auret "A Comparitive Study of electronic properties of defects introduced in p-Si (i) During Electron Beam Deposition of *Ti/Mo, (ii) by proton irradiation and (iii) by electron irradiation*", Surface and Coatings Technology, Vol. **203** (2009) 2628-2631.

Chapter 8

Radiation-induced defects in antimony-doped germanium after electron irradiation

8.1 Introduction

There is growing interest in Germanium (Ge) as a possible candidate for high performance complimentary metal-oxide-semiconductor (CMOS) devices because of its higher mobility when compared to silicon (Si) at low electric fields [1-2]. This has led to renewed interest in the complete understanding of origins and dynamic properties of radiation and process induced defects in Ge. Although several authors [3,4,5,6,7,8] have studied radiation defects introduced intentionally, by radiation or unintentionally, during processing stages, there is lack of understanding of the origins of most defects. In this chapter we have characterized defects, deliberately introduced by electron irradiation in n-type Ge doped with Sb using DLTS and LDLTS. The annealing characteristics of the defects are also presented to shed more light on the defect origin. Also presented in this chapter are the depth profile and the introduction rates of the *E*-center.

8.2 Experimental Procedure

Three sets of samples, (labeled Ge110, Ge111 and Ge100), of n-type, bulk grown Ge doped with Sb and supplied by Umicore have been used in this investigation. In the sample label nomenclature 'Ge110', Ge is germanium, 110 is the sample orientation. The doping levels were 2.2 x 10^{14} cm^{-3}, 1.0 x 10^{15} and 2.6 x 10^{15} for Ge110, Ge111 and Ge100 respectively. Before metallization the samples of 1cm x 1cm in size were first degreased and then etched in a mixture of H_2O_2:H_2O (1:5) for 1 minute. Immediately after cleaning they were inserted into a vacuum chamber where AuSb (0.6% Sb) was deposited by resistive evaporation process, on their back surfaces as ohmic contacts. The samples were then annealed at 350˚C in argon (Ar) for 10

minutes to reduce the contact resistivity of the ohmic contacts. Before the Schottky contact fabrication, the cleaning procedure above was repeated. Au contacts, 0.60 mm in diameter and 200 nm thick were deposited by vacuum resistive evaporation process. After the contact formation the samples were characterized by current – voltage (*I-V*) and capacitance – voltage (*C-V*) measurements at room temperature to determine the quality of the diodes. The samples were then irradiated by MeV electrons from a ^{90}Sr radionuclide source at different fluences. The energy distribution from this source is continuous with a primary peak energy of about 200 keV, a secondary maximum of about 1 MeV, and then it tails off to about 2 MeV [3]. After each and every dose the defects introduced were measured by DLTS and Laplace – DLTS. The current - temperature (*I-T*) and capacitance - temperature (*C-T*) measurements were also recorded. The '*signatures*' of radiation induced defects (i.e. activation enthalpy for the electron traps and hole traps, E_T, and apparent capture cross section, σ_a), were determined from Arrhenius plots of $ln(T^2/e)$ vs. $1000/T$, where 'e' is either the hole or electron emission rate, and T is the measurement temperature.

In order to investigate the defect annealing behaviour, the irradiated samples were annealed isochronally for 20 minutes in Ar gas from room temperature up to 500˚C.

8.3 Results

In this section the electronic and annealing properties of hole traps created in the samples after electron irradiation are discussed. The evolution of defects with increase in fluence and defects created in samples of different doping concentrations are revealed.

8.3.1 Defects introduced in Ge after electron irradiation with different doses

DLTS spectra of defects introduced in n-Ge after MeV electron irradiation at various doses are depicted in Fig. 8-1 and the defect 'signatures' extracted from Arrhenius plots (shown Fig. 8-4) are summarised in Table 8.1. No defect levels were detected within detection limit (about 10^{11} cm^{-3}) of our experimental system for the as-deposited samples, as shown in Fig. 8-1 (curves (a_e) and (a_h)). In the nomenclature

used here to label the curves, the subscripts 'e' and 'h' indicate that the spectrum is for electron traps and hole traps respectively.

Table 8.1. A summary of defects electron properties introduced in n-type Ge by electron irradiation.

Defect	E_T (eV)	σ_a (cm^2)	T^a_{peak} (K)	T^b_{out} (°C)	Defect origin
E(0.15)	$E_C - 0.15$	3.1 x 10^{-13}	78	150	Sb related?
E(0.20)	$E_C - 0.20$	2.3 x 10^{-13}	100	150	Sb and I related [2-4]
E(0.21)	$E_C - 0.21$	1.1 x 10^{-13}	101	150	Sb related [2-4]
E(0.23)	$E_C - 0.23$	9.7 x 10^{-13}	132	175	Sb and I related [2-4]
E(0.31)	$E_C - 0.31$	3.1 x 10^{-13}	151	125	I and impurity related [2-4]
E(0.38)	$E_C - 0.38$	6.1 x 10^{-14}	191	200	V-Sb (--/-) [2-6]
H(0.30)	$E_V + 0.30$	4.0 x 10^{-12}	142	200	V-Sb (0/-) [2-4]

[a]Peak temperature at a rate window of 80 s^{-1}, [b]Temperature at which defect is removed.

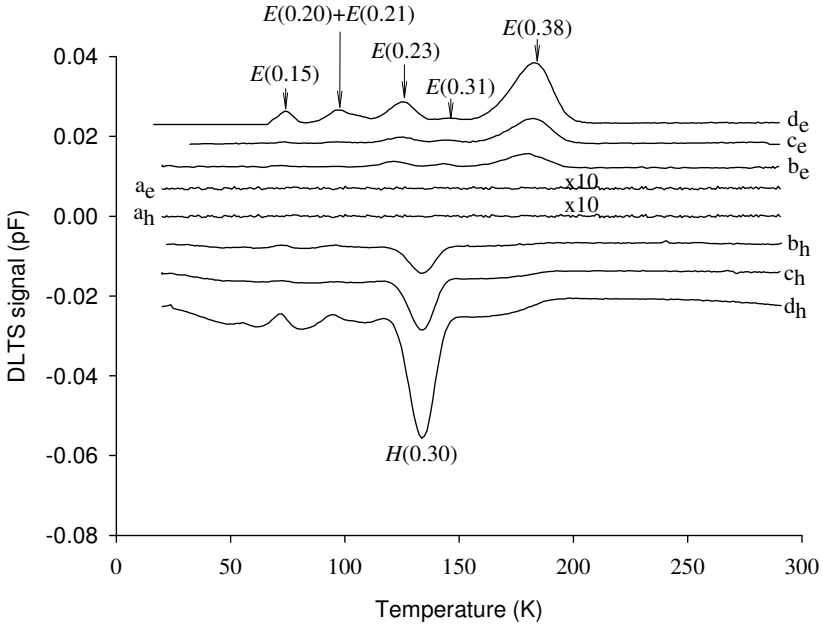

Fig. 8-1. DLTS spectra for sample Ge100 (a) as-deposited and after MeV electron irradiation at fluences of (b) 1.4 x 10^{13} e cm^{-2}, (c) 3.7 x 10^{13} e cm^{-2}, and (d) 9.2 x 10^{13} e cm^{-2}. The subscripts 'e' and 'h' on the graph labels stand for electron and hole traps respectively. These spectra were recorded at a rate window of 80 s^{-1} and quiescent reverse bias of -2 V with a filling pulse of 0 V and 3 V for electron and hole traps, respectively and a pulse width of 1 ms.

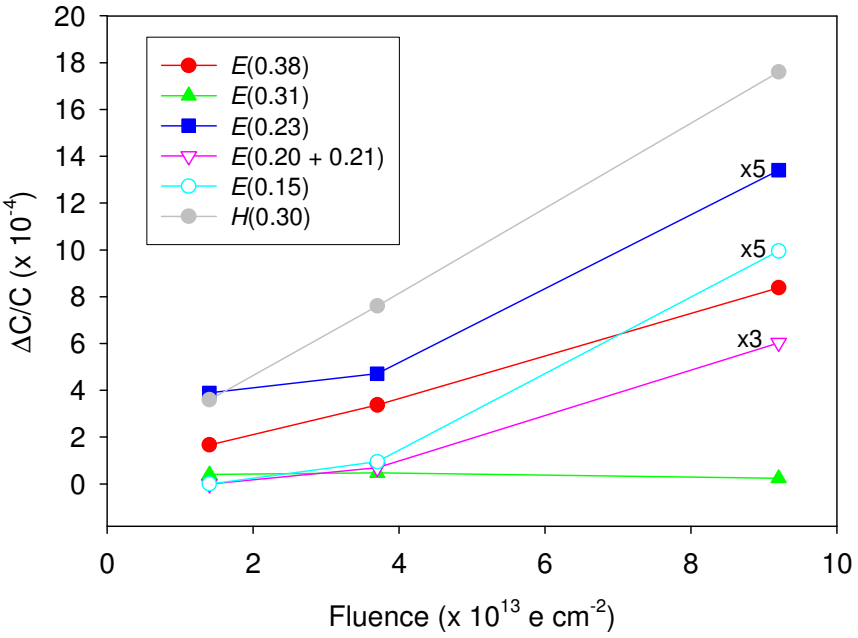

Fig. 8-2. Normalized DLTS peak height for each defect in the sample Ge100 as a function of fluence.

This proves that diode fabrication by resistive evaporation process does not introduce any detectable defect levels within semiconductor band gap. After irradiation with a fluence of 1.4 x 10^{13} e cm^{-2} a hole trap, *H*(0.30) is observed, curve (b_h) and *E*(0.38), *E*(0.31), *E*(0.23) trap levels are observable from curve (b_e). After a fluence of 9.2 x 10^{13} e cm^{-2}, three more electron traps *E*(0.21), *E*(0.20) and *E*(0.15) were introduced (curve (d_e)). Fig. 8-3 (a) depicts LDLTS spectra, for *E*(0.38), a single peak at 190 K and the peak shifted to higher emission rate at 200 K, which is consistent with a real defect level peak. In Fig. 8-3 (b), the LDLTS spectra for closely spaced levels *E*(0.21) and *E*(0.20) is shown as distinct peaks. At each temperature the extracted emission rates of the two peaks differs by a factor greater than 2 and both peaks shifted to higher emission rates when temperature was increased. The level *E*(0.38) and *H*(0.30) have been assigned to the vacancy – antimony (V-Sb) center, i.e. the so called *E*-center. This is further supported by the linear dependence of defect signal on fluence for both *E*(0.38) and *H*(0.30) as shown in Fig. 8-2. The *E*-center introduces three levels with different charge state in Ge band gap. *E*(0.38) is the double acceptor charge state (--/-) and *H*(0.30) is the single acceptor charge state (0/-) of the *E*-center [2-6]. The electron traps *E*(0.15), *E*(0.20), *E*(0.21), *E*(0.23) and

E(0.31) have not been identified, but only speculations that they are Sb and/or interstitial (I) related have been reported.

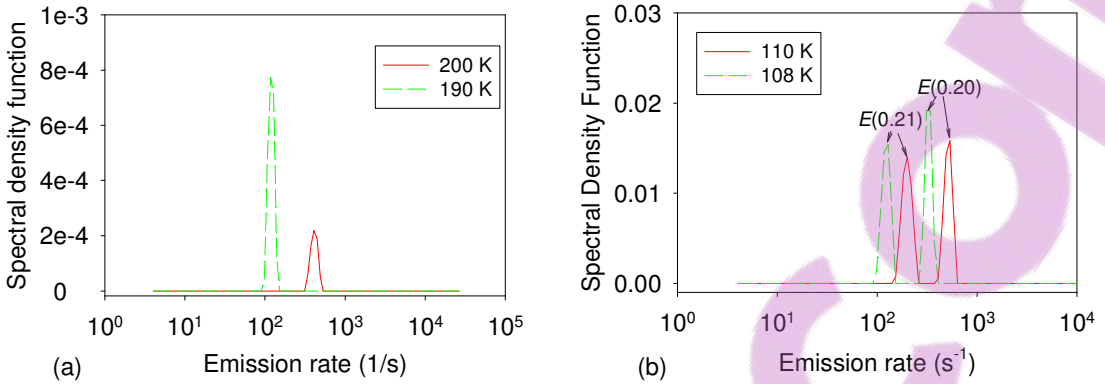

Fig. 8-3. LDLTS spectra for (a) E(0.38) as recorded at 190 K (dotted curve) and 200 K (solid curve) and (b) closely spaced traps E(0.20) and E(0.21) recorded at 108 K (dotted curve) and 110 K (solid curve). The spectra were recorded at a quiescent reverse bias of -1 V, filling pulse of 0 V and pulse width of 1 ms.

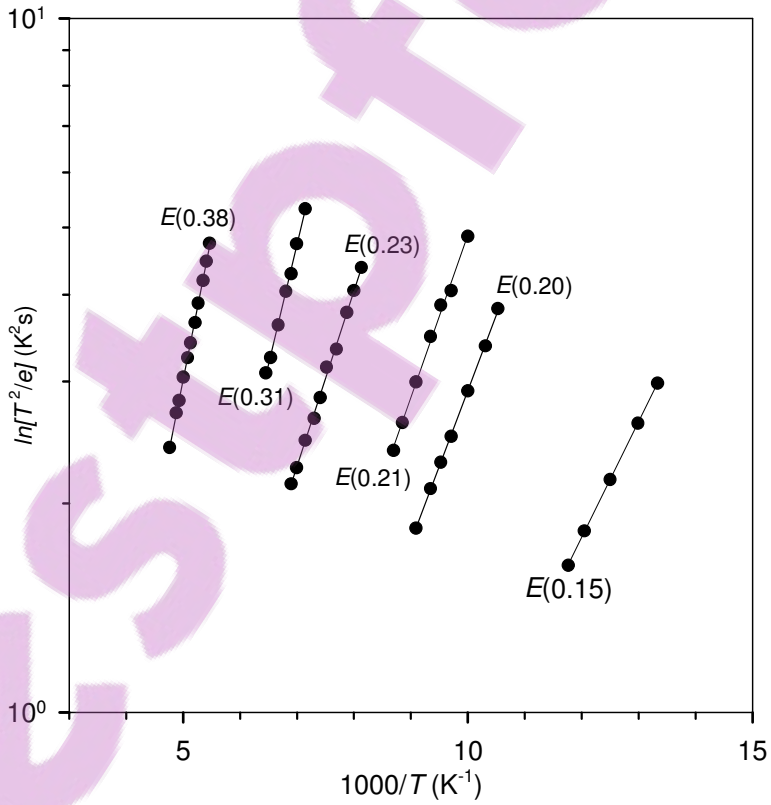

Fig. 8-4. Arrhenius plots of electron traps introduced in n-Ge after MeV electron irradiation.

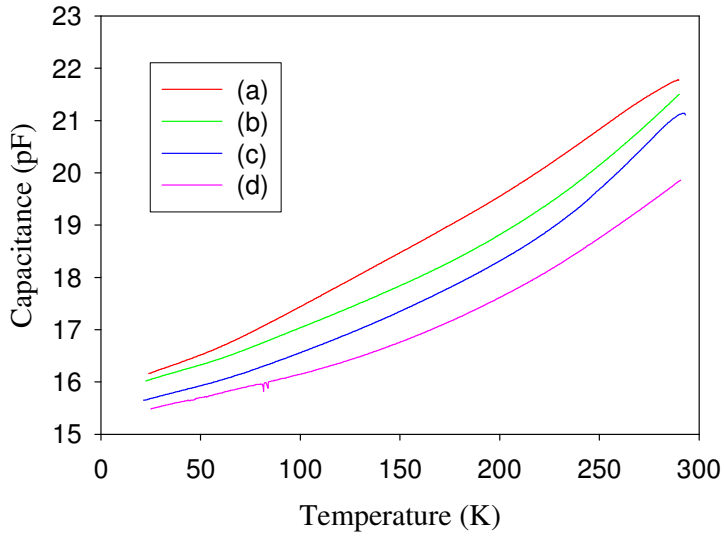

Fig. 8-5. Capacitance – temperature profiles of Ge110 for (a) as-deposited, and after irradiation with a fluence of (b) 1.4 x 10^{13} e cm^{-2}, (c) 9.2 x 10^{13} e cm^{-2} and (d) 1.7 x 10^{14} e cm^{-2} recorded at a quiescent reverse bias of -2 V.

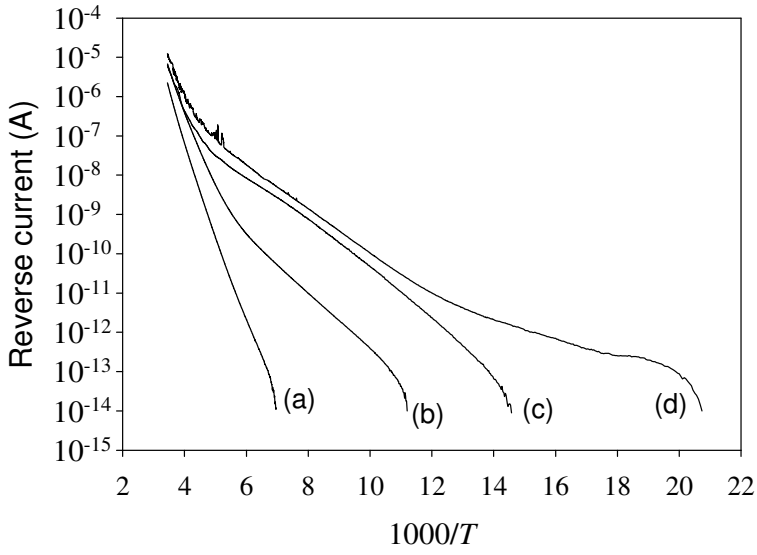

Fig. 8-6. Reverse current versus temperature profiles for Ge110 for (a) as-deposited, and after irradiation with a dose of (b) 1.4 x 10^{13} e cm^{-2}, (c) 9.2 x 10^{13} e cm^{-2} and (d) 1.7 x 10^{14} e cm^{-2} measured at a quiescent reverse bias of -1 V.

The normalized peak height signals for *E*(0.15), *E*(0.20), *E*(0.21), *E*(0.23) increase linearly with fluence within experimental error, suggesting that these traps are V or I related, while the defect concentration for *E*(0.31) is nearly independent of the dose, as shown in Fig. 8-2. Defect models are needed to identify this defect levels.

The diode capacitance – temperature (*C-T*) curves at various irradiation doses, depicted in Fig. 8-5, show a general shift to lower capacitance as the dose is increased, curves (a) – (d). This shows an increase in charge carrier traps with higher dose as expected. These results correlate well with the current-temperature (*I-T*) results shown in Fig. 8-6, which depict a near ideal behavior for the as-deposited sample, curve (a) and there is a shift to higher leakage currents as trap density increases with higher irradiation doses. Apart from the defect related leakage currents, (*I-T*) curves also show that the leakage current is thermally generated, i.e. from 10^{-6} A at room temperature to 10^{-12} A at 100 K as shown in Fig. 8-6 curve (b).

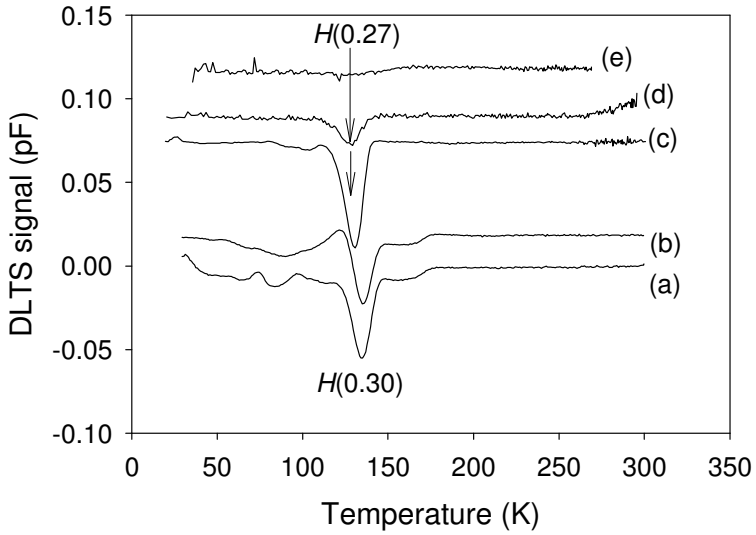

Fig. 8-7. DLTS hole traps spectra after irradiating Ge100 with electrons to a fluence of 1.7 x 10^{14} e cm^{-2} for (a) as-irradiated and after annealing at (b) 100˚C, (c) 200˚C, (d) 300˚C, and (e) 350˚C. These spectra were recorded at a rate window of 80 s^{-1} and quiescent reverse bias of -2 V with a filling pulse of 3 V and pulse width of 1 ms.

In order to extract more information on the defects in Ge, annealing studies were performed on the samples and the annealing temperatures (i.e. temperature at which a defect is removed) are summarized in Table. 8-1. *E*(0.15), *E*(0.20), *E*(0.21) and *E*(0.38), are all completely removed after annealing at 200˚C. *E*(0.31) and *E*(0.23) were removed after annealing at 125˚C and 175˚C respectively. The annealing profile of the hole traps is depicted in Fig. 8-7. A new hole trap *H*(0.27) is introduced at 200˚C as shown in the DLTS spectrum, in Fig. 8-7 curves (c) and is removed after annealing at 350˚C, as depicted by curve (e). It is interesting to note that apart from

observing the hole trap *H*(0.27) after annealing, it was also observed in the as-irradiated samples which had been stored at room temperature for more that a month. The origin of this secondary hole trap is still unclear at the moment, but Markevich *et al*, suggested that it might be a V-Sb_2 complex formed as a result of the annealing of the *E*-center [9].

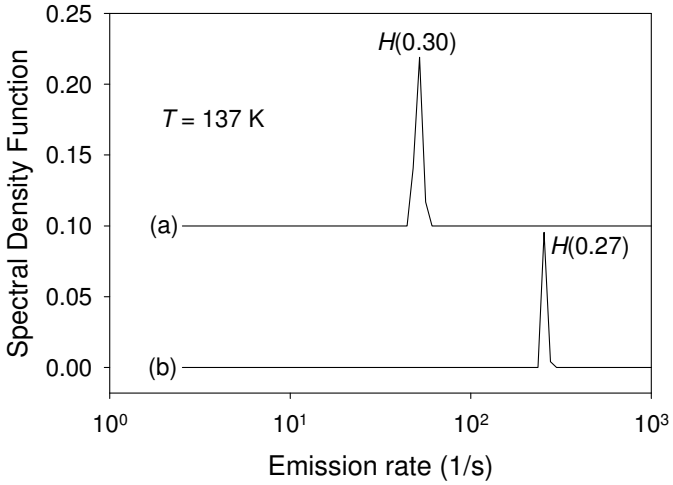

Fig. 8-8. LDLTS spectra for the hole traps H(0.27) and H(0.30) when recorded at 137 K (a) immediately after irradiation and (b) after annealing at 200˚C.

Fig. 8-8 shows the corresponding LDLTS signals for *H*(0.27) and *H*(0.30) both recorded at 137 K in as-irradiated sample (for *H*(0.30)) and in the sample annealed at 200˚C (for *H*(0.27)). The LDLTS spectra show two peaks with different emission rates, an indication that *H*(0.27) and *H*(0.30) are indeed different defect levels.

8.3.2 Dependence of electron irradiation induced defects in Ge on doping impurity density

DLTS spectra in Figs. 8-9 and 8-11 show the electron and hole traps introduced in three samples with different doping densities, respectively. As shown in Fig. 10, the defect concentration of *E*(0.38) linearly increases with doping density which confirms its assignment as V-Sb center. The concentrations of *E*(0.15), *E*(0.20) and *E*(0.21) increase with doping concentration (hence Sb-related), while *E*(0.23) and *E*(0.31) are independent of the doping concentration. A new low temperature peak *E*(0.04) is observed in the Ge110 sample. The origin of this particular defect is not clear at the moment. A summary of the electronic properties of the hole traps and a new electron

trap observed in the Ge110 samples are summarized in Table. 8.2 and the Arrhenius plots for the hole traps are depicted in Fig. 8-12.

Table 8.2. A summary of defects electronic properties introduced in n-type Ge by electron irradiation.

Defect	E_T (eV)	σ_a (cm^2)	T^a_{peak} (K)	T^b_{out} (˚C)	Defect origin
E(0.04)	$E_C - 0.04$	3.0 x 10^{-13}	30	200	I-related?
H(0.09)	$E_V + 0.09$	2.4 x 10^{-12}	47	225	$H_{0.09}$[b], V-Sb (+/0)[c]?
H(0.27)	$E_V + 0.27$	4.6 x 10^{-13}	135	325	V-Sb$_2$?
H(0.30)	$E_V + 0.30$	4.0 x 10^{-12}	142	225	V-Sb (0/-) [2-4]

[a]Peak temperature at a rate window of 80 s^{-1}, [b]see [ref. 2], [c]see [ref. 7].

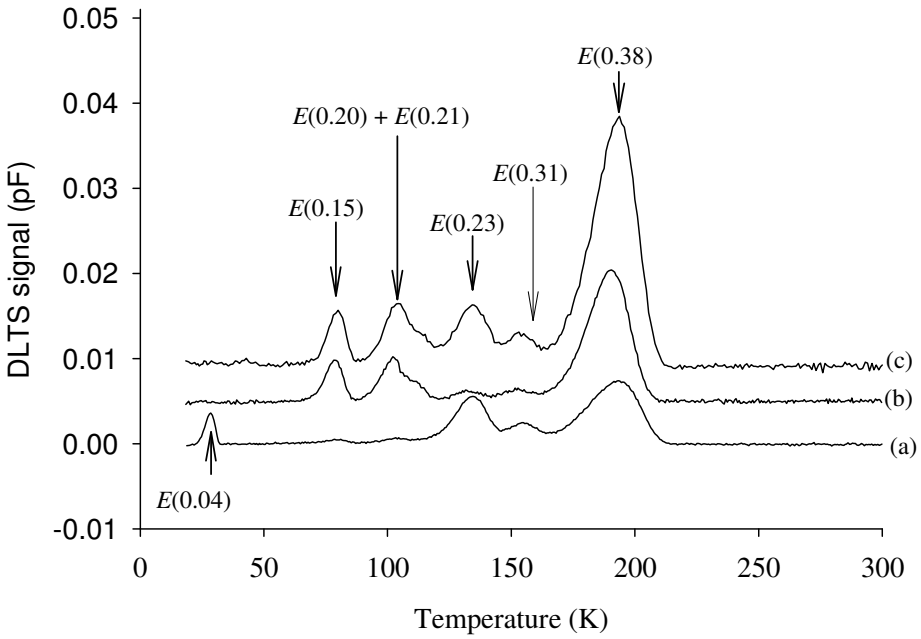

Fig. 8-9. Electron traps DLTS spectra for (a) Ge110 after a fluence of 3.7 x 10^{13} cm^{-2}, (b) Ge111 after a fluence of 9.2 x 10^{13} cm^{-2}, and (c) Ge100 after a fluence of 1.7 x 10^{14} cm^{-2}. The spectra were recorded at a quiescent reverse bias of -2 V, a filling pulse voltage of 0 V and +3 V for electron and hole traps respectively, and rate window of 80 s^{-1}.

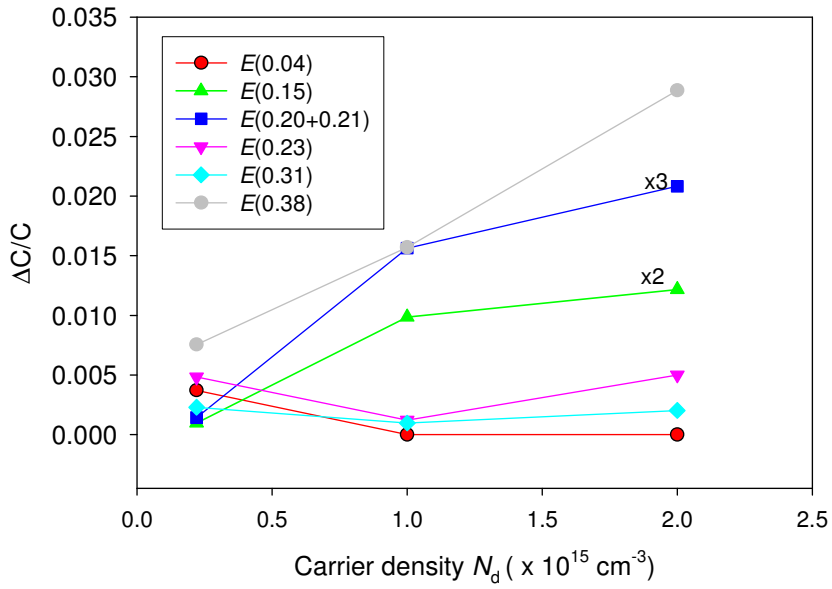

Fig. 8-10. Normalized DLTS peak height for each defect in the sample Ge100 as a function of fluence.

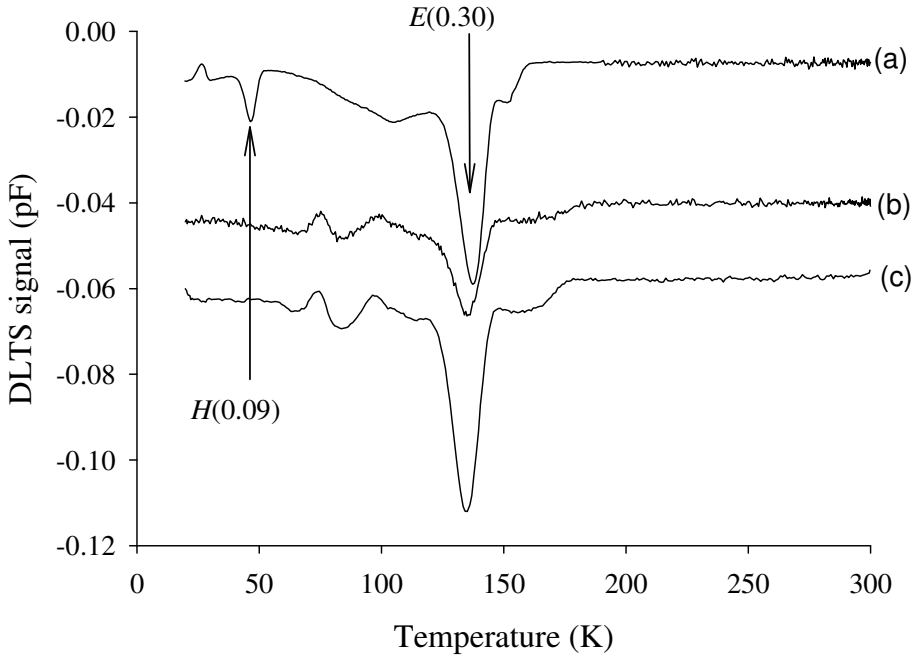

Fig. 8-11. Hole traps DLTS spectra for (a) Ge110 after a fluence of 3.7 x 10^{13} cm^{-2}, (b) Ge111 after a fluence of 9.2 x 10^{13} cm^{-2}, and (c) Ge100 after a fluence of 1.7 x 10^{14} cm^{-2}. The spectra were recorded at a quiescent reverse bias of -1 V, a filling pulse voltage of 0 V and +3 V for electron and hole traps respectively, and rate window of 80 s^{-1}.

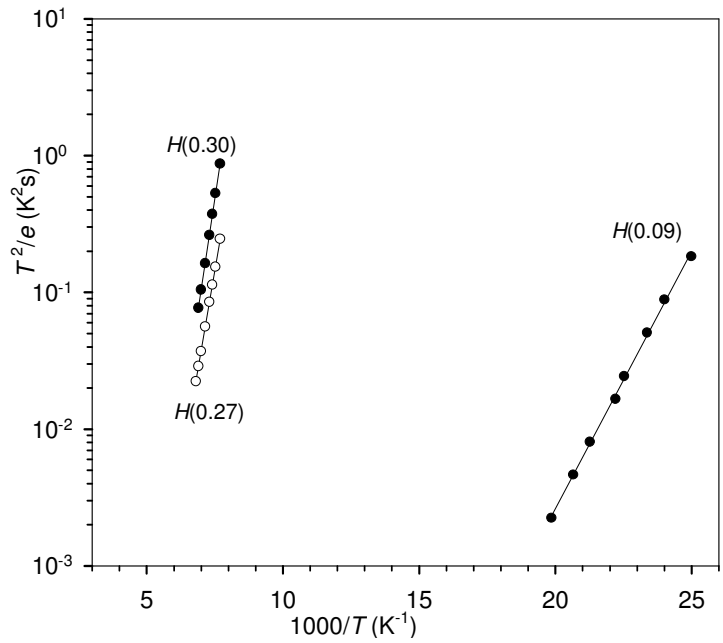

Fig. 8-12. Arrhenius plots of hole traps introduced in n-Ge after 1 MeV electron irradiation.

After annealing Ge110, the electron trap *E*(0.04) showed reverse annealing from room temperature upto 125˚C. Within the same temperature range there is a corresponding reduction in the concentration of the traps *E*(0.20), *E*(0.21), and *E*(0.31) which are probably interstitial related and this may suggest that *E*(0.04) is also interstitial related.

Defect concentration versus depth, i.e. depth profile of the *E*(0.38) measured in Ge100 is presented in Fig. 8-13. As clearly seen in the graphs, the defect concentration was generally constant with depth, which proves that the defect introduction was as result of energetic light particles such as electrons. The profiles shifted to higher concentrations as the fluence was increased as more damage was introduced into the material. The defect concentration of *E*(0.38) increased linearly with fluence upto the maximum fluence used in this study, as illustrated in Fig. 8-13 and 8-14, which can be explained by the fact that as more damage is induced into the material then there are more vacancies to combine with antimony to form the V-Sb center. The calculated introduction rate for this defect level is 1.6 x 10^1 cm^{-1}.

8.3.3 Thermal stability of defects in Ge at room temperature

The thermal stability of primary defects at room temperature has been investigated. Fage-Pedersen *et al* [4] have showed that several defects in Ge evolve at room temperature. Curves of reverse current (at -1 V) versus fluence measured after different storage times are shown in Fig. 8-15.

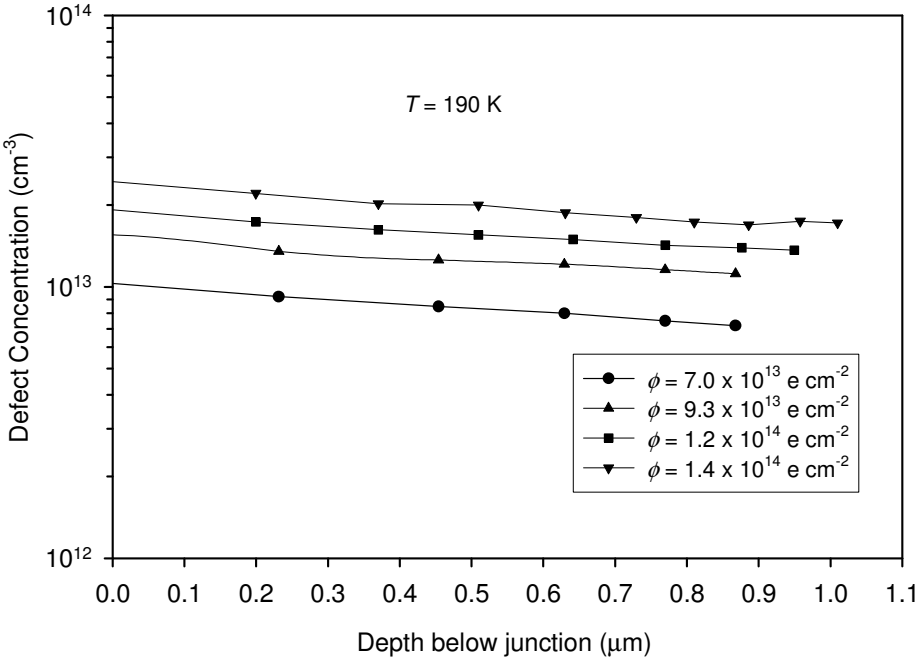

Fig. 8-13. Defect depth profile for E(0.38) as measured in Ge100 sample at fluence 7.0 x 10^{13} e cm^{-2}, 9.3 x 10^{13} e cm^{-2}, 1.2 x 10^{14} e cm^{-2}, and 1.4 x 10^{14} e cm^{-2}. The data was measured at a quiescent reverse bias of -5 V, a varying pulse voltage and pulse width of 1 ms (ref. 10).

There is a sudden decrease of reverse current after the electron irradiation. This can be attributed to an increase in the effective barrier height associated with the reduction of free carriers as a result of capturing by the introduced displacement damage. After increasing the fluence, there is a general increase in reverse current due to increase in traps which may act as generation-recombination centers, thereby increasing the leakage current. After each irradiation, the reverse current – fluence curves shifted to higher leakage current for longer storage time. This is due to increased defect concentration which evolves over time at room temperature as depicted in the DLTS spectra in Fig. 8-16.

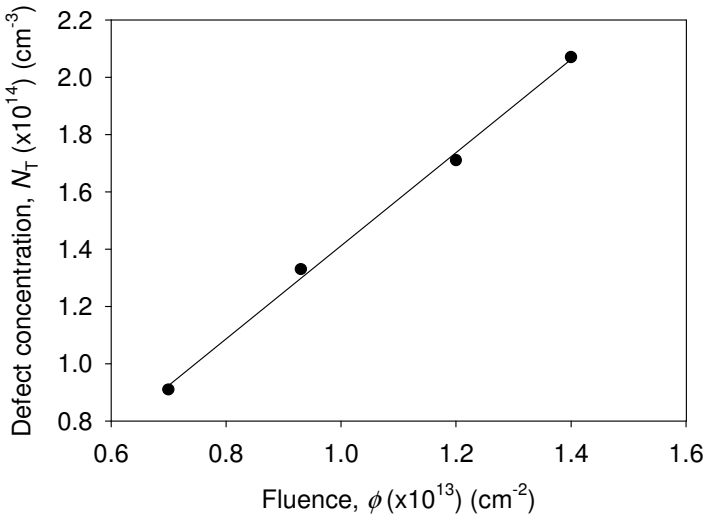

Fig. 8-14. Defect concentration of E(0.38) as a function of dose from which defect introduction rate is deduced.

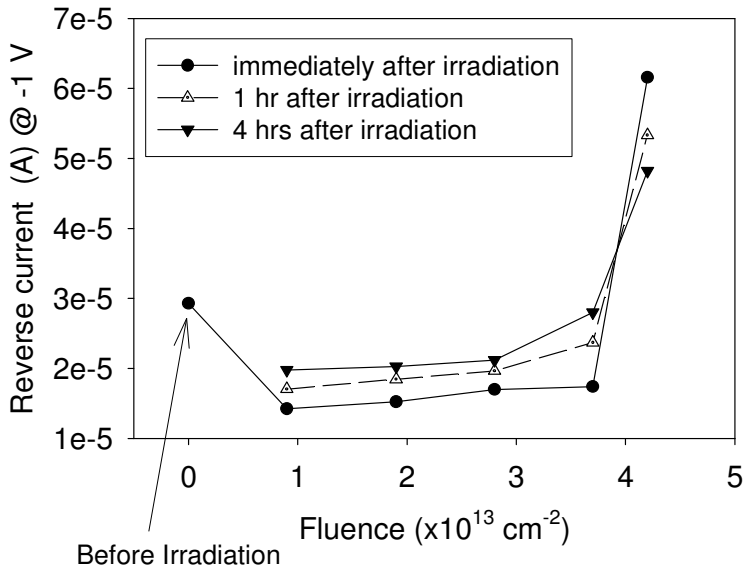

Fig. 8-15. The diode reverse current at -1 V reverse bias versus fluence, recorded immediately after irradiation, 1 hr, and 4 hrs after irradiation for Ge100.

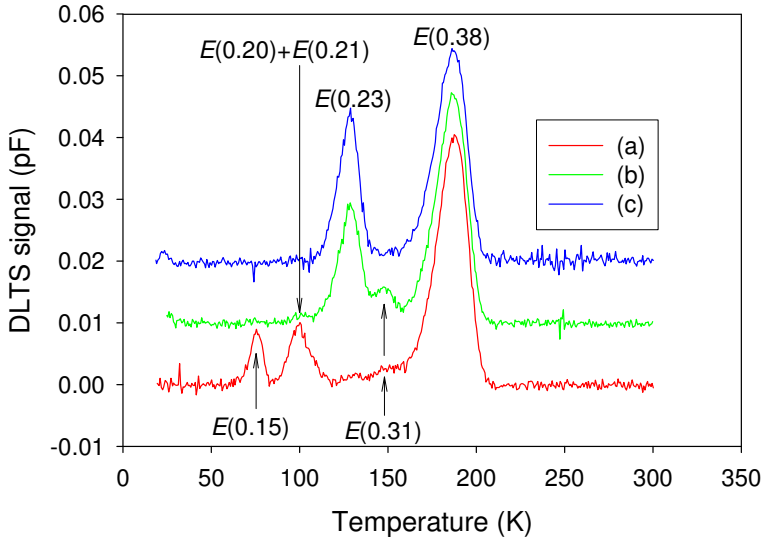

Fig. 8-16. DLTS spectra for Ge110 after electron irradiation with a fluence of 1.4 x 10^{14} e cm^{-2} when recorded, (a) immediately, (b) 2 days, and (c) 2 weeks after irradiation. The spectra were recorded at a quiescent reverse bias of -2 V, a filling pulse voltage of 0 V, and a rate window of 80 s^{-1}.

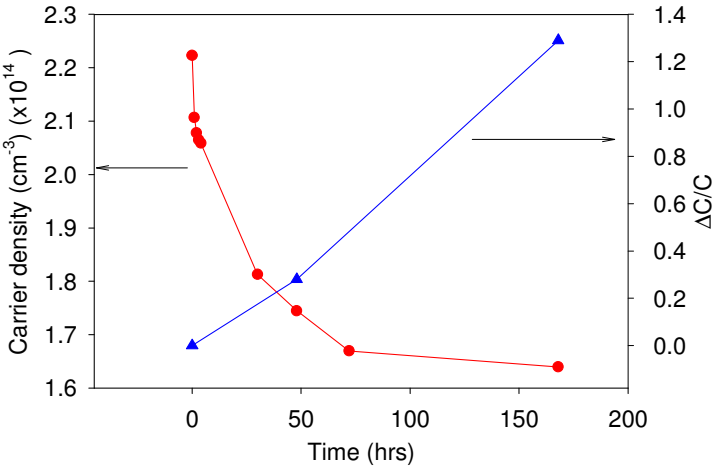

Fig. 8-17. Carrier concentration after irradiation of Ge110 with a fluence of 3.7 x 10^{13} e cm^{-2} as monitored over a period of time.

The concentration of *E*(0.31), *E*(0.23) increases significantly in the first 2 days after the irradiation, whereas there is a decrease in concentration of *E*(0.15), *E*(0.20), *E*(0.21) and *E*(0.38) in the same period. Similarly to the DLTS spectra recorded over a period of time, the free concentration shows a rapid decrease in the first day after irradiation and then the decrease slows down after 3 days and this correlates well with increase of the of *E*(0.23) which was monitored over time the same time period.

8.4 Summary and conclusions

Defects introduced in Ge doped with antimony have been characterized by DLTS and LDLTS. Electron traps *E*(0.15), *E*(0.20), *E*(0.21), *E*(0.23), *E*(0.31) and *E*(0.38), and hole traps *H*(0.09), *H*(0.27) and *H*(0.30) have been observed in electron irradiated Ge samples. Traps *E*(0.38), *H*(0.30) and *H*(0.09) have been identified as the three charge states of the V-Sb (*E*-center), namely, double acceptor (--/-), single acceptor (-/0), and single donor (0/+), respectively. Although the *ab initio* density functional theory (DFT) calculations has shown that divacancy has a single donor level at 0.08 eV and an acceptor level 0.3 eV above the valence band [11] and that the divacancy anneals at values between 150-180˚C [12], there has not been any experimental evidence of this from DLTS measurements. There are generally two ways of divacancy formation in semiconductors, i.e. (i) as a primary defect when the energy of irradiating particle is high enough or (ii) by the association of two single vacancies. The vacancy in Ge is negatively charged in a broad interval of Fermi level position in the gap [13], therefore the later mechanism of divacancy formation in Ge is suppressed because of coulombic repulsion of vacancies. Assuming direct divacancy formation then it means the complex is very unstable at room temperature and it will quickly dissociate. Kolkovsky *et al* [14] proposed that absence of a divacancy is due to the divacancy recombining with the self- interstitials rather than by dissociation.

It has been shown that after electron irradiation, some of the defects created evolve and only become fairly stable after at least 7 days of room storage. The *E*(0.23) peak height was observed to increase significantly a day after irradiation. Upon annealing, it has been observed that all defects in Ge are removed after a low thermal budget (350 - 400˚C) when compared to defects in Si. A new hole trap has been observed after annealing at 200˚C or after room temperature storage for a month. The identity of this new hole trap is currently subject to speculation.

The depth profile of the *E*(0.38) showed a uniform defect concentration with depth. This proves that high energy electrons introduces well spaced vacancies and interstitial and hence form stable complexes which are uniform with depth. The calculated introduction rate for the trap *E*(0.38) is 1.6×10^{1} cm^{-1} which is consistent with electron irradiation induced defects.

References

[1] Germanium Silicon, Phyiscs and Materials, Semiconductor and Semi-metals Vol. 56, edited by Hull and J. C. Bean (Academic, San Diego, 1999).

[2] F.D. Auret, W.E. Meyer, S. Coelho and M. Hayes, *Appl. Phys. Lett*. **88**, 242110 (2006).

[3] F.D. Auret, P.J. Janse van Rensburg, M. Hayes, J.M. Nel, W.E. Meyer, S. Decoster, V. Matias and A. Vantomme, *Appl. Phys. Lett*. **89**, 152123 (2006).

[4] J. Fage-Pedersen, A. Nylandsted Larsen and A. Mesli, *Phys. Rev. B*. **62**, 10116 (2000).

[5] V.P. Makervich, I.D. Hawkins, A.R. Peaker, K.V. Emstev, V.V. Emstev, V.V. Litvinov and L. Dobaczewski, *Phys. Rev. B*. **70**, 235213 (2004).

[6] V.P. Makervich, A.R. Peaker, V.V. Litvinov, V.V. Emstev and L.I. Murin, *J. Appl. Phys.* **95**, 4078 (2004).

[7] C.E. Lindberg, J. Lundsgaard Hansen, P. Bomholt, A. Mesli, K. Bonde Nielsen and A. Nylandsted Larsen, *Appl. Phys. Lett*. **87**, 172103 (2005).

[8] A.R. Peaker, V.P. Markevich, L.I. Murin, N.V. Abrosimov and V.V. Litvinov, *Mater. Sci. Eng*. **B 124** (2005) 166.

[9] V. P. Markevich, *Mater. Sci. in Semicond. Process*. **9** (2006) 589.

[10] Y. Zohta and M.O. Watanabe, *J. Appl. Phys*. **53** No.**3** (1982) 1809.

[11] J. Coutinho, R. Jones, V.J.B. Torres, M. Barroso, S. Oberg and P.R. Briddon, *Appl. Phys. Lett*. **88** (2006) 095208.

[12] H.J. Stein, '*Divacancy-like absorption in ion-bombarded Ge',* In: Radiation damage and defects in Semiconductors. London, London Institute of Physics: 1973.

[13] H. Haesslein, R. Sielemann and C. Zistl, *Phys. Rev. Lett*. **80** (1998) 2626.

[14] V.L. Kolkovsky, M. Christian Petersen, A. Nylandsted Larsen and A. Mesli, *Mater. Sci. in Semicond. Process*., (2008), doi: 10.1016/j.mssp.2008.07.006.

List of Publications

1. Cloud Nyamhere, M. Das, F.D. Auret and A. Chawanda, "*A Study of electron induced defects in n-type germanium by Deep Level Transient Spectroscopy (DLTS)",* Phys. Stat. Sol. (c) vol. 5, No. 2**,** (2008), 623 – 625.
2. C. Nyamhere, F.D. Auret, A.G.M. Das and A. Chawanda, "*A study of the dependence of electron-induced defects on the doping impurity density in n-type germanium by deep-level transient spectroscopy (DLTS)*", Physica B; Vols 401- 402 (2007) 499-502.

Chapter 9

Defects introduced in antimony-doped germanium during metallization by electron beam deposition

9.1 Introduction

To completely characterize defects in semiconductors materials, defects introduced by light and heavy particles should be investigated. Unlike high energy electrons which introduce well spaced vacancies and interstitial distributed evenly throughout the sample, which then diffuse to form simple stable defects at room temperature, heavy particles introduce densely populated vacancy-rich and interstitial rich regions with the interstitials concentrated at the near-end regions of the ion range, leading to complex defect formation [1]. Heavy ions (ions larger than protons or electrons) are usually associated with defects introduced into semiconductor substrate during metallization by sputter deposition or electron beam deposition and during doping by ion implantation. The ions usually associated with damage during electron beam deposition are the residual vacuum gasses (such as C, N, O, H) which are ionized and then accelerated by the electric and magnetic fields in the chamber. Although there is some literature on the defects introduced during implantation [2,3], sputter deposition [4,5] and electron beam deposition [6,7] there is still lack of clear understanding of the origin and identity of some of the defects introduced by these heavy ions.

Metallization is a critical device processing step in the semiconductor industry. Resistive evaporation, electron beam deposition, and sputter deposition are commonly used metallization techniques. In this study defects introduced in n-type Ge during electron beam deposition (EBD) of different metal contacts are presented. EBD induced defects can influence device performance and alter barrier heights of the contacts. To shed more light on the origin and structure of these defects, annealing

studies were also performed. The annealing mechanism of the *E*-center is presented from which the activation energy of the annealing process is deduced.

9.2 Experimental Procedure

The samples used for this work were n-type, bulk grown Ge (111) doped with Sb to about 2.5 x 10^{15} cm^{-3} and were supplied by Umicore. Before metallization the samples of 5 mm x 3 mm in size were first degreased and then etched in a mixture of H_2O_2 (30%) : H_2O (1:5) for 1 minute. Immediately after cleaning they were inserted into a vacuum chamber where AuSb (0.6% Sb) was deposited by, resistive evaporation, on their back surfaces as ohmic contacts. The samples were then annealed at 350 ˚C in argon (Ar) for 10 minutes to minimize the contact resistivity of the ohmic contacts. Before the Schottky contact fabrication, the cleaning procedure above was repeated. Au, Ru, Pt, Ru/Au or Pt/Au contacts, 0.60 mm in diameter and 200 nm thick each were deposited by electron beam deposition. For a control sample, Au was deposited as the Schottky contact using resistive deposition. After the contact fabrication, the diodes were characterized by current – voltage (*I-V*) and capacitance – voltage (*C-V*) measurements at room temperature to determine the quality of the diodes. Defects introduced by the deposition technique were characterized by deep level transient spectroscopy (DLTS) and Laplace – DLTS (LDLTS). The '*signatures*' of radiation induced defects (i.e. activation enthalpy for the electron traps and hole traps, E_T, and apparent capture cross section, σ_a), were determined from Arrhenius plots of $ln(T^2/e)$ vs. $1000/T$, where 'e' is either the hole or electron emission rate, and T is the measurement temperature.

In order to investigate the defect annealing behaviour, the samples were annealed isochronally for 20 minutes in Ar gas from room temperature up to 500˚C.

9.3 Published and other Results

In this section the electronic and annealing properties of defects introduced in n-type Ge by electron beam deposition are presented. The annealing behavior of these defects is investigated, with emphasis on the *E*-center (V-Sb). The annealing mechanism and activation energy of the annealing process of the *E*-center is also deduced.

9.3.1 Defects introduced by electron beam deposition in n-type Ge

A comprehensive discussion of defects introduced during metallization using electron beam deposition is presented in the publication at the end of section 9.3.2. A comparison has been made to defects introduced during sputter deposition and electron irradiation of similar samples.

- F.D. Auret, S.M.M. Coehlo, P.J. Janse van Rensberg, C. Nyamhere, W.E. Meyer, Mater. Sci. in Semiconductor Processing (2008) doi:10.1016/j.mssp.2008.09.001.

In addition to the results presented in the publication, other results are also presented in this section.

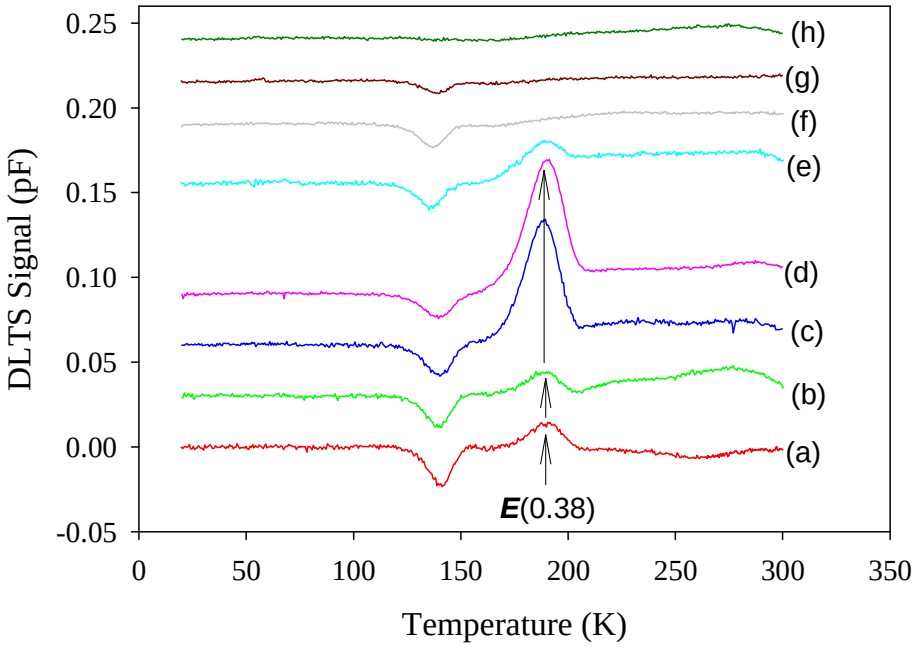

Fig. 9-1. DLTS spectra for electron traps induced in Ge after electron beam deposition of Ru/Au Schottky contacts. The spectra were recorded (a) for as-deposited, and after annealing at (b) 100˚C, (c) 150˚C, (d) 175˚C, (e) 200˚C, (f) 225˚C, (g) 250˚C, (h) 300˚C and (i) 350˚C. These spectra were recorded with a quiescent reverse bias of -2 V, a rate window of 80 s^{-1}, a pulse voltage of -0.15 V and pulse width of 1 ms.

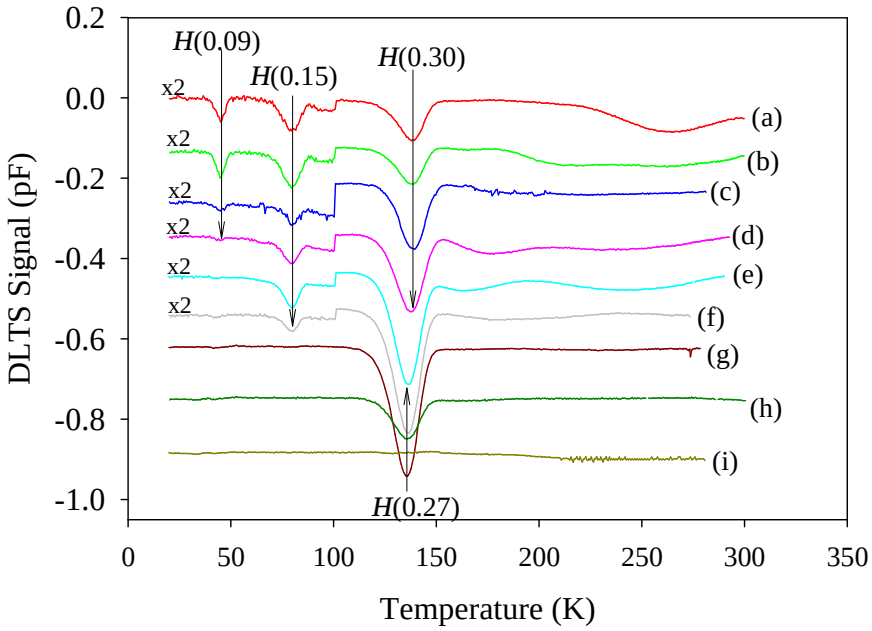

Fig. 9-2. DLTS spectra for hole traps induced in Ge after electron beam deposition of Ru/Au Schottky contacts. The spectra were recorded (a) for as-deposited, and after annealing at (b) 100˚C, (c) 150˚C, (d) 175˚C, (e) 200˚C, (f) 225˚C, (g) 250˚C, (h) 300˚C and (i) 350˚C. These spectra were recorded with a quiescent reverse bias of -1 V, a rate window of 80 s^{-1}, a pulse voltage of +3 V and pulse width of 1 ms.

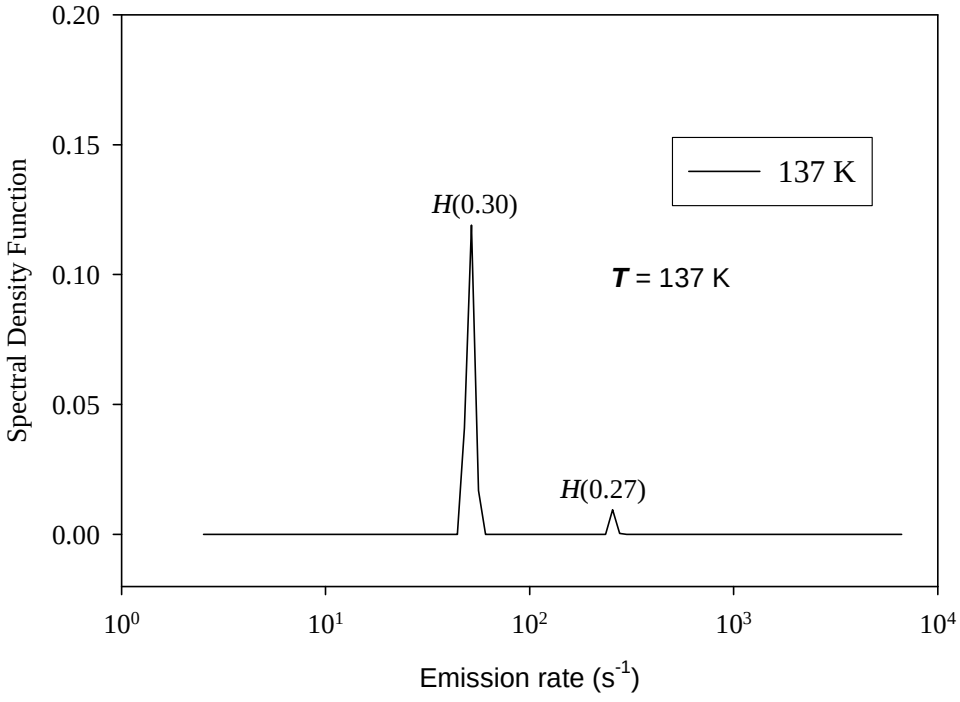

Fig. 9-3. LDLTS spectra for H(0.27) and H(0.30) in as-deposited sample recorded at 137 K.

Figs. 9-1, 9-2 and 9-3 summarize the primary defects introduced by electron beam deposition and their annealing behavior. *E*(0.38) level is the only detectable electron trap after Ru/Au Schottky contacts fabrication. This can be attributed to the heavy injection of minority carriers into the band gap even without applying a minority carrier filling pulse. The high barrier height formed between the Ru/Au and germanium give rise to an inversion layer close to the semiconductor surface, which is the source of these minority carriers during the application of a filling pulse. It should be noted that unlike in MeV electron irradiated samples, where the hole trap *H*(0.27) is introduced after annealing at 200˚C or after room storage for a month, but in the case of damage introduced by EBD, this hole trap is observed immediately after the deposition. This is explained by the fact that during EBD deposition the substrate temperature is higher than the room temperature and thus thermally introducing the trap *H*(0.27). The hole traps *H*(0.09) and *H*(0.15) were also observed after EBD is the (+/0) charge state of the *E*-center. The measurement of *H*(0.27) in the presence of *H*(0.30) was made possible by LDLTS which could clearly separate the signals as shown in Fig. 9-3. The signal of *H*(0.30) is much larger than that of *H*(0.27), hence a much larger concentration of *H*(0.30) in the as-deposited samples. The concentration of *H*(0.27) increases with annealing temperature until it reaches a maximum at around 225˚C at which point the *E*-center is completely removed. This reinforces the theory given in the chapter 8 that *H*(0.27) is a product of V-Sb after annealing to form new V-Sb_2 complex which is electrically active [8-9]. Although all defects were completely removed at 350˚C, the annealing studies were performed up to 600˚C to determine if there are any other defect levels that might be reactivated after presumably being transformed into electrical inactivate complexes during thermal annealing but no other defects were observed above 350˚C annealing temperature.

9.3.2 Annealing mechanism of *E*(0.38), the *E*-center

Since the *E*-center is a very important defect in Ge, for its role in (i) dopant deactivation, and free carrier removal (each V-Sb complex formation results in removal of three free carriers [10]), it is important to establish its annealing mechanism. The concentration versus depth profile of the *E*-center, measured at isochronal annealing temperatures between 25˚C – 175˚C is depicted in Fig. 9-4. The depth profile for the as-deposited sample shows that the concentration decreased from the surface of the semiconductor, which is typical of defects induced by heavy ions.

Upon annealing from 100˚C up to 175˚C for 20 minutes intervals, the trap showed some reverse annealing (i.e. increase in concentration with increase in annealing temperature) an indication that within this annealing temperature interval there is some unstable defect complex with vacancies as one of its constituency which dissociates and become the source of vacancy for the V-Sb center. Isochronal annealing at 175˚C showed a broadened profile which shifted to lower concentrations with prolonged annealing time as depicted in Fig. 9-2, suggesting diffusion of the *E*-center during the annealing process.

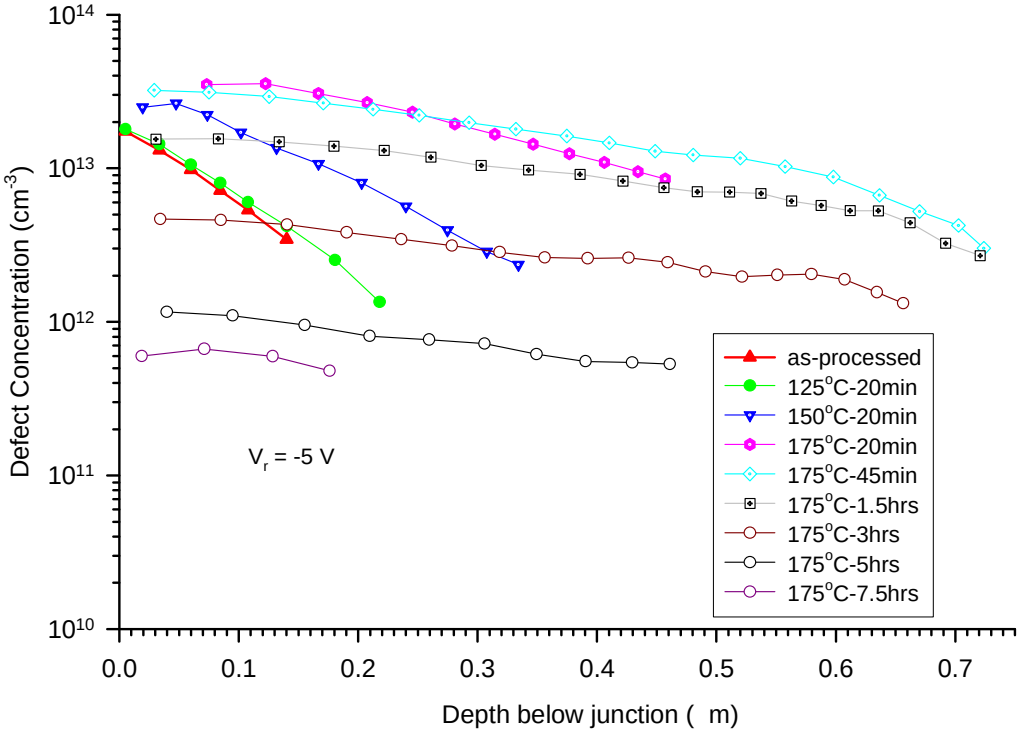

Fig. 9-4. Depth profile for E(0.38) recorded after annealing at different temperatures and for different period of time. The measurements were performed by LDLTS at fixed measurement temperature of 195 K, using fixed bias-variable pulse method with transition region correction [ref. 11].

Regions where vacancies are created in germanium by some of the residual vacuum gas ions (assuming a maximum energy of 10 keV for ions in the deposition chamber) are shown in the TRIM (version 2006.02) [12] simulation profiles in Fig. 9-5 (a-d). For an energy of 10 keV, the projected ion range is ~25 *n*m for C, N and O, each ion producing approximately 4 vacancies/nm, while H ions will create primary damage up

to a depth of ~100 *n*m and each ion producing ~10 x 10^{-3} vacancies/*n*m below the semiconductor surface.

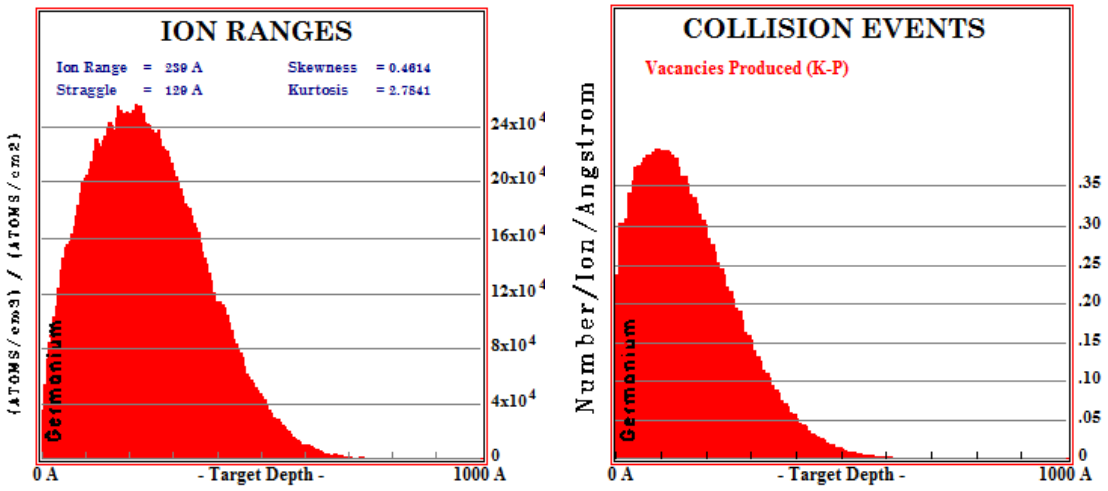

(i) (ii)

Fig. 9-5(a). (i) TRIM simulation for the projected ion range and (ii) damage events of 10 keV nitrogen ions in germanium.

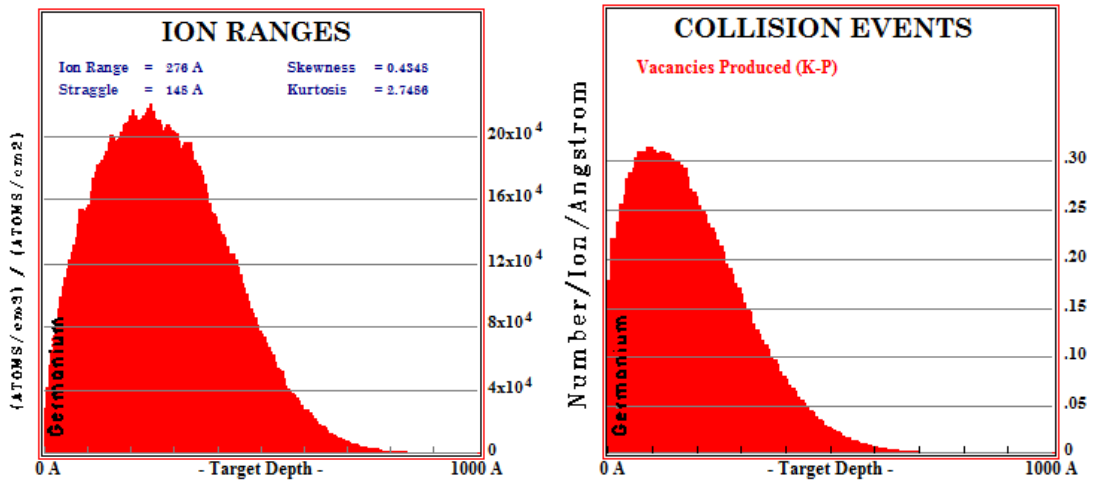

(i) (ii)

Fig. 9-5(b). (i) TRIM simulation for the projected ion range and (ii) damage events of 10 keV carbon ions in germanium.

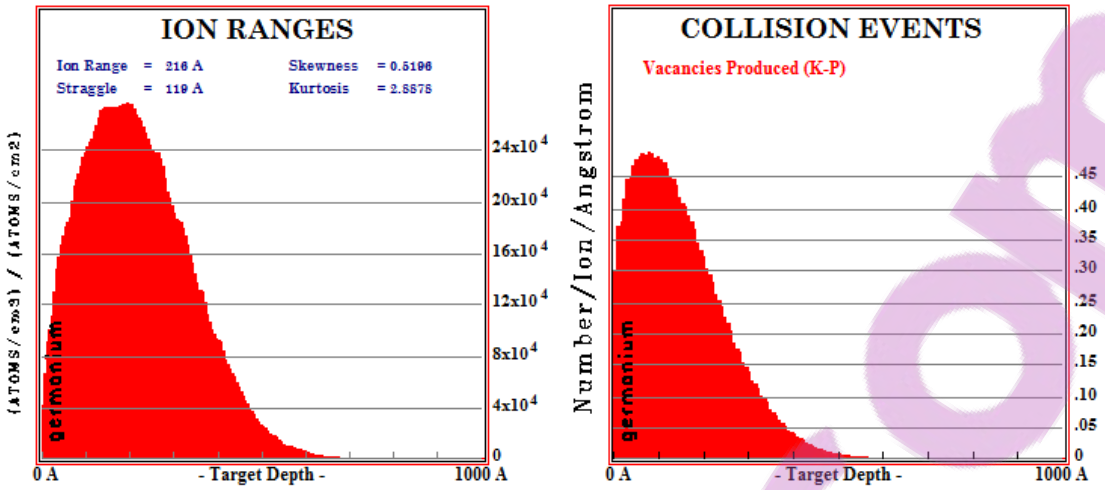

(i) (ii)

Fig. 9-5(c). (i) TRIM simulation for the projected ion range and (ii) damage events of 10 keV oxygen ions in germanium.

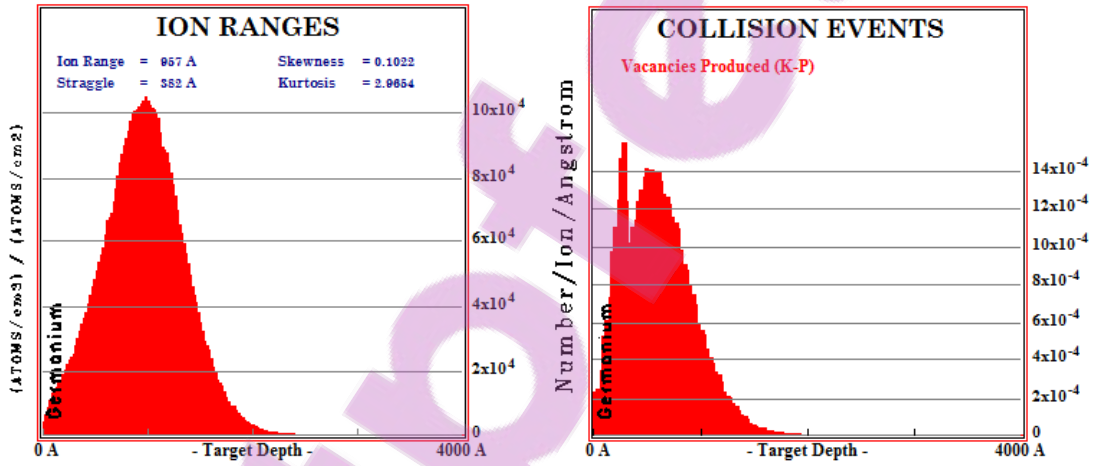

(i) (ii)

Fig. 9-5(d). (i) TRIM simulation for the projected ion range and (ii) damage events of 10 keV hydrogen ions in germanium.

This suggests that the formation of vacancy- or interstitial-related clusters is very much possible. The interstitial and vacancies created will then diffuse and form stable defect complexes (e.g. *E*-center) even deeper than the projected ion range. Thus, explaining the defect concentration profiles beyond the ion range as shown in Fig. 9-4.

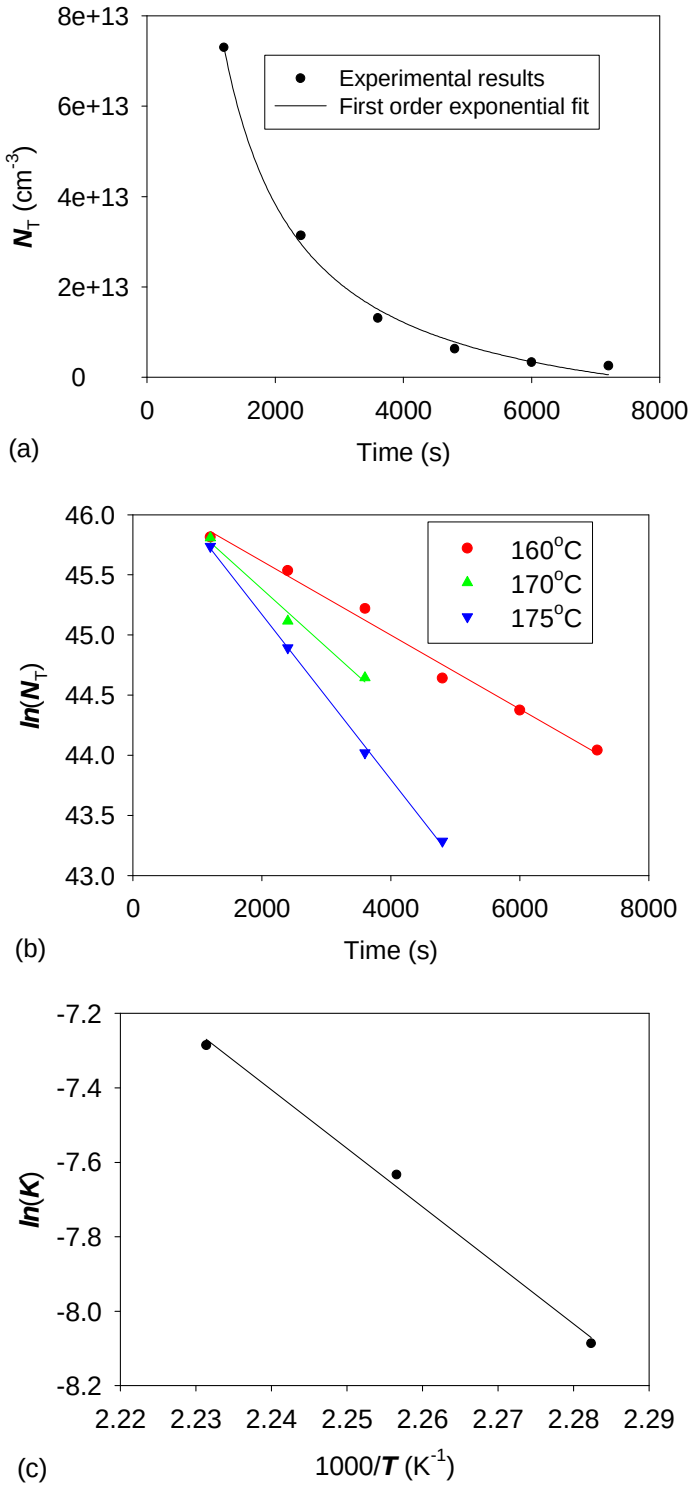

Fig. 9-6. (a) Defect concentration versus annealing time measured at annealing temperature of 175˚C. The solid line represents first order exponential decay fit. (b) Semi-log plot of defect concentration profile versus annealing time measured at annealing temperatures of 160˚C, 170˚C and 175˚C from which the annealing rate constant, K, is calculated. (c) The Arrhenius plot of log (K) vs. 1000/T.

To enhance the understanding of the annealing mechanism of the *E*-center it is important to investigate the annealing kinetics of the defect and determine the activation energy for the annealing process. The results for the annealing kinetics at temperatures 160˚C, 170˚C and 175˚C are shown in Fig. 9-6 (b) from which the annealing rate (*K*) for each temperature (*T* in ˚C) was extracted and used for the construction of the Arrhenius plots depicted in graph (c). The annealing of the *E*-center follows a first order exponential decay process as shown in Fig. 9-6 (a) and (b), with an activation energy,

$$E_a = 1.36 \text{ eV}$$

and pre-exponential factor,

$$A = (1.2 \pm 0.3) \times 10^{12} \text{ s}^{-1}$$

extracted from the gradient and vertical axis intercept of the Arrhenius plot shown in Fig. 9-6(c) respectively. The value of pre-exponential factor *A*, lies just below the lower end of the purely dissociation range of $>10^{12}$ s^{-1} [13,14]. The value of the pre-exponential factor obtained points more to a diffusion driven annealing mechanism of the *E*-center in Ge. The annealing of the *E*-center has been associated with the introduction of the hole trap *H*(0.27) which has been attributed to higher order complex Sb_2V [15]. This has been further supported by theoretical studies by Coutinho *et al* [16], who predicted that the complex Sb_2V is an electrical active level which is close the position of V-Sb (-/0). It then follows that the *E*-center anneals by diffusing until it captures an Sb atom in the substitutional position and its structure changes to Sb_2V.

Materials Science in Semiconductor Processing ▮ (▮▮▮▮) ▮▮▮–▮▮▮

Contents lists available at ScienceDirect

Materials Science in Semiconductor Processing

journal homepage: www.elsevier.com/locate/mssp

Electrical characterization of defects introduced during metallization processes in n-type germanium

F.D. Auret *, S.M.M. Coelho, P.J. Janse van Rensburg, C. Nyamhere, W.E. Meyer

Physics Department, University of Pretoria, Pretoria 0002, South Africa

ARTICLE INFO

Keywords:
Ge
Metallization
Defects
Deep-level transient spectroscopy
DLTS

ABSTRACT

We have studied the defects introduced in n-type Ge during electron beam deposition (EBD) and sputter deposition (SD) by deep-level transient spectroscopy (DLTS) and evaluated their influence on the rectification quality of Schottky contacts by current–voltage (I–V) measurements. I–V measurements demonstrated that the quality of sputter-deposited diodes are poorer than those of diodes formed by EBD. The highest quality Schottky diodes were formed by resistive evaporation that introduced no defects in Ge. In the case of EBD of metals the main defect introduced during metallization was the V–Sb complex, also introduced during by electron irradiation. The concentrations of the EBD-induced defects depend on the metal used: metals that required a higher electron beam intensity to evaporate, e.g. Ru, resulted in larger defect concentrations than metals requiring lower electron beam intensity, e.g. Au. All the EBD-induced defects can be removed by annealing at temperatures above 325 °C. Sputter deposition introduces several electrically active defects near the surface of Ge. All these defects have also been observed after high-energy electron irradiation. However, the V–Sb centre introduced by EBD was not observed after sputter deposition. Annealing at 250 °C in Ar removed all the defects introduced during sputter deposition.

1. Introduction

The low effective mass of holes in Ge has opened up the possibility of using Ge in ultrafast complimentary metal-oxide-semiconductor (CMOS) devices [1]. This, in turn, has triggered renewed interest in the properties of defects in Ge because defects ultimately determine the performance of devices. In a detailed study of proton and electron-irradiated Ge a comparison was made to previously observed radiation-induced defects and level assignments of the E-centre (V–Sb), A-centre (V–O) and divacancy (V–V) were proposed [2]. Several other O- and Sb-related defects were characterised in O-doped and Sb-doped Ge, respectively. It was also convincingly demonstrated that the E-centre in Sb-doped Ge can be present in three charge states and the level positions associated with these levels' states were determined [3–5].

Metallization is a critical processing step in the semiconductor industry. Resistive evaporation, electron beam deposition (EBD) and sputter deposition are commonly used metallization methods. It is well known that resistive evaporation does not introduce any detectable defects in the semiconductor. However, it cannot easily deposit high melting point materials e.g. W or Ru. EBD, on the other hand, is useful to deposit high melting point metals at very controllable rates. Sputter deposition can also be used to deposit high melting point metals and is further capable of stoichiometrically depositing alloys from compound targets. Unfortunately, these latter two methods introduce defects in semiconductors. Some investigations regarding the defects introduced in Ge during EBD [6–8] and sputter deposition [9,10] have been reported. The defects introduced during these processes reside in the Ge at and close to the metal–Ge junction;

* Corresponding author. Tel.: +27 12 420 2684; fax: +27 12 362 5288.
E-mail address: danie.auret@up.ac.za (F.D. Auret).

1369-8001/$ - see front matter © 2008 Elsevier Ltd. All rights reserved.
doi:10.1016/j.mssp.2008.09.001

they influence device performance and alter the barrier heights of the contacts [11]. The defects responsible for these barrier adjustments are formed when energetic particles reach the semiconductor surface and interact with the semiconductor. Depending on the application, these defects may either be beneficial or detrimental to optimum device functioning. For Si it has been shown that the defects introduced during high-energy electron and proton irradiation increase the switching speed of devices [12].

In this study, we review the electronic properties of defects introduced in n-type Ge during EBD and sputter deposition of different metal Schottky contacts. We also show that the concentrations of the most prominent EBD-induced defect, the V–Sb centre, depended on the metal deposited by EBD via the melting point of the metal and the influence thereof on the vacuum during metallization. We have found that sputter deposition also introduces several electrically active defects near the surface of Ge, but, contrary to what has been reported elsewhere [9], it did not introduce the V–Sb centre in our experiments. Most of the defects introduced by EBD and sputter deposition have also been observed after high-energy electron irradiation. We also illustrate the effect of these process-induced defects on the current–voltage (I–V) characteristics of the Schottky diodes at different temperatures. Finally, we compare the removal of these metallization-induced defects by thermal annealing.

2. Experimental procedure

The Schottky barrier diodes for this study were fabricated on bulk-grown (111) n-type Ge doped with Sb to a level of $2.5 \times 10^{15}\,cm^{-3}$. Before metallization the samples were first degreased and then etched in a mixture of H_2O_2:H_2O (1:5) for 1 min. Directly after cleaning they were inserted into a vacuum chamber where AuSb (0.6% Sb) was deposited on their back surfaces. The samples were then annealed at 350 °C in Ar for 10 min, yielding ohmic contacts with a low contact resistivity. Before Schottky contact deposition, the samples were again chemically cleaned as described above. Metal (Au, Ti and Ru) contacts, 0.6 mm in diameter and 200 nm thick, were deposited onto the Ge in an EBD system through a mechanical mask. A Varian 10 kV electron gun vacuum evaporation system was used for this process. In this system, the samples are positioned about 0.4 m above the electron gun. In a different system Au Schottky contacts were sputter deposited onto similar Ge samples cut from the same wafer. For sputter deposition Ar was leaked into the system to a pressure of 6×10^{-2} mbar [9]. The sputter-deposited contacts were deposited at a rate of about $2\,nm\,s^{-1}$ and were 400 nm thick. "Control" Au Schottky contacts were deposited on samples cut from the same wafer by resistive evaporation.

Following contact fabrication, current–voltage (I–V) and capacitance–voltage (C–V) measurements were performed to assess the quality of the diodes and to determine the free carrier density of the Ge, respectively. Thereafter both conventional and high-resolution Laplace deep-level transient spectroscopy (DLTS) [13,14] was used to study the defects introduced in the Ge during the EBD and SD processes. The activation energies, E_T, and apparent capture cross sections for electrons, σ_{na}, and holes, σ_{pa}, (i.e. the DLTS "signatures") of the process-induced electron traps were determined from the conventional DLTS Arrhenius plots. In order to identify the defects introduced by the deposition processes, a comparison was made with defects introduced by high-energy (MeV) electron irradiation from a Sr^{90} source in samples cut from the same wafer.

3. Results and discussion

3.1. I–V characteristics of Schottky diodes fabricated by EBD and sputter deposition

I–V measurements were recorded at room temperature as well as at several other lower temperatures. The series resistances of the control diodes remained in the 10–20 Ω range in the entire temperature regime investigated, indicating that the AuSb back contacts retained their ohmic character, even down to 16 K, the lowest temperature attainable in our cryostat. Room temperature C–V measurements yielded the free carrier density of the Ge as $(2.5 \pm 0.05) \times 10^{15}\,cm^{-3}$. In Fig. 1, we compare the forward and reverse I–V characteristics of Au Schottky contacts formed by resistive evaporation, EBD and sputter deposition at room temperature and at 100 K. We chose 100 K as

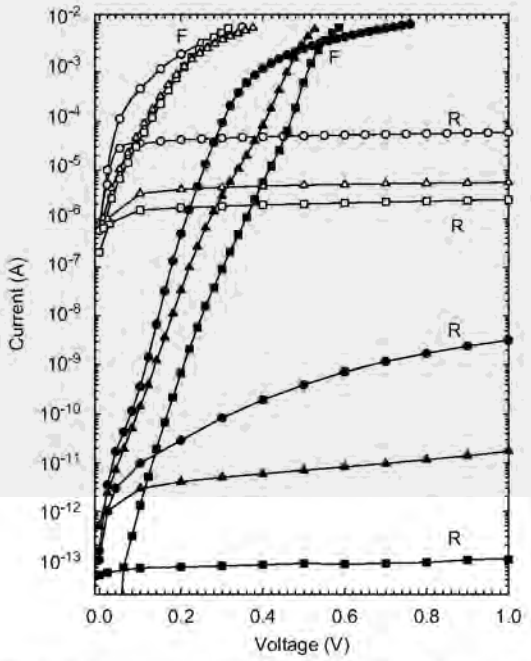

Fig. 1. I–V characteristics of Au Schottky contacts to n-Ge deposited by resistive evaporation (squares), EBD (triangles) and sputter deposition (circles). Open symbols are the data recorded at room temperature while filled symbols represent the data recorded at 100 K.

the lower temperature because at 100 K the reverse leakage current of the best diodes (deposited by resistive evaporation) is between 10^{-13} and 10^{-14} A, which is the lowest current our equipment can accurately measure. At room temperature the *I–V* barrier height of these three contacts were determined as (0.59±0.01), (0.56±0.01) and (0.53±0.01) eV, respectively.

From Fig. 1 we notice several interesting aspects. Firstly, at room temperature, the reverse leakage current of the control diodes are the best whereas that of the sputtered diodes are the poorest, by slightly more than a decade. Secondly, if we compare the characteristics of these diodes at 100 K then we see that the difference between the reverse characteristics of the three diodes has been amplified. The reverse current (at −1 V) of the sputter-deposited diode is more than four orders of magnitude higher than that of the control sample. The forward current characteristic of the sputter-deposited diode is also significantly higher than those of the other two diodes. These higher reverse currents may be the result of process-induced defects that act as generation centres. Another interesting point is that the forward characteristic of the sputter-deposited diode shows a significant increase in series resistance compared to the other diodes. This is especially noticeable for the characteristics recorded at 100 K. This may be due to surface disorder introduced during the sputter deposition process. The control and EBD samples exhibited very similar series resistances, significantly lower than that of the sputter-deposited diode. These *I–V* measurements clearly demonstrate that both EBD and sputter deposition resulted in degraded *I–V* characteristics but that the sputter deposition yields the poorest diodes of the three metallization processes.

3.2. Defects introduced by EBD of different metals

First, we summarise what is already known for the defects introduced during EBD of Pt on Sb-doped Ge [6–8]. Note that no defects could be detected in the control SBDs fabricated by resistive deposition, indicating that the Ge is of high quality. The main defect introduced during EBD of Pt [7] was the E-centre (V–Sb complex) with its prominent associated electron and hole traps $E_{0.38}$, $H_{0.30}$ and $H_{0.09}$, respectively. In the nomenclature used here "E" means electron trap and the number following it is the energy level of this trap below the conduction band. Similarly, "H" means hole trap and the number following it is the energy level of this trap above the valence band. Note that we have not corrected these energy values to take into account the temperature dependence of the capture cross section, which has been shown to significantly change the activation energy of the E-centre [3]. Several other electron traps in lower concentrations were also detected. In the case of EBD the E-centre forms when energetic particles (originating in the region of the filament) impinge on the Ge and create vacancies at and close to the Ge surface [15]. These vacancies are mobile at room temperature and migrate into the Ge where they combine with Sb-dopant atoms to form the E-centre.

In Fig. 2, we compare the DLTS results recorded using SBDs of three different metals, namely Ti, Au and Ru, formed by EBD. The top three curves ((a)–(c)) are for electron traps but clearly hole injection could not be completely eliminated and therefore they still show the $H_{0.30}$ trap. The lower three curves ((d)–(f)) are for hole traps and were obtained after using intentional hole injection. As was the case for Pd and Pt, the most significant defect introduced is the E-centre with the traps $E_{0.38}$, $H_{0.30}$ and $H_{0.09}$ associated with it [3–8]. Curve (b) also shows the presence of a defect $E_{0.13}$ in a lower concentration, whereas curves (e) and (f) reveal the presence of additional hole traps, $H_{0.15}$ and $H_{0.18}$. The DLTS signatures of these defects were extracted from the Arrhenius plot in Fig. 3 and are summarised in Table 1.

From Fig. 2 it is further evident that the concentration of the E-centre increases from Ti to Au to Ru. In order to explain this trend, it should be borne in mind that the defects introduced by EBD are caused by ionised particles that are accelerated from the region near the filament [15] and impinge on the Ge surface. The concentration of these particles in the residual gas in the vacuum will increase with increasing residual gas pressure as well as with increasing emission current (proportional to the filament current). In the case of Ti evaporation, the starting vacuum

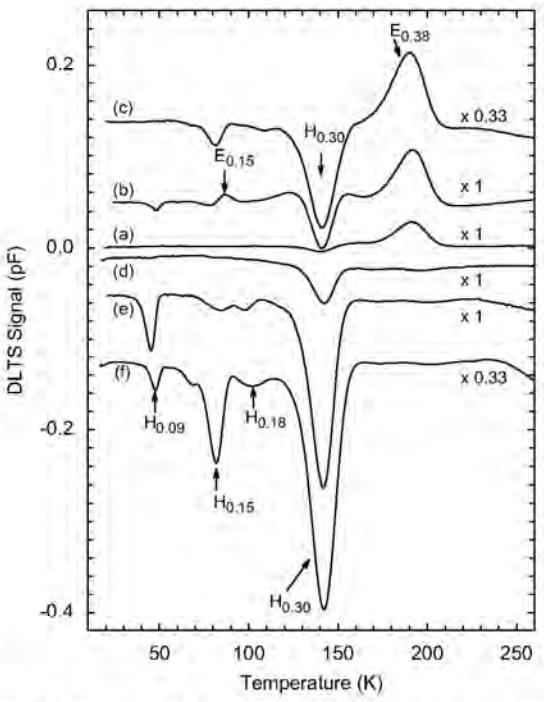

Fig. 2. DLTS spectra of Ti, Au and Ru Schottky contacts deposited by EBD to n-Ge: Curves (a), (b) and (c) are the electron-trap spectra for Ti, Au and Ru, respectively, while curves (d), (e) and (f) are the hole-trap spectra for Ti, Au and Ru, respectively. These spectra were recorded using a rate window of 80 s^{-1} at a quiescent reverse bias of −1 V. For the electron-trap spectra the pulse, V_p, was 0.15 V into forward bias. Hole-trap spectra were obtained by applying an injection pulse of $V_p = 3$ V into forward bias.

was more than an order of magnitude lower than for Au and Ru (Table 2). This means that, although the filament current was slightly higher than for Au deposition, a lower flux of particles reached the sample surface during evaporation, which in turn implies a lower level of damage, as observed in Figs. 1 and 2. When comparing the conditions for Au and Ru it can be seen from Table 2 that the vacuum during Au deposition was about the same as for Ru deposition. The filament current for Au deposition was only slightly lower than for Ru. However, if we consider the deposition rates then we notice that, due to its high melting point, the deposition rate of Ru is about one-twentieth of that of Au. This implies that it takes 20 times longer to deposit the same thickness of Ru as Au. This in turn means that the Ge surface is exposed to energetic particles for a much longer time during Ru deposition than during Au deposition, leading to the high concentration of defects observed for Ru metallization.

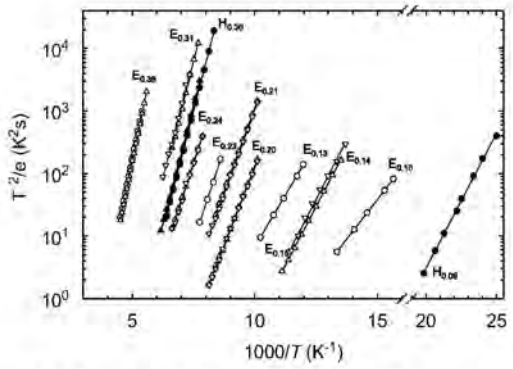

Fig. 3. Arrhenius plots for defects introduced by EBD (circles), MeV electron irradiation induced (triangles up) and sputter deposition (triangles down) in Ge. Filled symbols are for hole traps. All data were acquired using the bias and pulsing conditions defined in the caption of Fig. 2.

3.3. Comparison of defects introduced by EBD and sputter deposition

Curves (b) and (c) in Fig. 4 represent the DLTS spectra for Au Schottky diodes that were deposited by sputter deposition and EBD, respectively. Curve (d) was recorded after irradiating a resistively deposited diode with high-energy electrons at a dose of 2×10^{14} cm^{-2}. We have used Laplace DLTS to separate the signals of the $E_{0.20}$ and $E_{0.21}$

Table 1
Electronic properties of prominent defects introduced in n-type Ge during sputter and electron beam deposition of Schottky contacts, and by MeV electron irradiation

Sputter deposition				MeV electron irradiation				Similar defects/defect ID
Defect	E_T (eV) (±0.01)	σ_a (cm^2) (±10%)	T_{peak}[a] (K)	Defect	E_T (eV)	σ_a (cm^2)	T_{peak}[a] (K)	
$ES_{0.14}$	E_C−0.14	5.5×10^{-15}	78	$E_{0.15}$	E_C−0.15	2.8×10^{-14}	77	$E_{0.13}$[b], Sb and I related[c]
$ES_{0.20}$	E_C−0.20	3.7×10^{-14}	100	$E_{0.20}$	E_C−0.20	1.4×10^{-14}	100	$E_{0.19}$[c], Sb and I related[c]
$ES_{0.21}$	E_C−0.21	2.0×10^{-14}	109	$E_{0.21}$	E_C−0.21	3.6×10^{-14}	109	$E_{0.21}$[c], Sb related?[c]
$ES_{0.24}$	E_C−0.24	3.3×10^{-15}	131	$E_{0.24}$	E_C−0.24	2.5×10^{-15}	131	$E_{0.23}$[c], Sb and I related?[c]
$ES_{0.31}$	E_C−0.31	1.5×10^{-14}	151	$E_{0.31}$	E_C−0.31	5.0×10^{-14}	150	$E_{0.29}$[c]?, V_2[c]?
Electron beam deposition								
$E_{0.10}$	E_C−0.10	3.7×10^{-16}	65					
$E_{0.13}$	E_C−0.13	1.9×10^{-16}	85					
$E_{0.23}$	E_C−0.23	3.4×10^{-14}	116					
$E_{0.38}$	E_C−0.38	1.0×10^{-14}	191	$E_{0.38}$	E_C−0.38	1.1×10^{-14}	191	$E_{0.37}$[b], $E_{0.37}$[c], V–Sb (−/−)[b,c]
$H_{0.09}$	E_V+0.09	2.1×10^{-13}	47					
$H_{0.15}$	E_V+0.15	7.1×10^{-14}	82					
$H_{0.18}$	E_V+0.18	3.5×10^{-14}	97					
$H_{0.27}$	E_V+0.27	2.4×10^{-13}	133					
$H_{0.30}$	E_V+0.30	6.2×10^{-13}	141	$H_{0.30}$	E_V+0.30	3.66×10^{-13}	142	$H_{0.307}$[b], $H_{0.30}$[c], V–Sb (−/0)[b]

The error margins the value of E_T lie in the third digit after the decimal point whereas that for σ is less than 10% of its value.
[a] Peak temperature at a rate window of 80 s^{-1}.
[b] See Ref. [3].
[c] See Ref. [2].

Table 2
Electron beam deposition parameters and conditions for different metal Schottky contacts

Metal	Melting point (°C)	Thickness (nm)	Deposition rate (nm/s)	EB filament current (mA)	Starting vacuum (mbar)
Ti	1660	100	0.4	75	2×10^{-6}
Au	1064	200	0.5	60	5×10^{-5}
Ru	2250	50	0.02	70	6×10^{-5}

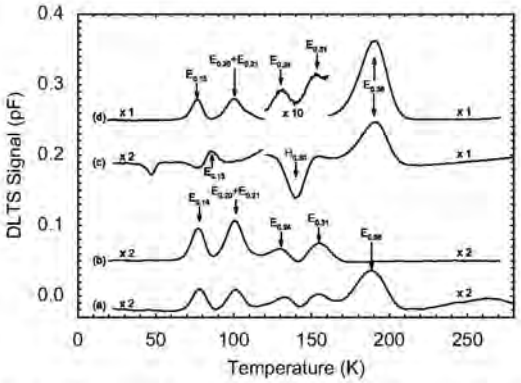

Fig. 4. DLTS spectra of Au Schottky contacts on n-Ge: Curves (a), (b) and (c) are the spectra for a sputter-deposited Au contact, a Au contact deposited by EBD and an electron-irradiated control contact, respectively. These spectra were recorded using a rate window of 80 s^{-1} at a quiescent reverse bias of −1 V. For the electron-trap spectra the pulse, V_p, was 0.15 V into forward bias.

of electron-irradiated samples. As described above, the E-centre is the only defect that is introduced by both EBD and high-energy electron irradiation. Curve (b) shows that sputter deposition introduced several electron traps: $E_{0.14}$, $E_{0.20}$, $E_{0.21}$, $E_{0.24}$ and $E_{0.31}$. However, the main electron trap introduced by EBD and electron irradiation, the E-centre, is not present in sputter-deposited diodes. Also, unlike in previous studies of high-energy electron-irradiated Ge and electron beam-deposited (EBD) Schottky diodes [6,7], we could not detect any hole traps in the sputter-deposited contacts studied here, even when applying a strong forward bias. However, after irradiating the sputter-deposited contacts with MeV electrons the $E_{0.38}$ trap associated with the E-centre could be clearly observed (curve (a) of Fig. 4). This means that sputter deposition by itself, in our sputter equipment and under our deposition conditions, does not introduce the E-centre. It is important to point out that the E-centre has been observed by Simoen et al. [10] after sputter deposition of Pt in a different sputter system.

The fact that the E-centre is not observed after sputter deposition in our system may imply that our sputter process does not introduce a sufficient number of single vacancies at and close to the surface that can diffuse into the Ge and combine with Sb ions to form V–Sb, as in the case of EBD. It should be realised that most of the damage that we observe after sputter deposition is caused by backscattered neutral Ar ions that, for the sputter conditions used here, have a maximum energy of approximately 700 eV of RF power [9]. From TRIM [14] modelling we have found that the range and straggle of these ions are 2.1 and 1.2 nm, respectively. In the first 3 nm each ion deposits on average 20 eV/nm in to the Ge lattice and produces, on average, 5 vacancies/nm. This implies that defects larger than the single vacancy, e.g. divacancy and vacancy or interstitial clusters, can be formed. Whereas vacancy clusters, such as the divacancy, are stable at room temperature [2], interstitial clusters, by nature, are not very stable. It is therefore conceivable that when they break up, interstitials are injected into the Ge during sputter deposition. Based on this we speculate that the defects we observe after sputter deposition are related to interstitial–impurity complexes (e.g. I–Sb) or vacancy or interstitial clusters, or complexes of these clusters with impurities. The signature of $E_{0.31}$ is close to that reported for the divacancy ($E_{0.29}$) [2], whereas the signatures of $E_{0.14}$, $E_{0.20}$ and $E_{0.21}$ are close to that of the $E_{0.13}$, $E_{0.19}$ and $E_{0.23}$ proposed to be related to Sb and the Ge interstitial [2].

3.4. Annealing of the metallization-induced defects

We have previously investigated the thermal stability of the defects introduced by EBD of Pt contacts by isochronal annealing in argon (Fig. 5) [7]. Only after annealing at 225 °C could the $E_{0.38}$ and $H_{0.30}$ levels no longer be detected. This is slightly higher than the 175–200 °C reported in Ref. [3] for removing the E-centre. However, it should be borne in mind that the annealing in Ref. [3] was under zero bias where most of the E-centres are filled with electrons. In our case, although we annealed at zero bias, the E-centres are very close to the surface and hence the levels of most of them are above the Fermi level. It has been reported that reverse bias annealing (E-centre level above the Fermi level) impedes the annealing of E-centres [2]. During annealing the concentration of $H_{0.26}$ increased up to 200–225 °C, rendering it the most prominent defect, and then it annealed out at 350 °C. At this temperature all the defects introduced during EBD were removed.

We have also previously investigated the thermal stability of the defects introduced by sputter deposition of Au contacts by isochronal annealing in argon [9]. After annealing at 150 °C the $E_{0.14}$, $E_{0.20}$ and $E_{0.24}$ levels could no longer be detected but the concentration of $E_{0.31}$ increased by about a factor of two. Annealing at 200 °C reduced the

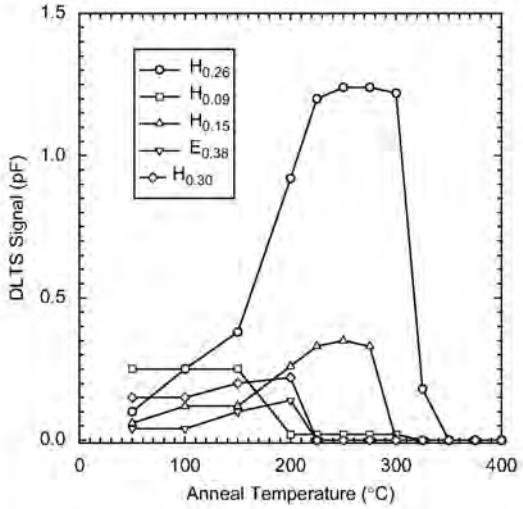

Fig. 5. Isochronal annealing (20 min periods) of the most prominent defects introduced by EBD in n-Ge [8].

concentrations of $E_{0.21}$ and $E_{0.31}$ by 10% and 30%, respectively, and annealing at 250 °C removed these defects completely, and no sputter deposition-induced defects could be detected any more. After annealing at 300 °C, no additional defects, i.e. no "second generation" defects could be observed, indicating that the sputter-deposition-induced defects did not reconstruct during annealing to form larger defects or different defect complexes.

4. Summary and conclusions

The *I–V* measurements demonstrated that both EBD and sputter deposition resulted in degraded *I–V* characteristics, but that sputter deposition yields the poorest diodes of the two metallization methods. The higher forward and reverse currents of Au Schottky contacts formed by sputter deposition and EBD as compared to resistively deposited Au contacts is most probably the result of process-induced defects that act as generation centres. Also, the sputter-deposited diode shows a significant increase in series resistance compared to the other diodes. This may be due to surface disorder introduced during the sputter deposition process.

Our DLTS results revealed that the main defect introduced during EBD has the same electronic properties as that of the V–Sb complex, or E-centre, introduced during high-energy electron irradiation of Ge. EBD also introduced several defects that are not introduced by electron irradiation, speculated to be higher-order vacancy clusters and complexes thereof with impurities. We show that the concentrations of the most prominent EBD-induced defect, the V–Sb centre, depended on the metal deposited by EBD via the melting point of the metal and the influence thereof on the vacuum during metallization: in general, low melting point metals resulted in less EBD damage. All the defects introduced by sputter deposition have also been observed after high-energy electron irradiation, but the V–Sb complex was not observed after sputter deposition. Annealing at 350 and 250 °C in Ar removed the defects introduced during EBD and sputter deposition, respectively, and annealing at higher temperatures did not introduce any new defects.

The role of these electron beam deposition and radiation-induced defects in optimising device performance for specific applications of Ge diodes will have to be carefully examined in order to ensure optimum device performance.

Acknowledgements

The authors gratefully acknowledge financial support of the South African National Research Foundation. The Laplace DLTS software and hardware used in the research was kindly provided by A.R. Peaker (Centre for Electronic Materials Devices and Nanostructures, University of Manchester) and L. Dobaczewski (Institute of Physics, Polish Academy of Sciences).

References

[1] Germanium silicon: physics and materials. In: Hull R, Bean JC, editors. Semiconductors and semimetals, vol. 56. San Diego: Academic Press; 1999.
[2] Fage-Pedersen J, Nylandsted Larsen A, Mesli A. Phys Rev B 2000;62(10):116.
[3] Markevich VP, Peaker AR, Litvinov VV, Emstev VV, Murin LI. J Appl Phys 2004;95:4078.
[4] Markevich VP, Hawkins ID, Peaker AR, Emstev KV, Emstev VV, Litvinov VV, et al. Phys Rev B 2004;70:235213–21.
[5] Markevich VP, Hawkins ID, Peaker AR, Litvinov VV, Dobaczewski L, Lindström JL. Appl Phys Lett 2002;81:1821.
[6] Auret FD, Meyer WE, Coelho SMM, Hayes M. Appl Phys Lettt 2006;88:242110.
[7] Auret FD, Meyer WE, Coelho SMM, Hayes M, Nel JM. Mater Sci Semiconductor Process 2006;9:576–9.
[8] Auret FD, Coelho SMM, Hayes M, Meyer WE, Nel JM. Phys Status Solidi (a) 2008;205(1):159–61.
[9] Auret FD, Coelho S, Meyer WE, Nyamhere C, Hayes M, Nel JM. J Electron Mater 2007;36(12):1604.
[10] Simoen E, Opsomer K, Claeys C, Maex K, Detavernier C, Van Meirhaegh RL, et al. Appl Phys Lett 2006;89:202114.
[11] Myburg G, Auret FD. J Appl Phys 1992;71:6172.
[12] Sawko DC, Bartko J. IEEE Nucl Sci 1983;30:1756.
[13] Dobaczewski L, Kaczor P, Hawkins ID, Peaker AR. J Appl Phys 1994;76:194.
[14] Dobaczewski L, Peaker AR, Bonde Nielsen K. J Appl Phys 2004;96:4689.
[15] Christensen C, Petersen JW, Nylandsted Larsen A. Appl Phys Lett 1992;61:1426.

9.4 Summary and conclusions

Similar to defects induced by electron irradiation, DLTS and LDLTS revealed that the dominant defect introduced by electron beam deposition is the V-Sb (*E*-center). This shows that during electron beam deposition vacancies are created below the semiconductor surface by particles which are ionized around the filament and then accelerated by the magnetic and electric fields torwards the sample. EBD also introduced some defects which were not observed in the electron irradiated samples. The concentration of V-Sb depended on the type of metal deposited via the melting point of the metal and the influence thereof on the vacuum during metallization. In general, low melting point metals resulted in less EBD damage. The *E*-center is removed after annealing at 225˚C, which is slight higher than the temperature at which this defect anneals in the electron irradiated samples. This difference in the annealing temperature has been attributed to the fact that the *E*-centers in the EBD deposited samples are closer to the surface and hence most of them are empty of electrons and this has been observed to impede the annealing of the *E*-center, whereas in the electron irradiated samples the *E*-center is deeper and hence most of the centers are filled with electrons during the annealing process. A hole trap *H*(0.27) exhibits some reverse annealing between from room temperature and reaches maximum concentration at 225˚C and anneals out at 350˚C. This trap has been attributed to the V-Sb_2 complex. All the defects were completely removed after annealing at 350˚C, which is a low thermal budget when compared to defects in silicon. This shows that defects in germanium have relatively lower binding energies than in silicon.

The annealing mechanism of the *E*-center has been investigated and it was found that it anneals by first order process with an activation energy 1.36 eV, and pre-exponential factor of $(1.2 \pm 0.3) \times 10^{12}\ s^{-1}$. Therefore, it is proposed that the *E*-center in Ge anneals by diffusion until its structure changes to another electrical active complex V-Sb_2.

References

[1] M. Lannoo, J. Bourngoin, *Point Defects in Semiconductors I, Theoretical Aspect* Springer series in solid state science 22, (1981).

[2] F.D. Auret, P.J. Janse van Rensburg, M. Hayes, J.M. Nel and W.E. Meyer, *Appl. Phys. Lett.* **89**, (2006) 152123.

[3] A.R. Peaker, V.P. Markevich, B. Hamilton, I.D. Hawkins, J. Slotte, K. Kuitunen, F. Tuomisto, A. Satta, E. Simoen and N.V. Abrosimov, *Thin Solid Films* **517** (2008) 152.

[4] F.D. Auret, S. Coehlo, W.E. Meyer, C. Nyamhere, M. Hayes and J.M. Nel, *J. of Electronic Materials* Vol. **36 No.2**, (2007) 1604.

[5] E. Simoen, K. Opsomer, C Claeys, K. Maex, C. Detavernier and R.L van Meirhaegh, *Appl. Phys. Lett.* 89 (2006) 202114.

[6] F.D. Auret, W.E. Meyer, S. Coehlo and M. Hayes, *Appl. Phys. Lett.* **88**, (2006) 242110.

[7] F.D. Auret, S.M.M. Coehlo, P.J. Janse van Rensberg, C. Nyamhere and W.E. Meyer, *Mater. Sci. in Semiconductor Processing* (2008) doi:10.1016/j.mssp.2008.09.001.

[8] V.P. Markevich, S. Bernardini, I.D. Hawkins, A.R. Peaker, V.I. Kolkovsky, A. Nylandsted Larsen and L. Dobaczewski, *Mater. Sci. in Semiconductor Processing* (2008) doi:10.1016/j.mssp.2008.09.007.

[9] J. Coutinho, V.J.B. Torres, S. Öberg, A. Carvalho, C. Janke, R. Jones *et al*, *Mater. Sci. Mater. Electron* **18** (2007) 769.

[10] V.P. Makervich, A.R. Peaker, V.V. Litvinov, V.V. Emstev and L.I. Murin, *J. Appl. Phys.* **95**, 4078 (2004).

[11] Y. Zohta and M.O. Watanabe, *J. Appl. Phys.* **53** No.**3** (1982) 1809.

[12] J.P. Biersack and L.G. Haggmark, *Nucl. Instrum. Methods* **174** (1980) 257.

[13] M. Mikelsen, E.V. Monakhov, G. Alfieri, B.S. Avset and B.G. Svensson, *Phys. Rev. B* 72 (2005) 195207.

[14] F.D. Auret and P.N.K. Deenapanray, *Crit. Rev in Solid State and Mater. Sci.* 29 (2004) 1.

[15] V.P. Markevich, *Mater. Sci. in Semicond. Process.* **9** (2006) 589.

[16] J. Coutinho, V.J.B. Torres, S. Öberg, A. Carvalho, C. Jonke, R. Jones and P.R. Briddon, *J. Mater. Sci.: Mater. Electron.* **18** (2007) 769.

List of publications

1. F.D. Auret, S.M.M. Coehlo, P.J. Janse van Rensberg, C. Nyamhere and W.E. Meyer Mater. Sci. in Semiconductor Processing (2008) doi:10.1016/j.mssp.2008.09.001.
2. F.D. Auret, S. Coehlo, W.E. Meyer, C. Nyamhere, M. Hayes and J.M. Nel, J. of Electronic Materials Vol. **36 No.2**, (2007) 1604.

Chapter 10

Defects introduced in antimony-doped germanium after sputtering by 3 keV Ar ions

10.1 Introduction

It is generally believed that heavy low energy ions may create shallow complex defects when compared to electrons and protons. Sputter deposition [1,2] and electron beam deposition [3,4] are associated with heavy ion damage in semiconductors. Sputtering is a widely used metal deposition and surface cleaning technique in microelectronics and generally is associated with defect creation by low energy heavy ions [3,4]. Aggressive scaling has resulted in the need for shallow junctions [5]. Defects introduced by low energy ions (e.g. during sputter etching) are usually located close to the semiconductor surface and therefore are important, particularly for shallow junction devices, as they will determine the reliability and performance of these devices. In this chapter defect levels introduced by low energy (3 keV) argon (Ar) ions are characterized.

10.2 Experimental Procedure

We have used bulk grown *n*-type Ge with (111) crystal orientation, doped with antimony, (Sb) to a density of 2.6 x 10^{15} cm^{-3} supplied by Umicore. Before metallization the samples of 0.5 cm x 0.3 cm in size were first degreased and then etched in a mixture of H_2O_2 (30%) : H_2O (1:5) for 1 minute. Immediately after cleaning they were placed in a vacuum chamber where AuSb (0.6% Sb), 130 nm thick, was deposited by resistive evaporation on their back surfaces as ohmic contacts. The samples were then annealed at 350 ˚C in argon (Ar) for 10 minutes to optimize the ohmic contacts. Prior to the Schottky contact fabrication, the samples were sputtered by 3 keV Ar ions of fluences, 1 x 10^{13} cm^{-2} and 1 x 10^{14} cm^{-2} using the

sputter gun in an Auger electron spectroscopy (AES) system. The sputtering process resulted in approximately 500 Å, thick layer being removed. Immediately after sputtering, Pd contacts, 0.60 mm in diameter and 100 nm thick were deposited by vacuum resistive evaporation. After the contacts were formed, the samples were characterized by current – voltage (*I-V*) and capacitance – voltage (*C-V*) techniques at room temperature. The defects introduced were characterised by DLTS and Laplace – DLTS [6,7]. The '*signatures*' of radiation induced defects (i.e. activation enthalpy for the electron and hole traps E_T, and apparent capture cross section, σ_a), were determined from Arrhenius plots of $\log(T^2/e)$ vs. $1000/T$, where '*e*' is either the hole or electron emission rate, and *T* is the measurement temperature.

DLTS measurements were performed regularly over a period of 4 months to monitor defect stability and evolution at room temperature. To obtain more information on the defects introduced by Ar ions sputtering, the samples were then annealed isochronally for 20 minutes in Ar gas from room temperature up to 300˚C. After each and every annealing cycle, *I-V, C-V,* DLTS and LDLTS measurements were performed.

10.3 Results

In this section the electronic and annealing properties of electron and hole traps created by Ar sputtering are discussed. The room temperature stability of the primary defects is also investigated.

10.3.1 Defects introduced in Ge after electron irradiation with different doses

The DLTS spectra (Fig. 10-1) shows the finger prints of the hole traps recorded after 3 keV sputtering with Ar ions of fluence 1 x 10^{14} cm^{-2}. Fig. 10-1 curve (a) shows the spectra recorded immediately after irradiation and curve (b) shows the spectra after one month of room temperature storage. The DLTS spectra measured immediately after the sputtering reveals an electron trap level *E*(0.38) and two hole traps *H*(0.09) and *H*(0.31) curve (a). In this nomenclature '*E*' is the electron trap and '0.38' is the position of the trap from the conduction band whereas '*H*' is the hole trap and '0.09' is the position of the trap relative to the valence band. After room temperature annealing for about a month a hole trap *H*(0.26) was observed. It should be noted that

the un-sputtered Ge did not contain any defects in the detectable range limit, which is consistent with data in refs. [8-9].

Table. 10.1. The summary of electron properties of primary defects introduced by 3 keV Ar sputter damage in n-Ge and secondary defects introduced after thermal annealing.

Defect	E_T(eV)	σ_a(cm^2)	T^a_{peak} (°C)	T^b_{in} (°C)	T^c_{out} (°C)	Defect Origin
E(0.38)	E_C – 0.38	5.1 x 10^{-14}	191	RT	225	V-Sb (--/-) [3,8-11]
H(0.09)	E_V + 0.09	7.8 x 10^{-13}	45	RT	225	V-Sb(+/0) [10]
H(0.14)	E_V + 0.14	1.3 x 10^{-14}	77	50	275	$H_{0.15}$ [3,4]
H(0.26)	E_V + 0.26	1.8 x 10^{-13}	140	RT	200	?
H(0.27)	E_V + 0.27	5.1 x 10^{-13}	140	200	---	V-Sb$_2$?
H(0.30)	E_V + 0.30	7.3 x 10^{-14}	142	200	---	?
H(0.31)	E_V + 0.31	3.3 x 10^{-14}	142	RT	225	V-Sb (0/-) [3,8-11]
H(0.40)	E_V + 0.40	4.8 x 10^{-11}	150	200	---	?

[a]Peak temperature with a rate window of 80 s^{-1}. [b]Temperature at which the defect was introduced. [c] Temperature at which the defect was removed.

The defect 'signatures' of the radiation induced defects and those that evolved at room temperature were extracted from the Arrhenius plots, shown in Fig. 10-5 (filled circles) and the electron properties of these traps are summarised in Table 10.1. When compared with defects introduced in similar samples by 1 MeV electron irradiation [8-11,12], sputter deposition [1,2] and electron beam deposition [3,4], *H*(0.09), *H*(0.31) and *E*(0.38) have also been observed in the electron irradiated samples and electron beam deposition [3,4,13]. *H*(0.09), *H*(0.31) and *E*(0.38) have been assigned to the (+/0), (0/-), (--/-) charge states of the *E*-center respectively [3,8-11]. The identity of *H*(0.26) is not clear at the moment.

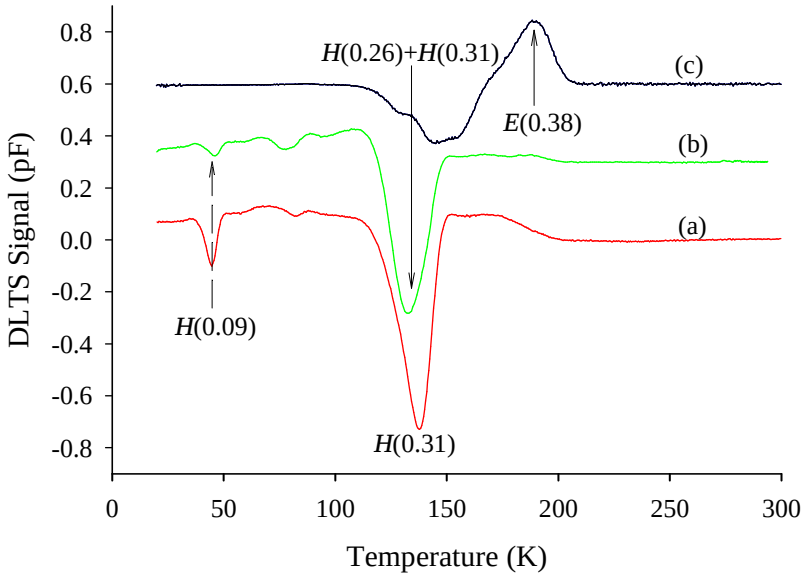

Fig. 10-1. The DLTS hole spectra after 3 keV Ar ions sputtering with a fluence of 1 x 10^{14} cm^{-2}, on n-Ge, (a) immediately after sputtering and (b) after room temperature annealing for a month. (c) DLTS electron traps spectra after sputtering. These spectra were recorded at a rate window (RW) of 80 s^{-1}, a quiescent reverse bias of V_r = -2 V with a filling pulse V_P = +3 V (hole traps) and V_P = 0 V (electron traps) superimposed on the reverse bias and with a pulse width of 1 ms.

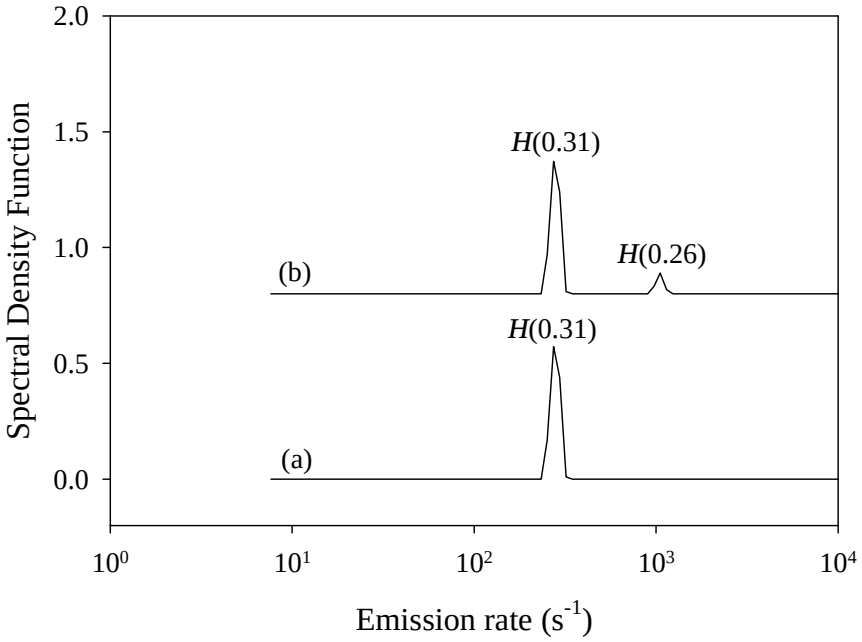

Fig. 10-2. LDLTS spectra recorded (a) immediately after sputtering showing H(0.31) peak and (b) after room storage for a month showing peaks for both H(0.31) and H(0.26). Both spectra were recorded at a temperature of 143 K.

The LDLTS depicts a single sharp peak immediately after the sputtering process attributed to the *H*(0.31) as shown in Fig. 10-2 (a) and after a month at room temperature another peak for trap *H*(0.26) emerges on LDLTS spectra as clearly illustrated in Fig. 10-2 (b), resulting in an apparently DLTS single peak slightly shifted to lower temperature.

10.3.2 Annealing behavior of the electron and hole traps

The annealing behavior of defects induced by 3 keV Ar ions sputtering on Ge is depicted in Fig. 10.3 and the electron properties extracted from the annealing graphs and Arrhenius plots depicted in Fig. 10-6 (open circles, after annealing at 225ºC) and (open triangles, after annealing at 275ºC) are summarized in Table. 10.1. The hole traps *H*(0.09), *H*(0.26), *H*(0.31) and *E*(0.38) were stable up to 175ºC as shown in Figs. 10-3 and 10.5 but *H*(0.09) and *H*(0.31) were both removed after annealing at 225ºC.

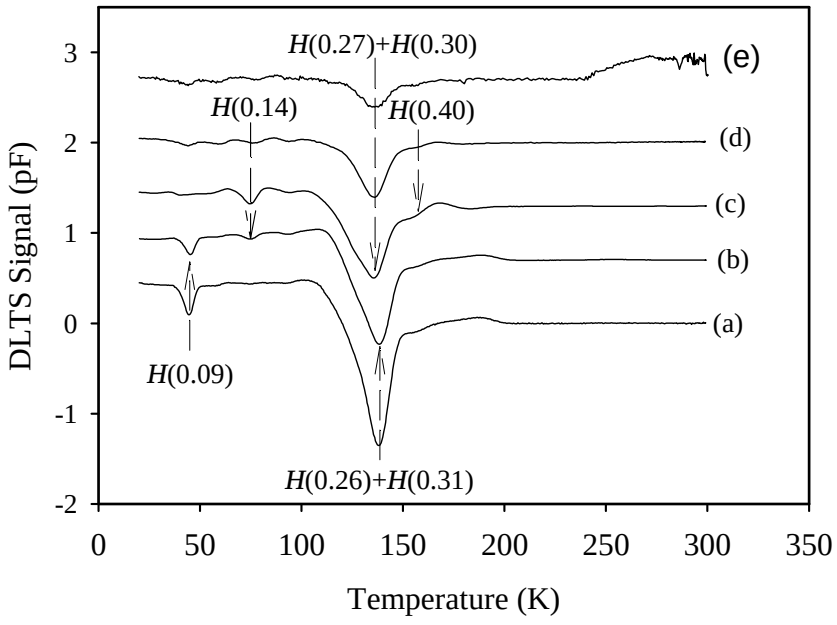

Fig. 10-3. The DLTS spectra showing defects created in n-Ge doped with Sb after sputtering with 3 keV Ar ions of fluence 1 x $10^{14}cm^{-2}$ (a) after room temperature annealing for a month, and after annealing at (b) 175ºC, (c) 225ºC, (d) 250ºC, (e) 285ºC. The measurements were recorded at quiescent reverse bias, V_r = -2 V, pulse voltage, V_p = +3 V, pulse width of 1 ms and rate window (RW) of 80 s^{-1}.

The hole trap *H*(0.14) was introduced after annealing at 50ºC and was removed at 275ºC whereas traps *H*(0.27), *H*(0.30) and *H*(0.40) are observed after annealing at 225ºC and were still present at the highest annealing temperature of 285ºC beyond which the diodes were too degraded for DLTS measurements. The Arrhenius plots in Fig. 10-6 clearly shows that the pair *H*(0.27) and *H*(0.26) and the pair *H*(0.30) and *H*(0.31) are indeed different sets of defects.

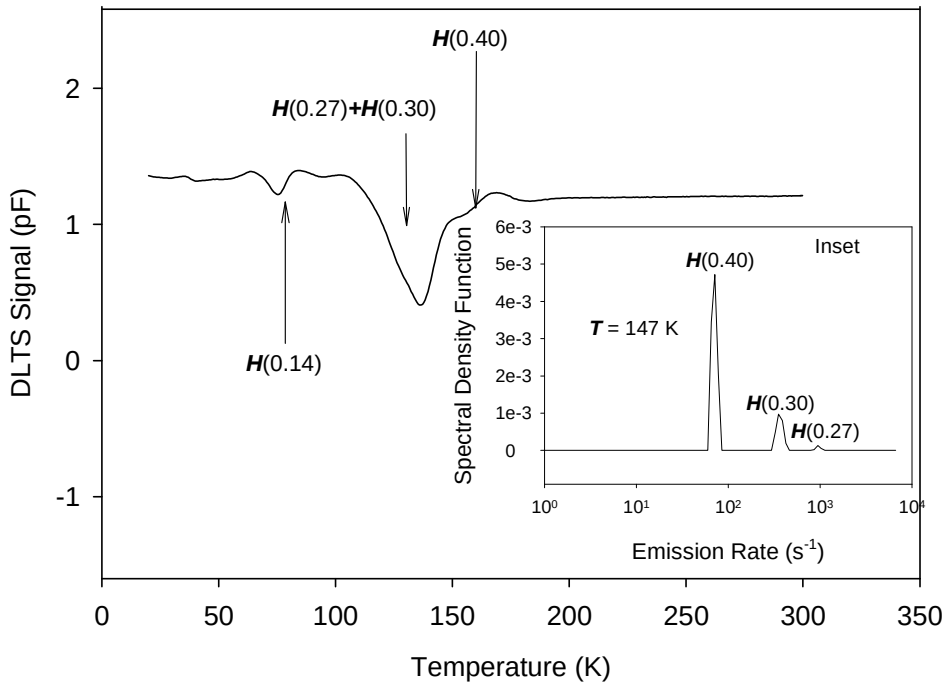

Fig. 10-4. DLTS spectra recorded after annealing at 225ºC. Inset: LDLTS showing the peaks H(0.27), H(0.30) and H(0.40) measured at 147 K.

H(0.27) has been observed after electron beam deposition and has been attributed to V-Sb_2 complex since it is observed after the annealing of the *E*-center [14]. *H*(0.30) and *H*(0.40) are new secondary defects and their identities are still unclear at the moment, but could be attributed to higher order V_n-Sb_n complexes. LDLTS was successfully used to separate the trap levels *H*(0.27), *H*(0.30) and *H*(0.40) as shown in Fig. 10-4 (inset). Annealing studies of similar samples irradiated with electrons [8-11] and after electron beam deposition [3-4] did not reveal the same secondary defects suggesting that introduction of these complex defects are dependent on the mass and energy of the irradiating particles.

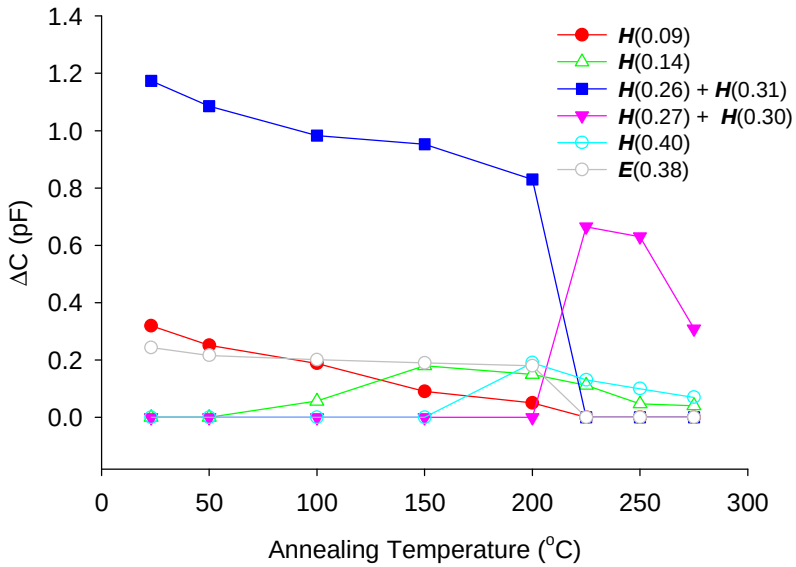

Fig. 10-5. Annealing behavior of defects introduced in germanium by 3 keV Ar sputtering.

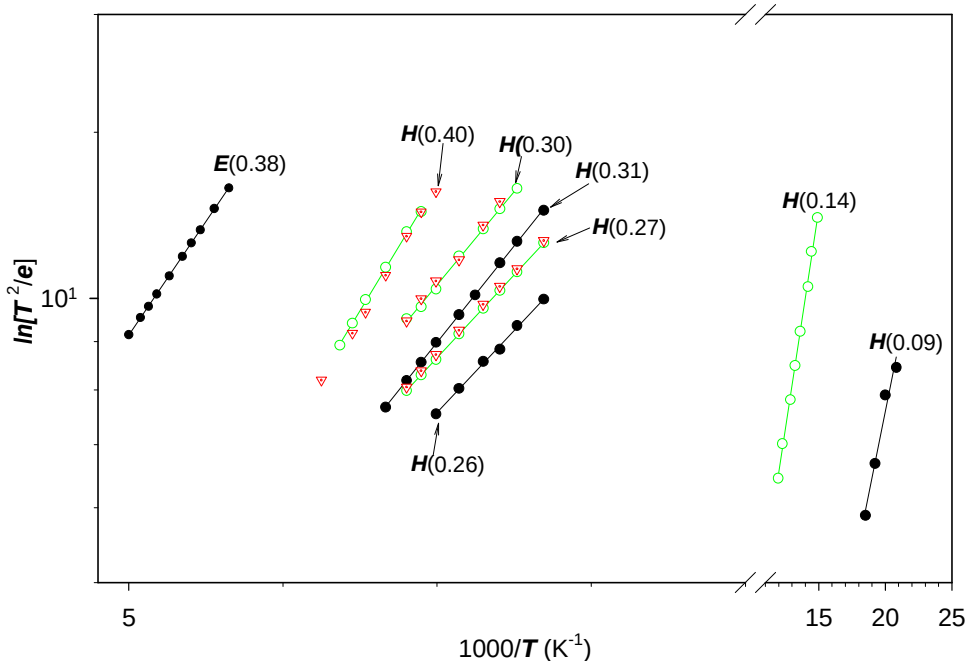

Fig. 10-6. The Arrhenius plots of the defects created in n-Ge after 3 keV sputtering with Ar ions with a dose of 1 x 10^{14} cm^{-2} for as-sputtered and recorded after a month (solid black circles), after annealing at 225ºC (open green circles) and after annealing at 275ºC (open red triangles).

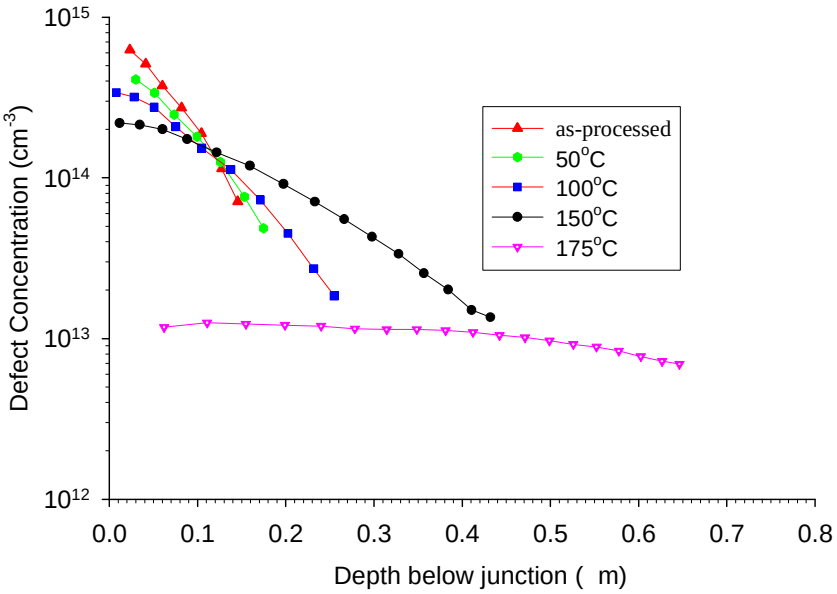

Fig. 10-7. Defect depth profile for the E(0.38) (E-center) recorded at various isothermal annealing temperatures from room temperature upto 175˚C.

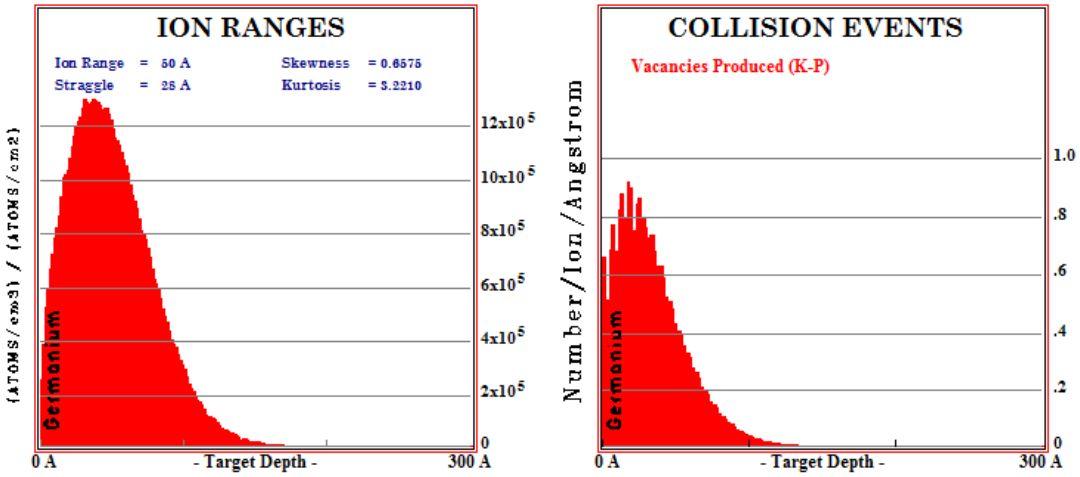

(a) (b)

Fig. 10-8. (a) TRIM simulation for the projected ion range and (b) damage events of 3 keV argon ions in germanium.

The depth profile of the *E*-center for as-irradiated samples showed a decrease in concentration from the semiconductor surface, which is a characteristic of damage by heavy ions as shown in Fig. 10-7. Upon annealing, the profile broadened and defect concentration significantly decreased at a temperature of 175˚C, which indicates the diffusion of the traps deeper into the material before its structure changes at 225˚C.

The projected ion range of the Ar ions in germanium is 5 *n*m below the junction and each ion produces, on average, 9 vacancies/*n*m as shown in the TRIM (version 2006.02) [15] simulation depicted in Fig. 10-8. The vacancy-interstitial pairs are expected to be formed within this projected ion range region before they diffuse and captured by other impurities to form stable complexes. Thus, higher order vacancy- or interstitial-related complex defects are likely to be formed.

10.4 Summary and conclusions

The 3 keV Ar ion sputtering introduces three primary traps, *H*(0.09), *H*(0.31), and *E*(0.38) which are similar to those introduced by electron irradiation and electron beam deposition which are the single donor, single acceptor and double acceptor charge state of the *E*-center respectively. The trap *E*(0.38) is the only electron trap observable after the sputtering process and the observation of other electron traps could have been impeded by injection of minority carrier even without applying minority carrier injection pulse. The creation of the V-Sb center shows that Ar sputtering introduces vacancy-interstitial pairs at and below the semiconductor surface. After room temperature storage for a month, a trap *H*(0.26) was observed and the origin of this trap is still not clear at the moment. The annealing studies have further revealed hole traps *H*(0.27), *H*(0.30) and *H*(0.40) which were all formed after the annealing of the *E*-center at 200˚C. *H*(0.27) has been observed after electron irradiation and annealing and also after electron beam deposition. It has been suggested that this center is a product of the *E*-center annealing and has been assigned to V-Sb_2. *H*(0.30) and *H*(0.40) have not been observed before and their identities are still unknown at the moment, but be higher order, vacancy- or interstitial-related complexes. More work in terms of defect models are required to identify these secondary defects.

References

[1] F.D. Auret, S. Coehlo, W.E. Meyer, C. Nyamhere, M. Hayes and J.M. Nel, *J. of Electronic Materials*, Vol. **36 No.2**, (2007) 1604.

[2] E. Simoen, K. Opsomer, C. Claeys, K. Maex, C. Detavernier and R.L. van Meirhaegh, *Appl. Phys. Lett.* 89 (2006) 202114.

[3] F.D. Auret, W.E. Meyer, S. Coehlo and M. Hayes, *Appl. Phys. Lett*. **88**, (2006) 242110.

[4] F.D. Auret, W.E. Meyer, S. Coehlo and M. Hayes, J.M. Nel, *Mater. Sci. Semiconductor Process*, **9**, (2006) 576.

[5] L.D. Yau, *Solid State Electronics*, vol. **17**, (1974) 1059.

[6] L. Dobaczewski, P. Kaczor, I.D. Hawkins, A.R. Peaker, *J. Appl. Phys*. **76** (1994) 194.

[7] L. Dobaczewski, A.R. Peaker and K.B. Nielsen, *J. Appl. Phys*. **96** (2004) 4689.

[8] J. Fage-Pedersen, A. Nylandsted Larsen and A. Mesli, *Phys. Rev. B*. **62** (2000) 10116.

[9] Cloud Nyamhere, F.D. Auret, A.G.M. Das and A. Chawanda, *Physica B* **401-402** (2007) 499.

[10] C.E. Lindberg, J. Lundsgaard Hansem, P. Bomholt, A. Mesli, K. Bonde-Nielsen and A. Nylandsted Larsen, *Appl. Phys. Lett*. **87** (2005) 172103.

[11] Cloud Nyamhere, M. Das, F.D. Auret and A. Chawanda, *Phys. Stat. Sol*. (C) **5 No. 2** (2008) 623.

[12] F.D. Auret, S. Coelho, W.E. Meyer, C. Nyamhere, M. Hayes and J.M. Nel, *J. of Electronic Mater*. **36 No.2** (2007) 1604.

[13] F.D. Auret, S.M.M. Coehlo, P.J. Janse van Rensberg, C. Nyamhere and W.E. Meyer, *Mater. Sci. in Semiconductor Processing* (2008), doi:10.1016/j.mssp.2008.09.001.

[14] V.P. Markevich, S. Bernardini, I.D. Hawkins, A.R. Peaker, V.I. Kolkovsky, A. Nylandsted Larsen and L. Dobaczewski, *Mater. Sci. in Semiconductor Processing* (2008) doi:10.1016/j.mssp.2008.09.007.

[15] J.P. Biersack and L.G. Haggmark, *Nucl. Instrum. Methods* **174** (1980) 257.

List of Publications

C. Nyamhere, A.G.M. Das, F.D. Auret, A. Chawanda, W. Mtangi, Q. Odendaal and A. Carr, *Physica B.* doi:10.1016/j.physb.2009.09.037.

Chapter 11

Conclusions

Detailed conclusions for specific experimental results have been presented at the end of each and every chapter. In this chapter a more general summary is presented.

Deep level transient spectroscopy (DLTS) and Laplace-DLTS (LDLTS) have been used successfully to characterize defects introduced in silicon and germanium by MeV electron irradiation and during metallization by electron beam deposition. LDLTS has been particularly useful in the deconvolution of deep levels with similar emission rates ($e_1/ e_2 > 2$), which otherwise could not be resolved by DLTS. New defect levels have been observed by using high resolution LDLTS which were not observed before by DLTS, enhancing the understanding of radiation and process-induced defects in silicon and germanium.

It has been shown that defects are introduced at and below the semiconductor surface during metallization. The source of the damage has been attributed to the residual vacuum gases, such as carbon, nitrogen, and oxygen, which are ionized near the filament region and then accelerated by magnetic and electric fields towards the sample, thereby causing lattice damage in the substrate region close to the surface. The vacancies and interstitial created are mobile at room temperature, hence they diffuse until they are captured by other impurities to form stable complexes.

Defects introduced in n- and p-type silicon by electron irradiation and during electron beam deposition have been characterized and compared. Although there are several similar defects, electron beam deposition introduces other defects which were not observed after electron irradiation. The reason for this lies in the nature of primary

damage introduced by irradiating particles. Heavier ions create vacancy-rich regions along the ion path with interstitial-rich regions near the end of projectile. Therefore, the opportunity for multi-vacancy and multi-interstitials reactions are much greater leading in complex defect formation. On the other hand, light particles such as, electrons, create uniform distribution of Frenkel pairs along their path, resulting in simple vacancy and interstial-related defects uniformly distributed with the material.

Similarly, defects introduced in n-type germanium by both MeV electron irradiation and during electron beam deposition have been characterized and compared. The most dominant defect observed after the two processes is the V-Sb (*E*-center). This shows that the energic particles found in the electron beam deposition and electron irradiation introduces vacancy-interstitial pairs beneath the semiconductor surface, which will then diffuse and form stable vacancy-related and other defects. Detailed annealing studies on the *E*-center showed an activation energy of 1.36 eV for the annealing process and a pre-exponential of $(1.2 \pm 0.3) \times 10^{12}$ s^{-1} and this point to a diffusion-driven annealing mechanism of this center. It is worth noting that while the divacancy in silicon is well known and has been characterized, in germanium this trap level has not been identified by experimental techniques.

In contrast to silicon, all electron irradiation and electron beam deposition damage were removed easily from germanium with very low thermal budget of between 350˚C - 400˚C compared to a thermal budget between 500˚C - 600˚C for defects in silicon. The annealing thermal budget indicates relative lower binding energies of defects in germanium than in silicon.

Although defects introduced in silicon and germanium have been characterized in this work, in terms of defect signatures and annealing properties, some of these defects are still to be identified. Thus, more work, in terms of defect models is necessary to properly identify these defects.

Future work

Further work can be done to characterize defects introduced during low energy (keV range) sputtering using other noble gas ions such as, Ne, Kr, Xe. The energy and fluences of the noble gas ions can also be varied.

More research work is required to identify the residual vacuum particles which are responsible for the lattice damage on and beneath the samples surfaces during electron beam deposition. Various modification to the EBD system maybe done, e.g. putting a shield around the sample to limit or eliminate damage from residual gas particles.